

# **Frequency metrology tools for high-precision spectroscopy of molecular hydrogen ions**

Inaugural-Dissertation

zur Erlangung des Doktorgrades  
der Mathematisch-Naturwissenschaftlichen Fakultät  
der Heinrich-Heine-Universität Düsseldorf

vorgelegt von

**Michael G. Hansen**  
aus Düsseldorf

Düsseldorf, Juli 2021

Institut für Experimentalphysik  
der Heinrich-Heine-Universität Düsseldorf

Gedruckt mit der Genehmigung der  
Mathematisch-Naturwissenschaftlichen Fakultät der  
Heinrich-Heine-Universität Düsseldorf

Referent: Prof. Stephan Schiller, Ph.D.

Koreferent: Prof. Dr. Axel Görlitz

Tag der mündlichen Prüfung: 31.5.2022

## Eidesstattliche Versicherung

Ich versichere an Eides Statt, dass die Dissertation von mir selbständig und ohne unzulässige fremde Hilfe unter Beachtung der “Grundsätze zur Sicherung guter wissenschaftlicher Praxis an der Heinrich-Heine-Universität Düsseldorf” erstellt worden ist.

Düsseldorf,

---

Michael G. Hansen

# Contents

<b>Eidesstattliche Versicherung</b>	<b>3</b>
<b>Contents</b>	<b>4</b>
<b>Abstract</b>	<b>6</b>
<b>1 Introduction</b>	<b>8</b>
1.1 Motivation . . . . .	9
1.1.1 Improve QED calculations and ab-initio calculations . . . . .	9
1.1.2 Determination of fundamental constants and their time variation . . . . .	10
1.1.3 Searching for physics beyond the Standard Model . . . . .	12
1.1.3.1 Improve limits on the existence of a fifth force . . . . .	13
1.1.3.2 Limits on the size of other dimensions . . . . .	13
1.2 Why cold ions? . . . . .	14
<b>2 The molecular ion <math>\text{HD}^+</math></b>	<b>14</b>
<b>3 Spectroscopic sources</b>	<b>17</b>
3.1 THz source at 1.3 THz . . . . .	17
3.1.1 Characterization of synthesizer linewidths . . . . .	18
3.2 Quantum cascade laser at 5.4 $\mu\text{m}$ . . . . .	22
3.2.1 Sum-frequency generation using OP:GaAs . . . . .	22
3.2.2 Lock-guard for stabilization of QCL to ULE . . . . .	25
3.2.3 Polarization and power stabilization of an EDFA . . . . .	26
3.2.4 Demonstration of spectroscopy . . . . .	29
3.3 Difference-frequency generation based sources for 5.1 $\mu\text{m}$ . . . . .	29
3.3.1 First-generation 5.1 $\mu\text{m}$ source . . . . .	30
3.3.2 New spectroscopy source for 5.1 $\mu\text{m}$ . . . . .	31
3.4 Frequency comb . . . . .	35
3.4.1 Application: Characterization of new cavity materials . . . . .	35
3.4.2 Application: Spectroscopy of Europium . . . . .	36
<b>4 Supporting laser systems</b>	<b>37</b>
4.1 UV1: Automated frequency tuning . . . . .	37
4.2 UV3: Stabilization of a cooling laser to a ULE cavity . . . . .	39
4.3 DFB: Improved frequency agility for optical state preparation lasers . . . . .	43
<b>5 Results</b>	<b>46</b>
5.1 Rotational spectroscopy . . . . .	46
5.2 Ro-vibrational spectroscopy . . . . .	47
5.2.1 Doppler-limited ro-vibrational spectroscopy . . . . .	47
5.2.2 Ro-vibrational spectroscopy in the Lamb-Dicke regime . . . . .	48
<b>6 Cumulative part of the dissertation</b>	<b>50</b>
6.1 Article: UV source for laser-cooling based on quintupling . . . . .	51
6.1.1 Contributions of the various authors . . . . .	51
6.1.2 Copyright . . . . .	51



6.2	Article: Rotational THz spectroscopy . . . . .	52
6.2.1	Contributions of the various authors . . . . .	52
6.2.2	Copyright . . . . .	52
6.2.3	Original article . . . . .	53
6.3	Article: Ro-vibrational spectroscopy of HD <sup>+</sup> . . . . .	60
6.3.1	Contributions of the various authors . . . . .	60
6.3.2	Copyright . . . . .	60
6.3.3	Original article . . . . .	61
6.4	Article: Frequency stabilization of a mid-IR QCL to a frequency comb . . . . .	66
6.4.1	Contributions of the various authors . . . . .	66
6.4.2	Copyright . . . . .	66
6.5	Article: Linewidth-narrowing of a QCL . . . . .	67
6.5.1	Contributions of the various authors . . . . .	67
6.5.2	Copyright . . . . .	67
6.6	Article: Rotational spectroscopy in the Lamb-Dicke regime . . . . .	68
6.6.1	Contributions of the various authors . . . . .	68
6.6.2	Copyright . . . . .	68
6.7	Article: Characterization of a NEXCERA-resonator . . . . .	69
6.7.1	Contributions of the various authors . . . . .	69
6.7.2	Copyright . . . . .	69
6.7.3	Original article . . . . .	70
6.8	Article: Europium hole-burning spectroscopy . . . . .	76
6.8.1	Contributions of the various authors . . . . .	76
6.8.2	Copyright . . . . .	76
6.8.3	Original article . . . . .	77
6.9	Article: High-resolution ro-vibrational spectroscopy of HD <sup>+</sup> . . . . .	85
6.9.1	Contributions of the various authors . . . . .	85
6.9.2	Copyright . . . . .	85
<b>7</b>	<b>Outlook</b>	<b>86</b>
<b>A</b>	<b>Appendix</b>	<b>87</b>
A.1	Tabular values of figures . . . . .	87
A.2	Beam analyzer for beam overlap for SFG . . . . .	89
	<b>Acknowledgements</b>	<b>93</b>
	<b>Publication list</b>	<b>94</b>
	<b>List of ORCIDs</b>	<b>95</b>
	<b>Bibliography</b>	<b>96</b>

## Abstract

The goal of this thesis is to use frequency metrology of molecular hydrogen ions to verify ab-initio calculations of molecular transition frequencies, determine fundamental constants, and to look for physics beyond the Standard Model, in particular fifth forces and extra dimensions. To this end, a variety of high-performance laser systems and other tools for frequency metrology are required. In this thesis, some of these systems were newly developed, existing ones improved and also basic research for next-generation systems was performed.

Molecular hydrogen ions, in particular the molecule  $\text{HD}^+$ , were chosen as spectroscopic workhorse. They are the simplest molecules, because they have only three components. On the theoretical side, their transition frequencies can be determined very accurately. Still, the calculations are rather complex and have been steadily advanced over several orders of magnitude in the last 20 years. By comparison between theory and experiment, a physical constant used for the calculation of the transition frequency can be treated as a free parameter and be determined from experimentally obtained transition frequencies. Any remaining frequency discrepancy between theory and experiment can be treated as an upper limit of the strength of hypothetical new physical effects. In this case, theory beyond the Standard Model is of interest. In order to fill the gap between the Standard Model and the theory of gravity, various extensions to the Standard Model have been proposed. One of them are fifth forces between particles, which either have very weak interaction strengths or can only be observed on length-scales which have not yet been explored. Another extension is based on the concept of extra dimensions, which allow the force of gravity to act differently from our 3+1 dimensional world at certain length scales.

Spectroscopy on the  $\text{HD}^+$  ion was performed while the molecule was trapped in an ion trap and cooled to ultra-cold temperatures. This provides the advantage of long interaction times with the spectroscopy lasers as well as reduced Doppler broadening, due to lower temperatures. For spectroscopic experiments to work well, the apparatus had to remain stable and provide repeatable operations over long timescales. To this end, several advances on the setup were made in this thesis, especially with regard to manual operator intervention and simpler frequency stabilization for the supporting laser systems. Both pure rotational as well as ro-vibrational transitions were spectroscopied using the ion trap setup.

Rotational spectroscopy was performed using a microwave source based on frequency multipliers. The feasibility of performing spectroscopy on a rotational transition was demonstrated using this source, albeit at low resolution. Using a new Doppler-free spectroscopy technique, a transition linewidth of 1.3 kHz was obtained, an improvement by almost 3 orders of magnitude over previous results. From these results, the constant  $m_p$  was determined. The result was consistent with the officially recommended value [1], but provides an independent verification, since it was determined using another method.

Ro-vibrational spectroscopy was performed using a difference frequency generation system, whose frequency was measured using an optical frequency comb. The lowest observed transition linewidth of 3 MHz was still Doppler-limited, but allowed a comparison between theory and experiment at the  $10^{-9}$  level and was the first to probe QED effects at the order  $\alpha^5$ . The results of these measurements were used by other researchers to set new limits on possible fifth forces.

In order to further increase the measurement resolution, two new laser systems were set up. One was a quantum-cascade laser system in the mid-IR, referenced to a near-IR frequency comb in order to be able to precisely control its absolute frequency. The system reached a record linewidth.

An improved version of the laser system based on difference frequency generation was also set up, this time performing the non-linear frequency conversion in waveguide non-linear optical crystals. It was also referenced to the frequency comb and therefore provided accurate absolute

frequency stability and low linewidth. Using this laser system and the new spectroscopy method demonstrated for the rotational transition, sub-Doppler transition linewidths of 0.2 kHz ( $3 \times 10^{-12}$  fractionally) were obtained. From these, an agreement between theory and experiment at the  $2.9 \times 10^{-11}$  level was reached. Also, the ratios of the constants  $m_p/m_e$  and the ratio of the reduced nuclear mass  $\mu$  to the electron mass  $m_e$  were determined in an alternative way to the measurements used for previous determinations of their officially recommended values[2]. The obtained results were consistent.

Frequency metrology using lasers is always fundamentally limited by the short- and long-term performance of the reference lasers used for the spectroscopy and the optical frequency comb. To this end, research on new reference systems was performed: The long-term stability of a new material for spacers for optical resonators (NEXCERA) was studied. As an alternative to the optical resonator approach, properties of spectral holes in Europium-doped crystals at cryogenic temperatures were investigated.

The obtained results demonstrate that spectroscopy of trapped molecular hydrogen ions, combined with the right tools, are now on-par with other methods for the determination of physical constants, as well as for tests of the validity of the Standard Model. Results improved by several orders of magnitude are likely to be obtained in the near future.

# 1 Introduction

As far back as we can trace human history, there has always been a desire in humans to understand and explain the phenomena observed in nature. Initially, these desires were filled by the creation of stories, which linked physical and biological phenomena to actions of Gods and other spiritual beings. With the advent of scientific rigor, they were replaced with theories and models. Whenever new phenomena were observed or known phenomena were investigated more thoroughly, those models who did not stand the test of time had to be discarded or extended. A good example of this is the way in which the description of the composition of matter has changed over time. Initially explained as a composition of the four elements fire, air, water, and earth, different atoms were discovered and took their place. The atoms, at first thought to be the smallest, solid, and unbreakable components of matter, were soon discovered to have their own inner structure, described by Bohr's model of the atom. With ever-increasing accuracy of measurements, Bohr's model of the atom had to be extended ever finer until today's description via Quantum-Electro-Dynamics. Later, even some of the components of the atom could be further dismantled, paving the way to Quantum Chromodynamics.

When new models were brought up, they had to be consistent with the currently observed phenomena. In order to verify them, their predictions in previously unexplored regions of physics have to be tested. This allows to put limits on the strength of their possible effects.

Today, our physical world is described by the Standard Model of particle physics, and the theory of general relativity. Unfortunately, these two models do not converge when considered together on small particles. Separately, on large scales, we observe deviations from the law of gravity governed by general relativity. These discrepancies inspire a search for new physics, which will hopefully lead to new theories which can fill the gaps. New physics can either be found by more stringent tests on the validity of existing models or by "accidental" discovery of new phenomena.

The discovery of new phenomena is often the result of an accident and can therefore not be planned. Imagine writing a research grant, where you explain that you will perform "sloppy" work in the lab in the hope that you will find new antibiotics.

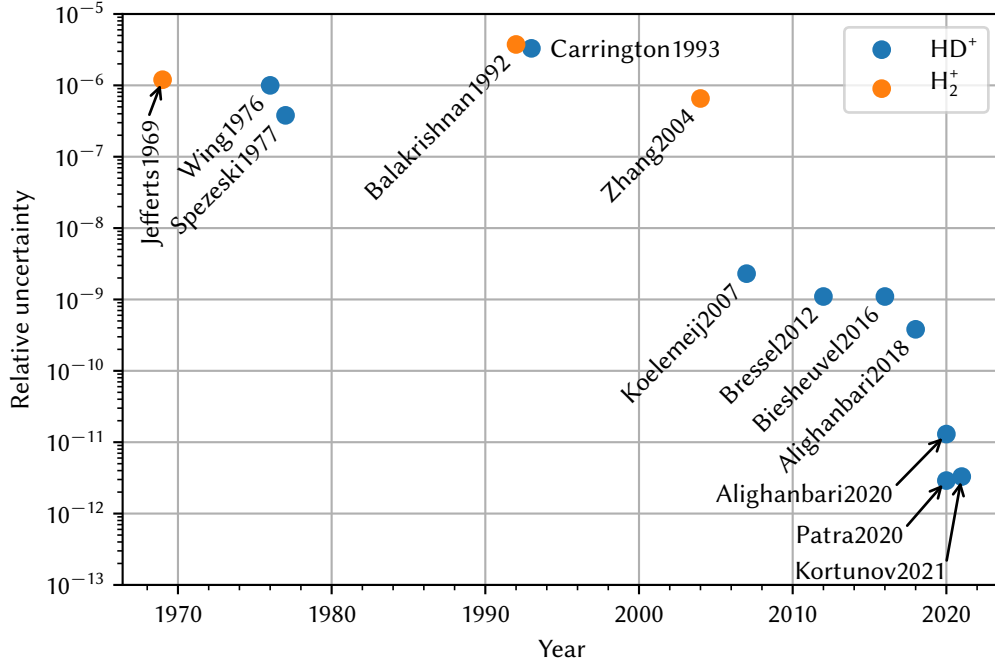
Increasing the precision of existing measurements can also not promise a break-through, but at least the required effort can be estimated and the desired outcome be evaluated in terms of its effect on the increased coverage of the validity of a certain theory.

Due to a lack of new physics discovered via previously unobserved phenomena, new models were thought up to either unify the two theories or explain other discrepancies between the predictions of those theories and real observations.

The search for new physics is currently being performed at all scales of length and energy. This thesis focuses on the search at short length scales and low energies.

On the unification front, several extensions to the Standard Model have been proposed. The most well-known extensions are string-theory and quantum-loop-gravity. String-theory uses the concept of extra dimensions to establish a mathematical description in which the Standard Model and the general theory of relativity can be unified.

The implications of string-theory depend on how the parameters of the model are set up. The extra dimensions suggested by string-theory contradict our current observations of three spatial dimensions and one time dimension. One parameter that can be adjusted in such a model is the size of the extra dimensions, affecting both their compactification and their curvature. It is feasible that these extra dimensions are quite small and therefore their effects have not yet been detected. To this end, increasing the measurement resolution can set boundaries on the scale at which the effects of extra dimensions can be observed. Another possible effect of string-theory is a change of the values of fundamental constants over time. Here, precision measurements must be repeatedly performed



**Figure 1.1:** Relative uncertainties in the measurement of molecular hydrogen ion transition frequencies. Only values with uncertainties smaller than  $10^{-5}$  are shown. Values and references are listed in table A.1.

in order to set limits on this time variation. In order to increase the confidence in the determination of these constants, they should be determined by several different means.

## 1.1 Motivation

Spectroscopy of molecular hydrogen atoms can be traced back to as far as the end of the 1960s. Figure 1.1 shows the relative uncertainties of spectroscopic results found in the literature. In this section, the motivation behind the desire for ever better spectroscopic resolution is explained.

### 1.1.1 Improve QED calculations and ab-initio calculations

The validity of the Standard Model relies strongly on the validity of the underlying theories, such as QED. It is therefore desirable to check the validity of this theory as precisely as possible. This can be done by comparing calculated transition frequencies against the results obtained by measurements. In order to ease the calculations of transition frequencies, the calculation of the energy of a specific state is expressed in orders of the fine structure constant  $\alpha$ :

$$E(\alpha) = \mathcal{E}^{(0)} + \alpha^2 \mathcal{E}^{(2)} + \alpha^3 \mathcal{E}^{(3)} + \alpha^4 \mathcal{E}^{(4)} + \alpha^5 \mathcal{E}^{(5)} + \dots \quad (1)$$

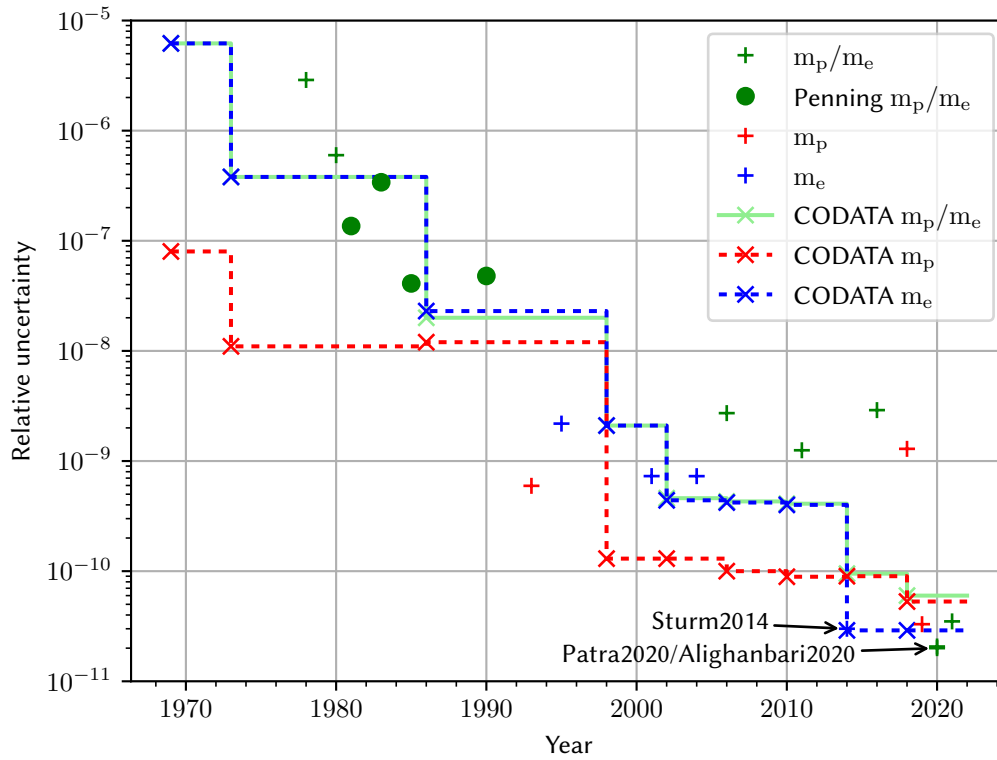
Term 0, which also depends on  $\alpha$ , is the non-relativistic energy and can be calculated up to 30 digits using the variational approach [3]. The term of order  $\alpha^2$  is called the leading order relativistic correction and contains, for example, terms for the recoil energy, the relativistic kinetic energy and the finite size of the nucleus [4, page 2, eq 7]. The term of order  $\alpha^3$  is called the leading order radiative correction and contains terms for quantum electrodynamics, such as for example the one-loop electron self energy, the anomalous magnetic moment and the one-loop vacuum polarization

[4, page 2, eq 14]. Terms in higher order of  $\alpha$  contain higher orders of some of the mentioned terms [5, page 2], second- or third loop contributions for some terms [6, page 6, eq 25] as well as additional terms which are relevant only in higher orders of  $\alpha$ , such as the Wichmann-Kroll contribution [7, 8]. The amounts contributed by the various orders are nicely listed in [4, page 5, table VI], [5, page 3, table III], [6, page 6, table I], [9, page 6, table I] and [10, page 581, table 2].

Note that some manuscripts express the order of  $\alpha$  in terms of masses, following a convention used mostly in atomic physics. The two ways to express the order of  $\alpha$  are related by [5, page 1 between eq 2 and 3]:

$$R_\infty \alpha^4 \sim m_e c^2 \alpha^6 \quad (2)$$

### 1.1.2 Determination of fundamental constants and their time variation



**Figure 1.2:** Development of the relative uncertainty of  $m_p/m_e$  over time. Solid and dashed lines: Uncertainty of CODATA recommended values for  $m_p/m_e$ ,  $m_p$  and  $m_e$ . Markers on the lines indicate the year for which the values were released. Green crosses: Uncertainties for values of  $m_p/m_e$  determined from measurements, excluding Penning trap measurements, which are shown as green dots. Red and blue crosses show the uncertainties for values of  $m_p$  and  $m_e$ , respectively. Up to the year 2014, the uncertainty of the CODATA values of  $m_p/m_e$  was mostly limited by the uncertainty of  $m_e$ , which was improved by an order of magnitude by Sturm2014[11]. Afterwards, the uncertainty of the CODATA values is limited mostly by  $m_p$ . The datapoints Sturm2014 [11], Patra2020 [12] and Alighanbari2020 [10] are indicated by arrows, because they are overlapping with other datapoints or with each other. References and plotted values are listed in table A.2.

The determination of the values of the physical constants is an inherent goal of metrology.

Official values of the physical constants are set and published by the CODATA consortium [1, 2, 13–19]. For each constant, published measurement results along with their uncertainties are reviewed and assigned weights based on their derived reliability. The value of the constants is then calculated from the weighted measurements using a least-square optimization and a combined confidence interval is assigned.

Within the CODATA publications, the masses of the electron and proton in atomic weights as well as the proton-to-electron mass ratio are labeled  $A_r(e)$ ,  $A_r(p)$  and  $A_r(p)/A_r(e)$ , respectively.

Figure 1.2 shows the improvement of the relative uncertainty in the determinations of the constants  $A_r(e)$ ,  $A_r(p)$  and  $A_r(p)/A_r(e)$  over time. For a reliable determination of the values, results from different measurement methods are desired. If they are consistent, the reliability of the final value is greatly increased. This helps to detect both possible systematic errors in single measurements as well as testing assumptions made in theoretical physics, like the validity of CPT [20]. For the determination of  $A_r(p)/A_r(e)$ , for example, strongly differing measurement methods are the determination via cyclotron-resonance frequency comparisons in Penning traps for electrons and single  $C^{6+}$  ions [21] and the determination via two-photon spectroscopy of antiprotonic helium (assuming that CPT holds) [20]. The determination of this constant from spectroscopy of molecular hydrogen ions is a good complementary tool, because it probes quite different physical effects.

In this thesis, the ratio  $m_p/m_e$  and the value of  $m_p$  are determined with the help of spectroscopy of cold molecular hydrogen ions.

In order to extract the values of physical constants from frequency measurements in molecular hydrogen ions, first a precise calculation of the transition frequency has to be performed, as outlined in the previous section. These calculations themselves depend on the values of physical constants. By combination of several transition frequencies, possibly of different isotopes, the number of required physical constants can in some cases be reduced.

Then, one can use the existing values of the physical constants, which are assumed to be “fixed”. The constant which one wants to determine is treated as a free parameter and is determined by fitting the expression for the transition frequency to the obtained measurement result. The uncertainty of the determination of the constant is then determined by the uncertainty of the remaining physical constants in the expression, the uncertainty in the theoretical calculation as well as the uncertainty of the measurement. Also, the determination of the constant implies that the involved molecular theory is valid. Results for the determination of  $m_p$  and  $m_p/m_e$  can be found in sections 5.1 and 5.2.2, respectively.

With enough precision, it is also possible to set limits on a possible variation of their values over time. Variations are possible on long (gigayear) [22] as well as short [23, 24] timescales. A relative inaccuracy of  $10^{-16}$  is desired in order to set limits on potential time variations of particle mass ratios [25, sec. 7, first paragraph]. Currently, limits for the change of fundamental constants are sought for via astrophysical measurements as well as via measurements using optical clocks.

Astrophysical measurements are based on the fact that light emitted from sources far away from earth basically allows us to look at the conditions in the universe at the time when the light was emitted. Usually, the absorption spectrum of an absorber, like a gas cloud, in front of a quasar is used as a light source. When the composition of the absorber is known, the expected spectrum can be modeled. The relative speed between the absorber and the earth has to be taken into account to accommodate for redshifts. From the distance of the absorber to the earth, the traveling time of the light, called “lookback time”, can be deduced. The estimated time it took for the light to reach us from the source depends on the model of evolution of the universe used. An evolution-independent expression for the distance is the redshift  $z$ .

Determining limits on the time evolution of physical constants by this method has some limitations. There is only a limited small number of suitable absorbers, and they are coincidentally

distributed over the sky [26]. Also, one can not easily differentiate between different physical conditions due to time and space.

The literature reports both null-results [27, 28], as well as rate limits in the range  $10^{-17}$  to low  $10^{-15}$  for relative changes in the proton-to-electron mass-ratio per year [28–50].

When optical clocks are used to search for changes in physical constants, two clocks based on different clock species are compared over time. The time evolution of the difference in their frequencies is proportional to [50, eq. 1]

$$v_{AB} = \frac{v_A}{v_B} \propto \alpha^{\lambda_\alpha} \cdot \mu^{\lambda_\mu} \cdot g_p^{\lambda_g}. \quad (3)$$

Here,  $\alpha$  is the fine-structure constant,  $\mu = m_p/m_e$  and  $g_p$  is the proton gyromagnetic ratio. The sensitivity coefficients  $\lambda_\mu = \frac{d \ln v_{AB}}{d \ln \mu}$  are different or even zero, depending on the systems compared. Using a set of measurements, constraints on the values can be obtained. Note, however, that in some assumptions on the evolution of the physical constants, the variations of the constants may not be independent.

In the case of optical clocks, both the time evolution and the evolution of earth through space are probed at the same time. Limits for the relative change of  $m_p/m_e$  obtained from optical clocks are in the low  $10^{-16}$  per year [51, 52].

The results of measurements done via optical clocks and via astrophysical methods can only be compared if an astrophysical evolution model is chosen, for example the dynamics of a scalar field [50].

### 1.1.3 Searching for physics beyond the Standard Model

The Standard Model does not include gravity. Several extensions have been introduced to overcome the problems of unification, for example string theory [53] or the concept of dark matter [23, 24].

Some extensions of Standard Model allow extra terms on gravity (non-Newtonian gravity, based on additional dimensions) [54] but also new forces between elementary particles. These new forces could be spin-dependent or spin-independent. A good review is provided in [55].

Both of these extensions have in common that they would provide extra force terms. Both the strength of these forces, relative to electroweak force, for example, as well as its defining length of scale are unknown. It is therefore necessary to put limits on combined sets of strengths and length scales. These tests can be done by observing different physical systems, which show a strong dependence on certain length scales. In the scope of this thesis, molecular ions are chosen to investigate length scales on the order of 1 Angstrom, in the range of the size of a molecule.

The tests are performed by measuring a transition frequency and comparing it to its theoretical value, supplied by the QED calculations. Then, an extra force term is added to the Schrödinger equation which describes the interaction of the particles.

The discrepancy between the predicted and the measured frequency values is then taken as an upper limit of an effect caused by the unknown force. Given an analytical expression for the force, a limit on its strength at the distance of the particles can be obtained.

In the case of molecular ions, it is desirable to have a large dependency of the transition frequency on the strength of the force. It is therefore favorable to analyze transitions with large  $\Delta v$ , where the wavefunctions of the respective states have little overlap [56, page 5 top left]. In this case, two different ranges with different strengths of the forces can be investigated. If the two wavefunctions are very similar, like for fundamental transitions, only a differential effect can be measured. In practice, the obtainable limits also depend on how well the transition frequency can be measured and how large the systematic errors are.



**1.1.3.1 Improve limits on the existence of a fifth force** Fifth forces can be assumed for a variety of interacting systems, like lepton-lepton, hadron-lepton (for example, electron-nucleon: [57]) and hadron-hadron [20], at a variety of scales. It is also possible that there are extra forces in the gravitational force [58, 59]. An overview of the deduced limits for a variety of scales can be found in [60, figure 3] and [10, figure 3].

As described above, for setting a limit on a potential force, an analytical expression of the assumed form of the force is required. One possible assumption for a fifth force is a Yukawa-type potential with an effective range  $\lambda$  [56, page 4, eq. (2)]:

$$V_5(r) = \beta' \frac{\exp(-r/\lambda)}{r} \hbar c = \beta' Y(r) \quad (4)$$

Here,  $\beta'$  is the coupling strength, which can be expressed relative to the coupling strength  $\alpha$  of the electromagnetic interaction. For the range of 1 Angstrom in hadron-hadron interactions considered in this thesis, the force-carrying particles would have masses on the order of  $2 \text{ keV}/c^2$ . In order to be able to compare the strengths in different molecular systems, a coupling strength normalized to the hadron number can be introduced:

$$\beta = \beta' / (N_1 \cdot N_2) \quad (5)$$

For a given discrepancy  $\delta E$  between experimental and theoretical results,  $\beta$  can be expressed as:

$$\beta < \frac{\delta E}{N_1 N_2 \Delta Y_\lambda}, \quad (6)$$

where  $\Delta Y_\lambda$  is the contribution of the Yukawa potential to the Schrödinger equation.

Results from spectroscopy of  $\text{HD}^+$  [61, 62] have been used to extract such limits [56, C, page 5].

**1.1.3.2 Limits on the size of other dimensions** The postulation of the existence of extra dimensions by the string-theory is in strong contradiction to our experience of the world so far. One possible explanation for this discrepancy is the assumption of compactified extra dimensions, outlined in the ADD-framework [54]. It can then be assumed that the gravitational force has extra terms, whose force-carriers can only be carried through the extra dimensions. Following the explanations in [63, section 2], the extra dimensions can be assigned a compactification radius  $R_n$ . At distances below this radius, extra gravitational terms can be felt, leading to a modified potential:

$$V_{ADD} = -\frac{m_1 \cdot m_2}{M_{(4+n)}^{n+2}} \cdot \frac{1}{r^{n+1}} \text{ for } r < R_n \quad (7)$$

At distances larger than the compactification radius, the potential has again the form of normal Newtonian gravity:

$$V_{ADD} = -\frac{m_1 \cdot m_2}{M_{(4+n)}^{n+2} (R_n)^n} \cdot \frac{1}{n} \text{ for } r \geq R_n, \quad (8)$$

where  $n$  is the number of extra dimensions above the known  $3 + 1$  dimensions. The effective Planck mass  $M_{Pl}^2 = M_{(4+n)}^{n+2} (R_n)^n$  is dependent on the number of extra dimensions.

The goal is now to set an upper limit for the value  $R_n$  for a given  $n$ . This limit can be derived from the obtained discrepancy between the expected theoretical value and the experimental result.

Another framework is laid out in the models RS-I and RS-II of Randall and Sundrum [64, 65], which are not based on compactified dimensions. Instead, a distance between the  $3+1$  dimensions and an extra dimension is established. The strength of the change in the gravitational force at small distances is then dependent on the distance between these dimensions.

## 1.2 Why cold ions?

Performing spectroscopy on cold ions has some advantages over spectroscopy in the gas phase. When trapped in an ion trap, ions can be cooled down to the mK range. This greatly reduces the Doppler broadening [66, p. 137, eq 5.36]

$$\Delta\nu_D = 2\frac{\nu_0}{c}\sqrt{\frac{2kT}{m}}\ln 2 \quad (9)$$

For a fundamental transition at 5.1  $\mu\text{m}$  in  $\text{HD}^+$ , the Doppler broadening at room temperature of 420 MHz is reduced to 3.4 MHz at 20 mK.

Another advantage is the reduced transit time broadening. Since the ions are located inside the trap, the high lifetimes of their levels can be exploited.

The effect of first-order Doppler broadening can be suppressed by constraining the ions to a volume of width  $a$ , which is significantly smaller than the wavelength  $\lambda$  of the interrogating radiation:

$$a \ll \lambda/2\pi \quad (10)$$

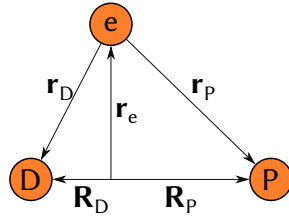
This is the so-called Lamb-Dicke regime [67]. The spectroscopic signal obtained from ions in this state will show a Doppler broadened background signal, with a narrow, Doppler-free peak on it. The strength of the Doppler-free signal with respect to the background signal depends on how strong the interaction fits into the Lamb-Dicke regime.

In order to reach this regime for wavelengths near the visible range, ions are usually trapped in an RF trap with tight confinement [68], combined with cooling them in the resolved-sideband regime [69, 70]. A trap fulfills the condition for resolved sidebands if the oscillatory frequency of a particle in the trap is larger than the natural linewidth of the cooling transition used to cool the particle. In this regime, Raman-sideband cooling can be applied to cool the particle to the motional ground state of the trap. With careful design of the trap, the volume in which the particle is then trapped can be smaller than 1  $\mu\text{m}$ , allowing the application of the Lamb-Dicke regime in the near-IR and possibly extending it into the visible range.

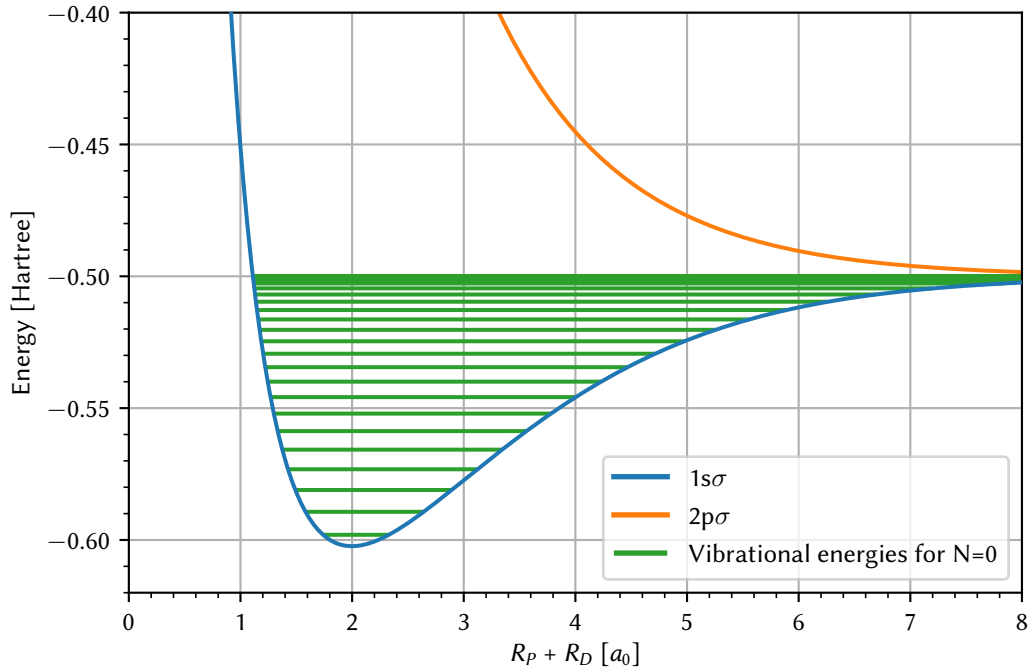
## 2 The molecular ion $\text{HD}^+$

The molecular ion  $\text{HD}^+$  is the simplest molecule, with only three components: the electron, the proton, and the deuteron, as shown in figure 2.1. In order to describe the energy levels of this molecule, the three-body-problem has to be solved. The electronic potential of the molecule is shown in figure 2.2. Only the potential energy curve for the  $1s\sigma$  level is stable, while already the  $2p\sigma$  level does not constitute a bound state. This allows dissociation of the molecule by exciting it from the  $1s\sigma$  level to the  $2p\sigma$  level using UV light. The rotational-vibrational level structure of the molecule relevant to this thesis is shown in figure 2.3.

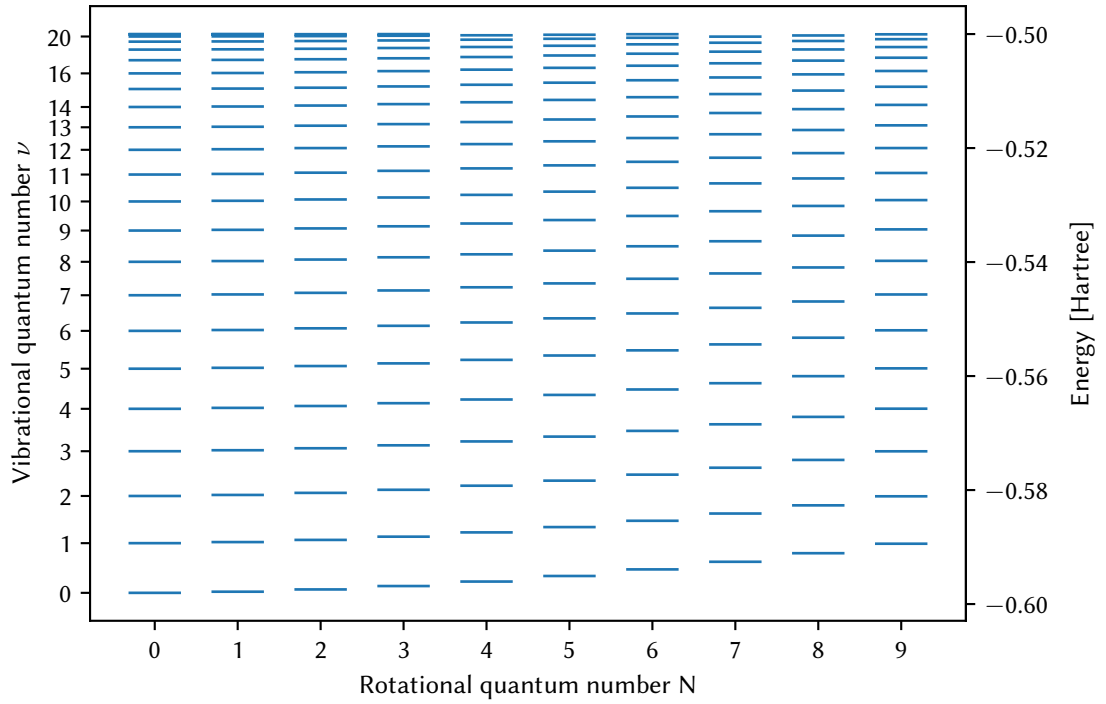
When the ion is trapped in an ion trap and cooled to roughly 20 mK, the vibrational levels “freeze out” and only the lowest level  $v = 0$  is occupied. The state distribution in the respective rotational states is governed by the black-body radiation of the surrounding environment. For an ion trap with a vacuum chamber at room temperature, only the lowest seven rotational levels are populated [71, Section II.A, eq 1]. More than 50% of the population can be found in the rotational levels  $N=1$  and  $N=2$  [72, fig. 1].



**Figure 2.1:** The  $\text{HD}^+$  molecular ion, notation like in [73, page 2 top left]:  $\mathbf{R}_P, \mathbf{R}_D, \mathbf{r}_e$ : Particle positions relative to center-of-mass of the molecule of proton, deuteron and electron, respectively.  $\mathbf{r}_P = \mathbf{R}_P - \mathbf{r}_e$ ,  $\mathbf{r}_D = \mathbf{R}_D - \mathbf{r}_e$  are the coordinates relative to the electron.



**Figure 2.2:** Electronic potential of  $\text{HD}^+$  as calculated by [74], overlaid with vibrational energy levels from [75].



**Figure 2.3:** Ro-vibrational structure of the  $\text{HD}^+$  molecular ion without hyperfine structure as calculated by [75]. The quantum numbers are  $\nu$  for vibrational levels and  $N$  for rotational levels. Note that in some publications, the rotational quantum number is referred to as  $L$  ([73]).

Due to coupling of the electron spin to the nuclear spins, the level structure is further expanded into hyperfine structure. The angular momentum coupling scheme for low values of  $N$  is as follows [73, eq. (5)]:

$$\mathbf{F} = \mathbf{I}_p + \mathbf{S}_e, \quad \mathbf{S} = \mathbf{F} + \mathbf{I}_d, \quad \mathbf{J} = \mathbf{N} + \mathbf{S} \quad (11)$$

with the electron spin  $S_e = 1/2$  and the nuclear spins  $I_p = 1/2$  and  $I_d = 1$  for the proton and deuteron, respectively. The spins of proton and electron couple to the combined state  $F$ , which is further split up by coupling to the deuteron spin. The final splitting of the structure is caused by the coupling to the total orbital momentum  $N$ .

In the states with  $N = 0$ , there are four hyperfine levels, while there are 10 in the states with  $N = 1$  and 12 in the states with  $N = 2$  [25, table 2]. The hyperfine structure of the levels ( $v = 0, N = 0$ ) and ( $v = 1, N = 1$ ) are shown in figure 2 on page 62. The  $N=0$  level is therefore more suitable as a starting level for spectroscopy, since the populations in the individual hyperfine levels are higher.

The spectrum is split further in magnetic fields, which in practice are always present. The coupling to the magnetic field is described by the quantum number  $J_Z$ . The strength of the splitting of the energy levels due to the magnetic field is composed of a linear and a quadratic term, for some states there is also a non-negligible cubic term [25, eq (5) and text below]. Precise knowledge about the Zeeman effect is necessary to decide which transitions are most suitable for spectroscopy, namely those with low magnetic field dependency. Transitions with a high magnetic field dependency are useful for checking systematics of the spectroscopy system.

### 3 Spectroscopic sources

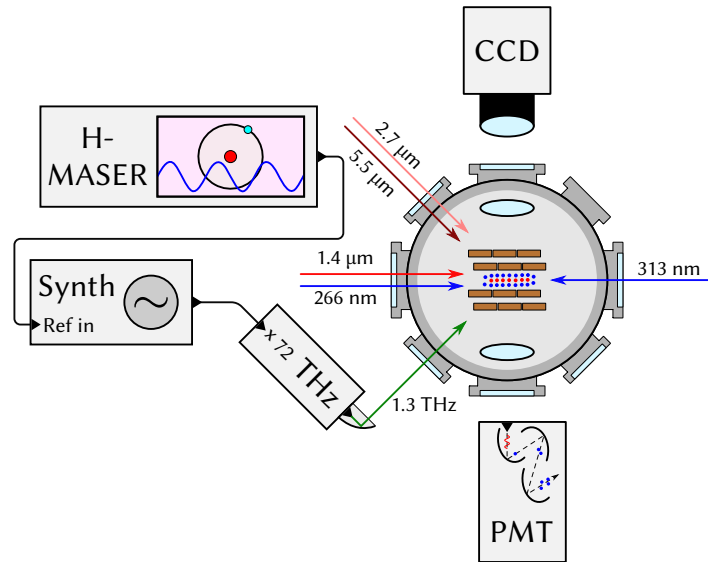
In this section, the spectroscopic sources used in this thesis are presented.

#### 3.1 THz source at 1.3 THz

The THz source used as a spectroscopic source in this thesis emits radiation at 1.31 THz, suitable for spectroscopy of the ( $v = 0, N = 0$ )  $\rightarrow$  ( $0, 1$ ) purely rotational transition in  $\text{HD}^+$ . Its wavelength of roughly 0.2 mm is expected to be larger than the region in which the ions are confined to in the trap. Therefore, it should enable spectroscopy in the Lamb-Dicke regime [67], where the Doppler broadening is suppressed. The source is based on a multiplier and amplifier chain with a total multiplication factor of 72. When seeded with a microwave source of a few mW at roughly 18 GHz, it produces a few  $\mu\text{W}$  at 1.31 THz. Since the upmultiplication is detrimental to the phase noise and therefore the final linewidth of the source, high quality synthesizers with high quality references have to be used for seeding it.

The source has been previously characterized by performing a beat with another source in the same frequency range, indicating a linewidth below 10 Hz when using the internal frequency references of the synthesizers used for seeding [76].

The complete THz setup is shown in figure 3.1. Here, the synthesizer which seeds the THz source is referenced to one of the hydrogen masers in the institute. The long-term accuracy of the maser is therefore transferred onto the synthesizer. Since the synthesizer is referenced to the maser, its short-term stability should also be improved. However, the detailed transfer function of the phase-lock to the reference inside the synthesizer is unknown and therefore no estimations of the linewidth of the synthesizer at 18 GHz can be made. One possible way to investigate the linewidth would be the use of a microwave spectrum analyzer, but such a device with sufficient resolution is not available



**Figure 3.1:** Setup of THz source used for rotational spectroscopy with THz source at  $45^\circ$  towards the crystal. Green: lasers for cooling and spectroscopy, red: THz radiation, black: electrical connections.

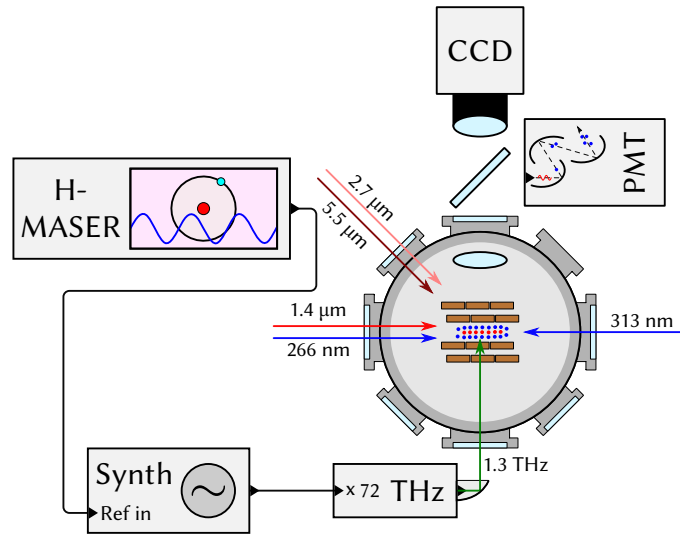
in the institute. Therefore, an alternative way of investigating the linewidth was used, as outlined in the next subsection.

The optical part of the experimental setup is similar to the other  $\text{HD}^+$  spectroscopy themes presented in this thesis. The Beryllium cooling laser is irradiated into the trap from the right hand side, while the REMPD lasers at  $1.4\ \mu\text{m}$  and  $266\ \text{nm}$  are irradiated from the left hand side. Optical state preparation lasers are irradiated under a  $45^\circ$  angle. The initial THz experiments were performed by irradiating the THz radiation under a  $45^\circ$  angle into the ion-trap. This arrangement was due to space constraints. With this setup, it was shown that the THz transition in  $\text{HD}^+$  can be driven, but no high resolution spectroscopy was performed. The results of these measurements are summarized in section 5.1.

Later, the optical setup was changed such that the PMT and the camera could observe the ions from the same port of the vacuum window, as shown in figure 3.2. This allowed irradiation of the THz radiation onto the ions perpendicular to the trap axes. Seen from this direction, the ions take the form of a thin cylinder. In the direction of the beam, the ions are therefore much tighter confined than from the  $45^\circ$  position, where the radiation is irradiated onto a projection of the  $\text{HD}^+$  ion cylinder. With this setup, high resolution spectroscopy became possible, as reported in section 5.1.

### 3.1.1 Characterization of synthesizer linewidths

In order to set a lower limit for the linewidth of the THz source, the linewidth of the synthesizer which seeds it has to be known. The setup for the determination of the synthesizer linewidth is shown in figure 3.3. Since no high resolution microwave spectrum analyzer was available, a low frequency (up to  $100\ \text{kHz}$ ) spectrum analyser had to be used. In order to transfer the synthesizer output at  $18\ \text{GHz}$  down into the frequency range of the spectrum analyzer, it has to be downmixed using another microwave source. The synthesizer is operated in the region of the target frequency and its output is sent to a microwave mixer. The second RF source for downmixing is generated using an optical frequency comb, which is phase-locked to an ultrastable reference laser at  $1.5\ \mu\text{m}$ . The phase-lock transfers the linewidth and frequency stability properties of the reference laser onto



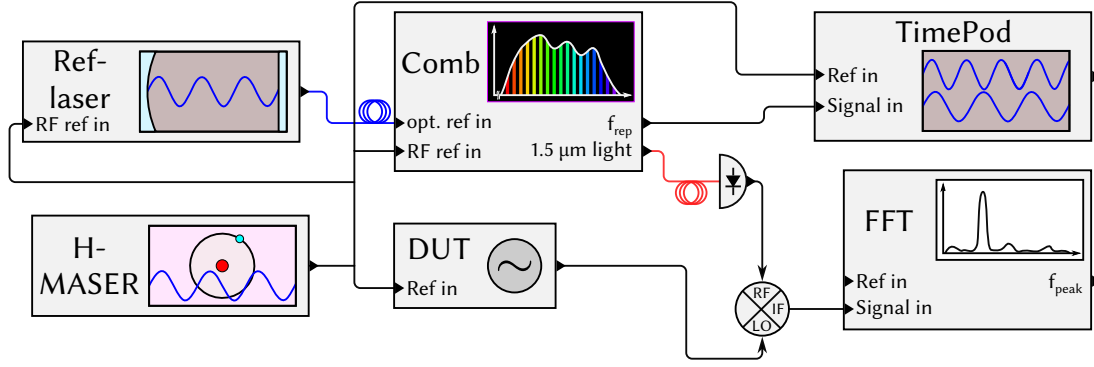
**Figure 3.2:** Setup of THz source used for rotational spectroscopy with THz source at  $90^\circ$  towards the crystal for spectroscopy in the Lamb-Dicke regime. Green: lasers for cooling and spectroscopy, red: THz radiation, black: electrical connections.

the comb teeth. The repetition rate of the frequency comb becomes therefore very stable and narrow as well. The carrier envelope offset frequency is phase-locked to an RF reference. Another  $1.5 \mu\text{m}$  output port of the frequency comb is now directed onto a fast photodiode, which can receive high harmonics of the repetition rate and convert them to an RF signal. In order to downmix the 18 GHz synthesizer to the kHz range, the 73rd harmonic of the  $\sim 250 \text{ MHz}$  repetition rate is chosen. It is important to note here, that using the 73rd harmonic of the repetition rate does not significantly deteriorate its phase noise, since the frequency stability of the repetition rate is controlled by the phase-lock to the reference laser. The phase-lock operates at  $1.5 \mu\text{m}$  and therefore acts on roughly the 800.000th harmonic of the repetition rate. By setting the synthesizer to an appropriate frequency offset to the 73rd harmonic of the repetition rate, a downmixed signal at several kHz is created. The spectral width of this signal is a combination of the individual linewidths of the synthesizer and the harmonic of the repetition rate.

The resulting spectrum of the downmixed signal is shown in figure 3.4. The full-width-half-maximum of this signal is  $2.3 \text{ mHz}$ , as shown by the blue curve in the plot on the right hand side. The recording of the spectrum took 2000 s.

As stated earlier, the frequency stability of the reference laser is transferred onto the repetition rate. However, the frequency stability of the reference laser is not perfect and therefore its frequency drift is converted into a frequency drift of the repetition rate. The expected drift of the downmixed signal due to the drift of the repetition rate is shown in figure 3.5. The 10 minute drift cycles are probably due to a pickup of the a local oscillator signal into the frequency counting device (TimePod) and a drift of that signal due to air conditioning cycles.

The drift determined via the fit (horizontal orange line in figure 3.4) is smaller than the linewidth resulting from the spectral analysis. After applying a 10 s moving average in order to reduce spikes, a histogram (orange curve) of the frequency drift overlaps nicely with spectrum obtained via FFT. A 10 s moving average is also shown (green). Their width is on the same order as the width of the downmixed signal recorded via spectrum analysis. This indicates that the width of the observed spectrum could be limited by the residual drift of the reference laser. The drift of the reference laser could in principle be removed by an active frequency stabilization based on the measured frequency, using an AOM between the laser and its cavity as an actuator. This has been shown to work before



**Figure 3.3:** Setup for linewidth analysis of the synthesizer. All synthesizers used for stabilization of the RT-ULE laser, all synthesizers and counters in the frequency comb, the Timepod, and the DUT are referenced to the maser (connections omitted for clarity). The FFT is not referenced to the maser, due to a lacking reference input. Red lines: fibers with  $1.5\ \mu\text{m}$  light, black lines: electrical connections. The frequency comb is phase-locked to the optical reference RT-ULE. The Timepod is used to count its repetition rate.

for another reference laser by U. Rosowski and I. Ernsting.

With the current spectrum analyzer, the resolution of the spectrum can not be easily increased for technical reasons.

Assuming no additional linewidth broadening inside the THz source except for the broadening due to the upmultiplication, the resulting lower limit for the THz linewidth is:

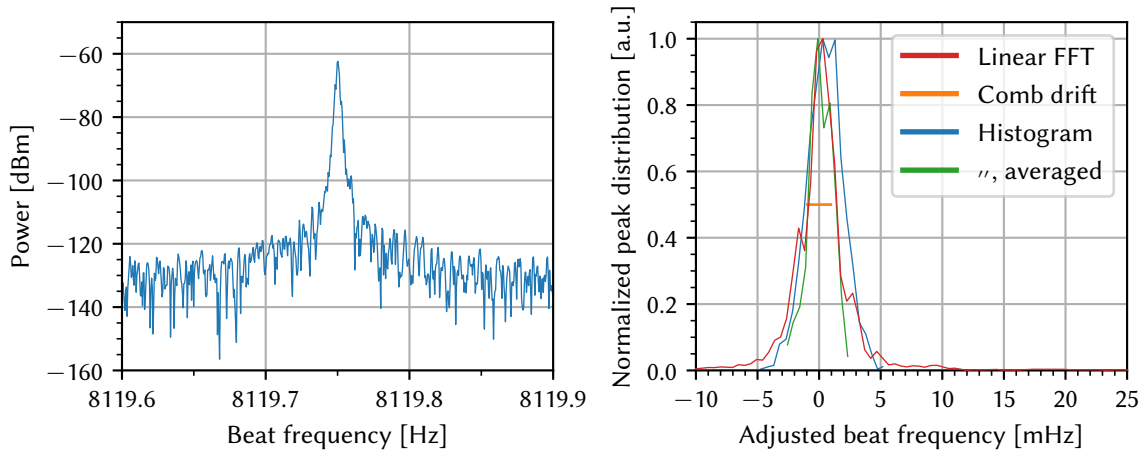
$$2.3\ \text{mHz} \cdot 72 = 166\ \text{mHz} \quad (12)$$

This number is lower than the number reported in [77], which is based on earlier results from this measurement. This linewidth sets the lower limit for the fractional resolution of the THz source to:

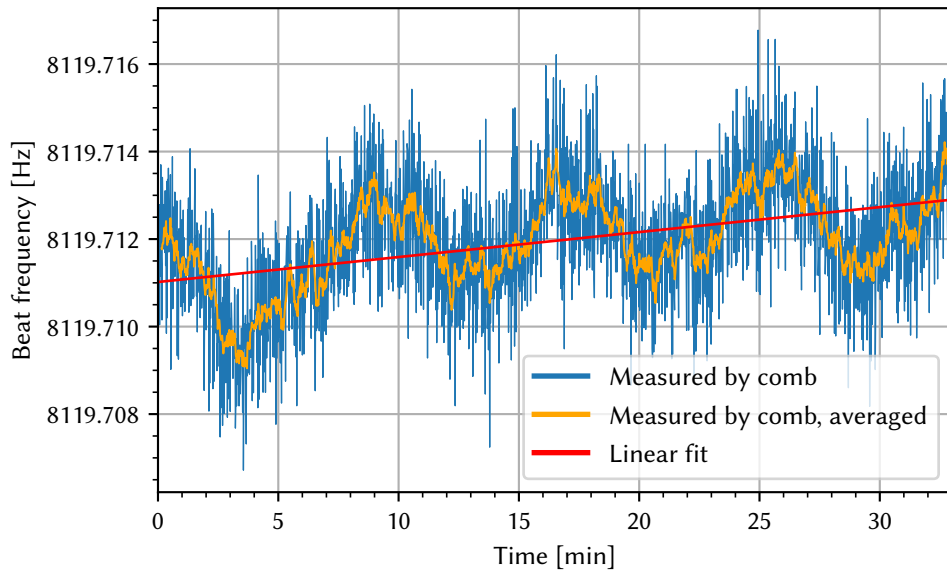
$$\frac{166\ \text{mHz}}{1.31\ \text{THz}} = 1.3 \times 10^{-13} \quad (13)$$

Recent results of spectroscopy at higher resolution [10] have reached a fractional resolution of  $3 \times 10^{-12}$  and are therefore not yet limited by the concluded linewidth of the THz source.





**Figure 3.4:** Spectrum of E8241A running at  $\sim 18$  GHz downmixed to  $\sim 8$  kHz by beating it with the 73rd harmonic of the optical frequency comb. Linewidth: 2.3 mHz FWHM. Resolution bandwidth: 488.3  $\mu$ Hz, acquisition time: 2000 s. Left: logarithmic scale. Right: Linear scale. Blue: result of spectrum analysis, orange: beat shape expected from a histogram of comb repetition rate, green: beat shape expected from comb repetition rate averaged with moving average of 10 s, red line: expected linewidth from linear fit to comb drift. Details of comb drift are shown in figure 3.5.



**Figure 3.5:** Calculated drift of the downmixed signal due to the drift of the repetition rate of the optical frequency comb. The drift is due to a drift of the reference laser. Blue: no averaging, orange: 10 s moving average, green: linear fit through original data.

## 3.2 Quantum cascade laser at 5.4 $\mu\text{m}$

Quantum cascade lasers are favorable spectroscopy sources for the mid-IR, due to their high output power and simple operation. In recent years, various approaches for absolute frequency stabilization and linewidth-narrowing of QCLs have been reported in the literature [78]. In this thesis, a quantum cascade laser was linewidth-narrowed and absolutely frequency stabilized, as described in two publications [79, 80]. This section contains some more details about these systems which are not in the publications.

### 3.2.1 Sum-frequency generation using OP:GaAs

In this thesis, the frequency of a QCL is measured with a near-IR fiber-based frequency comb. In order to move the frequency of the QCL into the spectral region accessible to the frequency comb, its radiation was upconverted to 1.2  $\mu\text{m}$  by sum-frequency generation using a laser at 1.5  $\mu\text{m}$ :

$$f_{\text{QCL}} + f_{1.5\mu\text{m}} = f_{1.2\mu\text{m}} \quad (14)$$

Sum-frequency generation was performed in a non-linear optical crystal. In the mid-IR, where the QCL emits, GaAs is a suitable material for non-linear optical processes. It has a very large non-linear coefficient of  $\sim 100 \text{ pm/V}$ , high transparency in the 1 – 16  $\mu\text{m}$  region and a high laser damage threshold, due to its good thermal conductivity [81, section 2]. The GaAs crystals used in this thesis have been produced by Arnaud Grisard, Eric Lallier and Bruno Gérard [81, 82].

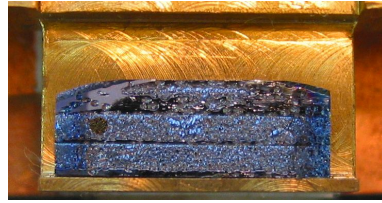
The production of GaAs crystals, however, requires more effort than the production of materials used in the near-IR, like PPLN. Efficient generation of radiation via non-linear processes requires good phase-matching of the involved radiation. In case of GaAs, phase-matching is achieved via quasi-phase matching (QPM). Since it is an isotropic material, QPM can not be performed via periodic poling like in PPLN. Instead, the crystallographic orientation has to be changed in order to change the sign of the phase-matching process. This process is called orientational patterning (OP). Crystals are created by first constructing a template wafer, which is constructed from manually aligned one period wide pieces of crystal. The actual crystal is then grown on the template by means of Hydride Vapour Phase Epitaxy (HVPE) until a suitable height of the crystal is reached. Since the templates can not be created with arbitrarily small regions, high-order QPM has to be used for some wavelength ranges. This is unfortunately detrimental to the conversion efficiency.

Another side effect of the growth process is that tiny backreflections on OP-interfaces can cause counter-directional modes in ring cavities [82, p. 1654, below fig. 5]. The back-reflections can also be detrimental to QCL applications, because they can cause optical feedback to the laser.

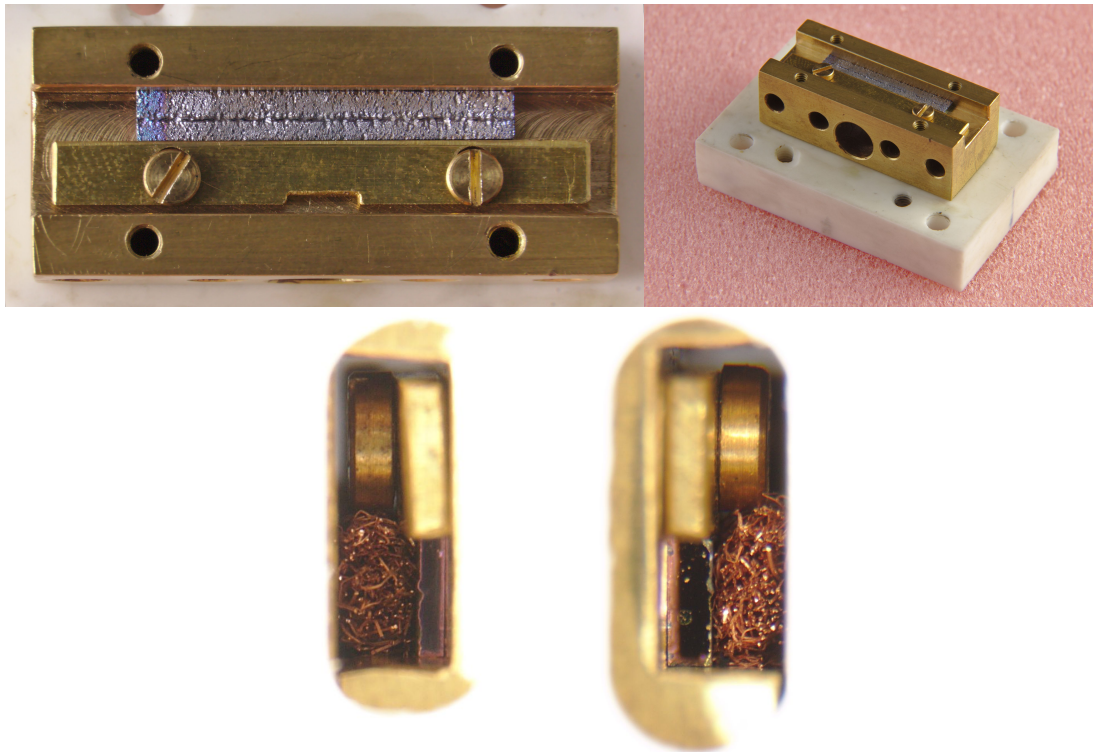
Figure 3.6 shows a photo of the OP-GaAs crystal used with the 5.4  $\mu\text{m}$  QCL. Two OP-zones with different periods can be seen. The top surface of the crystal is not flat. Therefore, care must be taken when fixing it in the oven using a spring.

For crystals with flat cut sides, a better way of mounting them is by pressing on them from the side. An oven following this idea suggested by Arnaud Grisard is shown in figure 3.7. The free space above the crystal is filled with copper wool in order to improve thermalization.

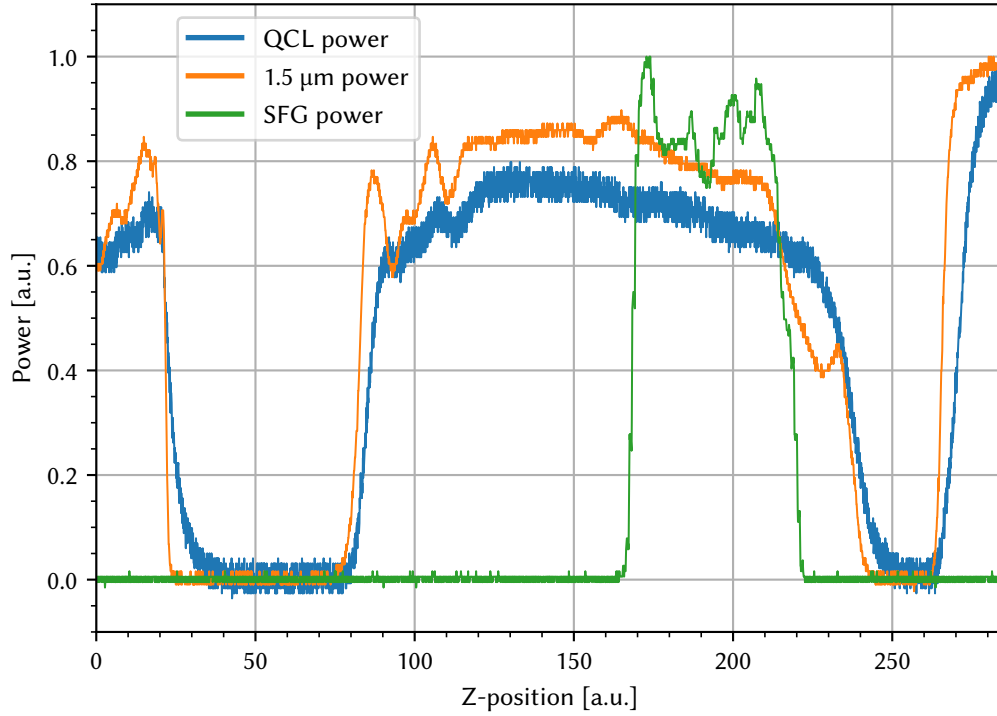
Since the OP-GaAs growth process is not completely uniform, conversion efficiency varies across the crystal. Figure 3.8 shows how the conversion efficiency changes by about 20% as the crystal is shifted orthogonally to the overlapped laser beams.



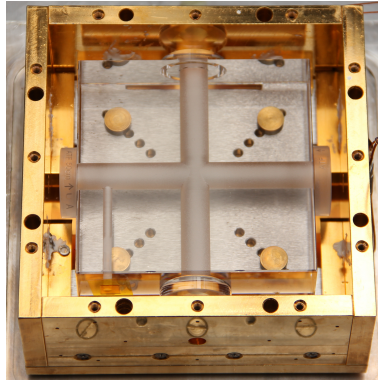
**Figure 3.6:** GaAs crystal in the open oven, seen from top. The top part of the crystal is a bulk area without orientational patterning. The two regions below, separated by a horizontal groove, are orientationally patterned zones.



**Figure 3.7:** Photo of the new oven design based on suggestions from Arnaud Grisard. Top left: Top view of the crystal in the oven. The OP-grating can be seen in the upper part of the crystal. The crystal is held in place by the rod below it. Top right: View of the oven on its MACOR holder. Bottom: Side views into the closed oven. The space above the oven is filled with copper wool. It can be seen that the crystal has different heights on each side.



**Figure 3.8:** Scan through a GaAs crystal in lateral direction. The crystal is moved vertically through the overlapped beams. Since the crystal was moved by turning the micrometer screw by hand, the Z-position axes can only serve as a rough guide. The scan starts in the empty region above the crystal. The transmitted power subsequently drops to zero because the beams hit the slightly rounded bulk region of the crystal. The transmitted power rises again as the beams pass through the OP-zones. In the top zone, no sum-frequency light is produced since no phase-matching is achieved. The transition between the different zones (indicated by a groove in figure 3.6) can not be observed in the transmitted power. As the beams enter the lower OP-zone, sum-frequency light is generated. The intensity is position-dependent with a 20% change, indicating a slightly non-uniform manufacturing process. After the second OP-zone, the beams are blocked by the lower side of the oven enclosure and the transmitted power rises to maximum as the oven moves out of the beams. The 1.5  $\mu\text{m}$  beam has a power of roughly 235 mW and the QCL power is 24 mW. The sum-frequency signal is detected using a lock-in amplifier. The QCL beam is chopped in order to produce a time-varying sum-frequency signal which the lock-in amplifier can detect.



**Figure 3.9:** ULE cavity block with high finesse mirrors in the inner temperature stabilization box.

### 3.2.2 Lock-guard for stabilization of QCL to ULE

The system presented in this section was developed together with Qun-Feng Chen and Evangelos Magoulakis.

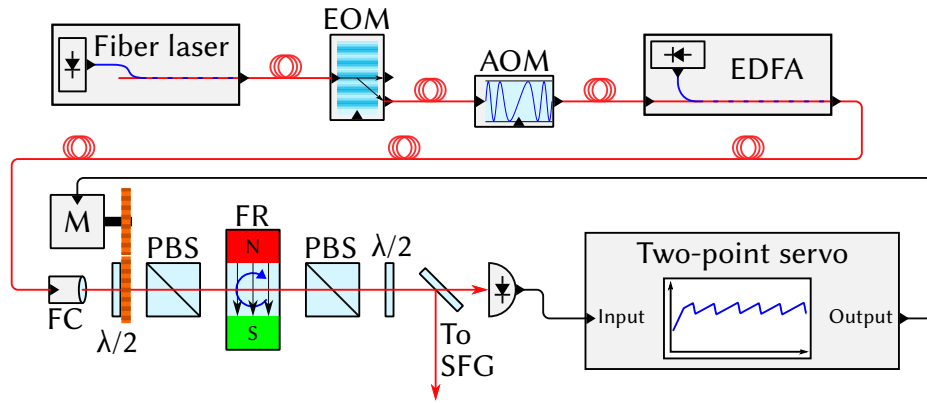
The quantum cascade laser at  $5.4\text{ }\mu\text{m}$  is stabilized to the ULE cavity shown in figure 3.9 using the sum-frequency signal at  $1.2\text{ }\mu\text{m}$ . The locking setup used for this laser is shown in figure 3.10 and follows a common strategy for laser locking: A fast servo with limited integrators acts directly on the laser diode current via a bypass, while the slow servo with unlimited, slower integrators acts on the current via the current driver. During the configuration of the locking servo it was noticed that the QCL is sometimes very “jumpy” and has lots of frequency jumps. The exact origins of this erratic behavior could not be determined. Since the laser also showed large and fast drifts, locking it with only the fast, limited lock did not work for long enough times to be able to optimize the locking setup. The laser drifted out of the limited locking range too quickly. Adding the slow locking servo extended this locking range, but due to the frequent jumps of the laser, the slow integrator would wind up to its limit and drive the laser away from the lock point for good.

Therefore, a mechanism was sought to keep the fast lock active at all times, but to “freeze” the slow integrator as soon as the laser jumped away from the lock point and to resume integration once the laser fell back into the range of the fast servo. The mechanism was termed “lock guard”. Figure 3.10 its integration into the slow locking circuit. The lock guard monitors the DC output voltage of the transmission photo detector. If that value falls below a configurable setpoint, a switch in the input path of the slow integrator is opened. Since the slow integrator receives no further error voltage, it keeps its current voltage. When the laser jumps back into the capture range of the fast lock, the signal on the transmission photo diode rises again and the switch is closed. The system can also handle a short interruption of the beam path of a few seconds and resume locked operation later.

Figure 3.11 shows the circuit diagram of the lock guard. A comparator (LM360, Texas Instruments) compares the photo diode monitor signal against the output of a configurable voltage divider. The output of the comparator is then used to control three CMOS switches (ADG1211, Analog Devices). One switch turns on a control LED to indicate a locked state, a second switch is used to interrupt the input of the slow integrator via the connector P4. A third switch is reserved for implementing a monitoring of the locked state via a TTL input to the measurement computer (connector P5). A manual switch allows overriding the lock guard.







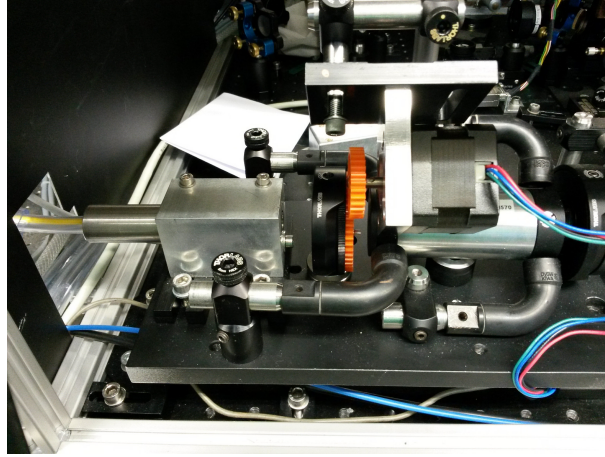
**Figure 3.12:** Parts of the QCL SFG setup relevant to polarization stabilization.

for proper modulation. Both of this was mostly the case after the fibers had settled after movement and proper alignment of the fiber twisters. The optical isolator behind the output collimator of the EDFA, however now converts the remaining polarization changes into power changes. These power changes have a double penalty: first, the loss in power reduces the strength of the generated sum-frequency signal. Second, due to the absorption of the  $1.5\ \mu\text{m}$  light in the non-linear crystal, a power change leads to a change of the local temperature in the crystal, shifting the quasi-phase-matching temperature and therefore lowering the conversion efficiency.

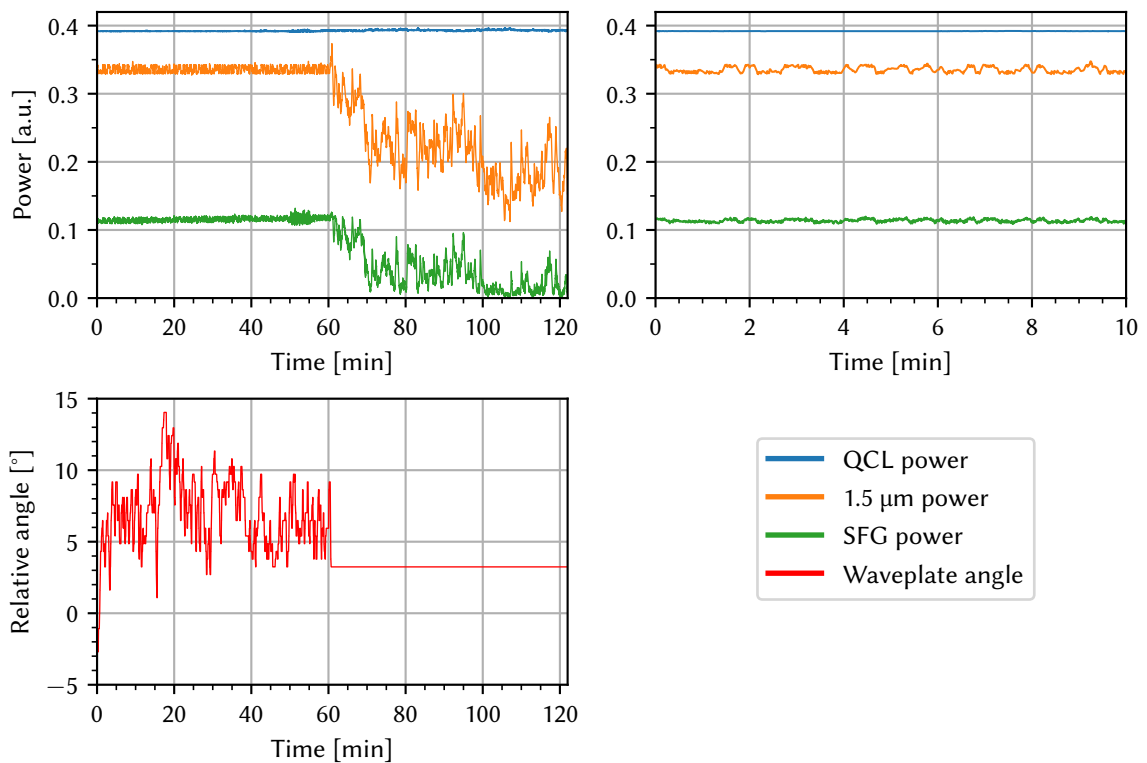
Therefore, the polarization of the light in front of the optical isolator had to be actively stabilized. Since the optical isolator converts polarization changes to power changes, a photo diode behind a dielectric mirror can be used as a monitor for the polarization state. A waveplate in front of the optical isolator is used as an actuator and rotated via a stepper motor. Figure 3.13 shows how the stepper motor (400 steps per rotation, RS PRO 535-0401) is connected to the waveplate's holder. Luckily, a gear was found which can be easily fit into the holder instead of the built-in scale. An microcontroller (ATMega168, Atmel) controls the motor via a stepper motor driver chip (TMC246, Trinamic) and allows the user to move the motor via a connected rotary encoder. The waveplate is turned by the user to a few percent below the maximum transmission of the optical isolator. When the stabilization is engaged, the current power level is used as the setpoint for a two-point stabilization system. An additional switch controls the sign of the lock.

Since the stabilization is on the slope of the instead of the maximum, no dithering is needed to determine the target direction. By lowering the setpoint a bit further, additional headroom is created to accomodate for partially elliptic polarization. For example, when the power of the  $1.5\ \mu\text{m}$  beam behind the crystal was measured to be  $6.5\ \text{W}$ , the setpoint was usually set to  $6\ \text{W}$ . At this point, sufficient sum-frequency signal for locking to the cavity was obtained and a decent amount of elliptic polarization could be tolerated.

Figure 3.14 shows the power stabilization in action. The recording was made when an especially badly matching collection of fiber-based components was used during the inital setup. During the first 60 minutes, the polarization stabilization is on. The zoomed plot shows the remaining fluctuations within the two-point stabilization regime. The relative waveplate angle is also shown and indicates that the system is quite active. When the stabilization is turned off, the decay in both  $1.5\ \mu\text{m}$  and  $1.2\ \mu\text{m}$  power can be seen.



**Figure 3.13:** Photo of motor actuator XXX find original image XXX

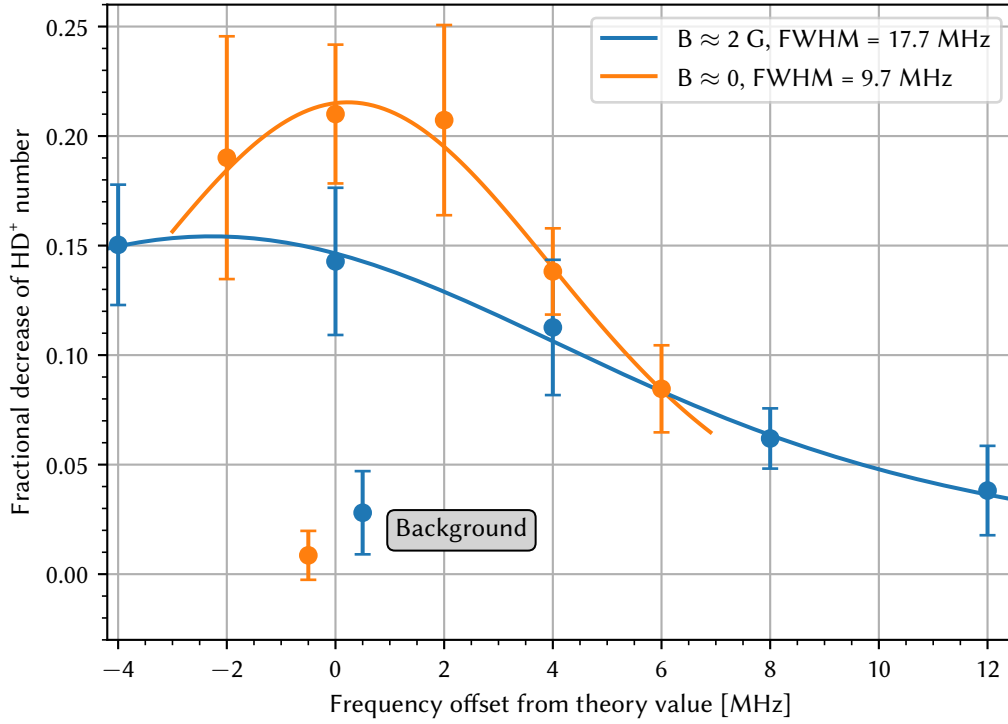


**Figure 3.14:** Power stabilization of the SFG setup. Points averaged over 0.5 s. Top (left and right): QCL power (blue), 1.5 μm laser power (orange), SFG power (green). The top right plot shows a magnification of the first 10 minutes. The effect of the two-point stabilization system can be seen. The residual instabilities of the 1.5 μm and SFG powers over this timespan shown on the right are 5.8 % and 9.5 %, respectively. Bottom left: Relative angle of the waveplate which is used to correct the polarization drift. The power stabilization is turned off after roughly 60 minutes. The fluctuations in the SFG power are stronger than in the 1.5 μm power because in addition to the power loss for the non-linear process, the absorbed power in the crystal is reduced. This reduces the local crystal temperature and therefore affects the phase matching conditions negatively.



### 3.2.4 Demonstration of spectroscopy

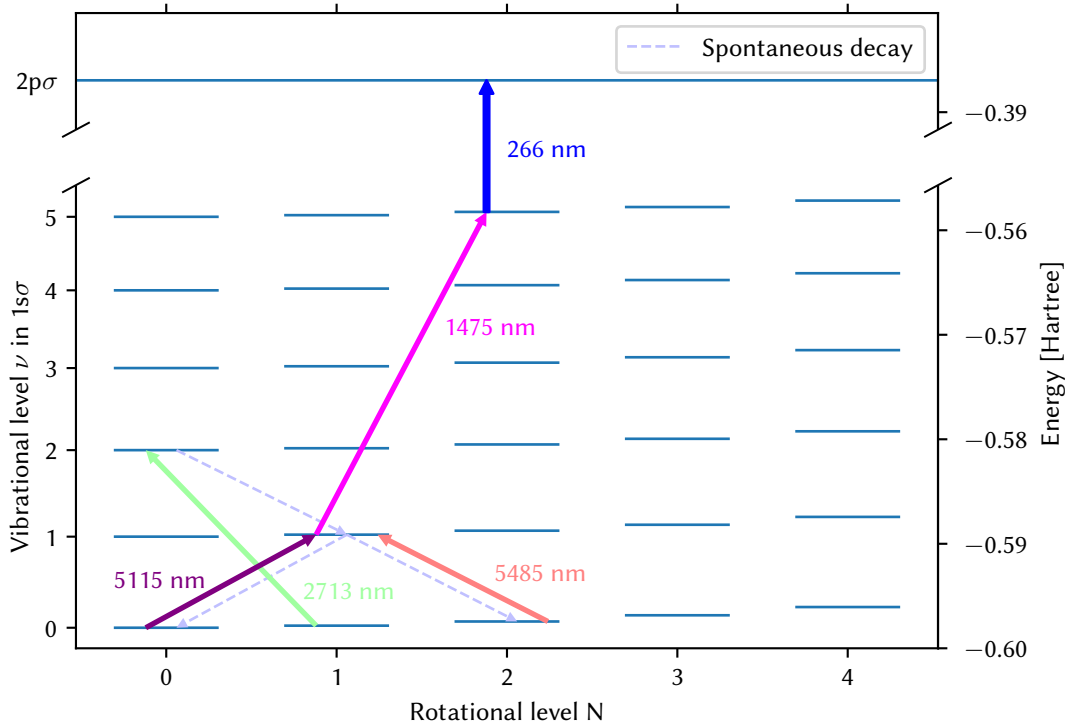
The source was employed to record a Doppler-broadened spectrum of the  $\text{HD}^+$  transition ( $v = 0, N = 1$ )  $\rightarrow$  ( $1, 0$ ) at two different magnetic field strengths, as shown in figure 3.15. The spectroscopy laser was sent into the trap in the axial direction, therefore no Lamb-Dicke regime can be expected, as shown in [77]. The minimum width of the transition due to Doppler broadening according to formula 9 is 3.3 MHz. The spectrum is not extended beyond -4 MHz, because other hyperfine transitions lie in the vicinity. The spectrum obtained for nominally zero magnetic field is still wider than the minimum set by the Doppler broadening, possibly due to power broadening.



**Figure 3.15:** Spectrum of the ( $v = 0, N = 1$ )  $\rightarrow$  ( $1, 0$ ) transition, hyperfine line ( $F = 1, S = 2, J = 1$ )  $\rightarrow$  ( $1, 2, 2$ ) (notation following 11) at 26.27 MHz from the spin-free frequency. Full width at half maximum at nominally zero magnetic field is 9.7 MHz, and 17.7 MHz at  $B \approx 2$  G.

### 3.3 Difference-frequency generation based sources for 5.1 $\mu\text{m}$

The ( $v = 0, N = 0$ )  $\rightarrow$  ( $1, 1$ ) transition in  $\text{HD}^+$  has a wavelength of 5.1  $\mu\text{m}$ . Its lower level, ( $v = 0, N = 0$ ), is also the starting level for the THz spectroscopy. Therefore, the same laser systems which were used for rotational cooling can be used in order to prepare a sufficient population in this state for spectroscopy. The spectroscopy scheme is shown in figure 3.16. The QCL at 5485 nm and the DFB laser at 2713 nm are used to populate the lower spectroscopy level ( $v = 0, N = 0$ ). Detection of the spectroscopy signal is done via REMPD: Once ions are excited into the ( $v = 1, N = 1$ ) state by the spectroscopy laser, they are transferred into the ( $v = 2, N = 5$ ) level from where they are dissociated using a 266 nm laser.



**Figure 3.16:** Spectroscopy scheme for the  $(v = 0, N = 0) \rightarrow (1, 1)$  transition.

### 3.3.1 First-generation 5.1 $\mu\text{m}$ source

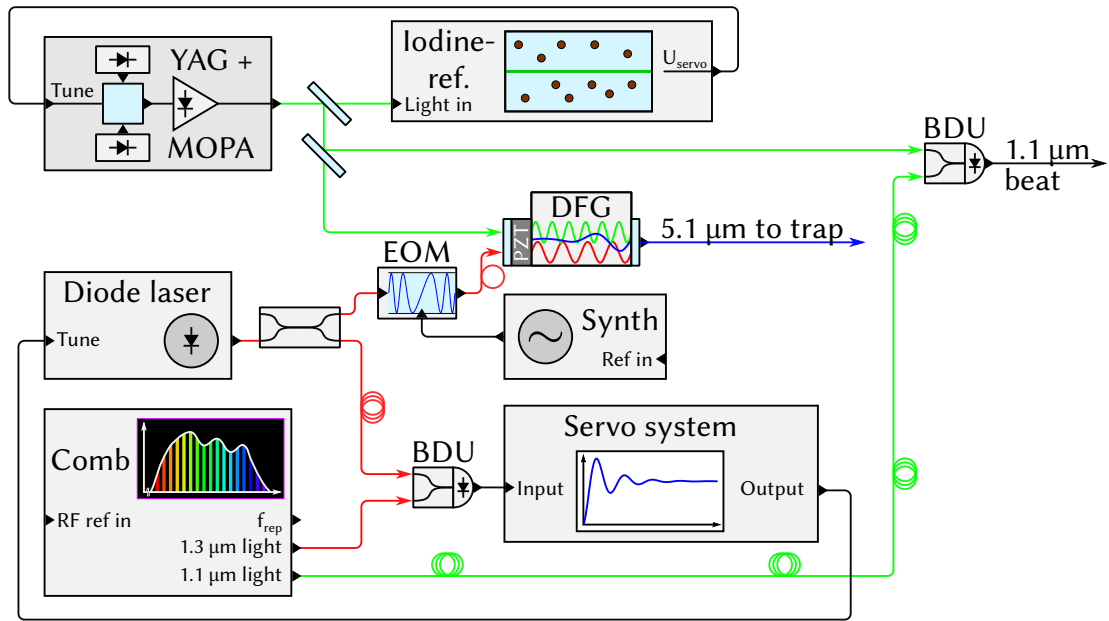
The first radiation source for this transition was built by Ulf Bressel [83] and is shown in figure 3.17. It is based on difference-frequency generation between an Nd:YAG laser at 1064 nm and an ECDL laser diode at 1344 nm. The Nd:YAG laser is frequency stabilized to molecular iodine. Both its frequency and linewidth are measured via the Ti:Sapphire based frequency comb. The laser diode is frequency locked to the frequency comb. The difference frequency generation of the two lasers is performed in MgO:PPLN. In order to improve the conversion efficiency, the 1344 nm radiation is enhanced in a cavity around the crystal, providing a maximum output power of 105  $\mu\text{W}$  at 5.1  $\mu\text{m}$ . The linewidth of the source at 5.1  $\mu\text{m}$  is estimated to be roughly 700 kHz from measurements of the linewidths of the lasers via the frequency comb.

In order to improve the tunability of the source, a sideband generator was added to allow rapid tuning over a range of 460 MHz. This, however, caused the output power to drop to 2.2  $\mu\text{W}$ . Once the diode laser is locked to a suitable comb tooth, further tuning can be performed by changing the frequency of the sideband generator in appropriate steps.

In order to adjust the output power such that power broadening can be minimized, a waveplate mounted on a computer-controllable flip-mount was flipped into the beam, changing the polarization of the Nd:YAG laser's light and therefore the conversion efficiency in the non-linear process.

Control over the source was integrated into the spectroscopy setup's control software by embedding GPIB commands into the scripts which drive the spectroscopy runs. TTL outputs were used to change the output power of the source and to shutter it using a flip mirror. While shuttered using a flip mirror, the light is directed onto a power detector to monitor laser performance during the spectroscopy runs.

Spectroscopic results of this source can be found in section 5.2.1 on page 47



**Figure 3.17:** Simplified setup of the 5.1 μm source and its integration into the spectroscopy setup.

### 3.3.2 New spectroscopy source for 5.1 μm

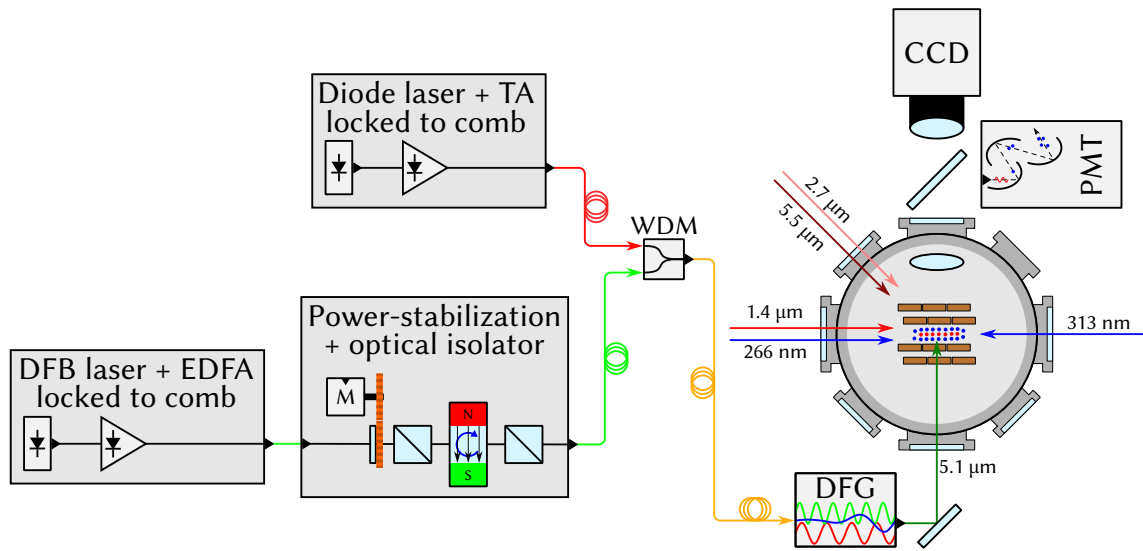
In order to improve on the results obtained via the source explained in the previous section, a more modern version had to be implemented. The main goals for improvement were an easier-to-use source, less maintenance requirements and lower linewidth. The maintenance requirements are mainly due to the usage of the enhancement cavity and its tedious alignment, in which the beams of both lasers have to be overlapped with little feedback during the alignment process until a difference-frequency signal is found.

The working principle of the new source is shown in figure 3.18. Instead of a cavity, a PPLN-based waveguide is used to increase the conversion efficiency. Since the waveguide is fiber-coupled, no alignment of the pumping lasers into the waveguide structure is necessary. The waveguide unit is of small size and can be placed close to the ion trap, thus minimizing the length of the beam path and possible misalignment due to changes in the environment. The waveguide is seeded by two diode lasers, which are combined into a single fiber by means of a wavelength division multiplexer.

The spectroscopy radiation at 5115.5 nm is generated from the difference of 1183.7 nm and 1540 nm.

The pump laser at 1540 nm is a fiber-coupled DFB diode laser, shown in figure 3.19. The setup is very similar to the locking servo of the fiber laser used in conjunction with the QCL (section 3.2): An AOM is used as a fast frequency actuator in order to allow phase-locking of the laser to the frequency comb. The slow actuator is provided by the current modulation input of the laser. Tuning is allowed by adjusting the output frequency of a DDS and mixing the target beat frequency down to a fixed frequency value. This has the advantage that a narrow bandpass filter can be used to filter the input to the PLL. The laser's power is amplified using an EDFA, which also uses the power stabilization setup explained in section 3.12. Figure 3.21 shows the beat between the diode laser and the frequency comb while the phase-lock is engaged. At 1 Hz resolution bandwidth, the carrier strength is more than 60 dB higher than the pedestal.

The pump laser at 1183.7 nm is an ECDL with a tapered amplifier for amplification, as shown in figure 3.20. Its main output is coupled into a fiber, while its secondary output is used to phase-lock it to the frequency comb. Here, the laser diode's current is used as a fast frequency actuator and the piezo-controlled grating angle is used as the slow frequency actuator. The laser can also be

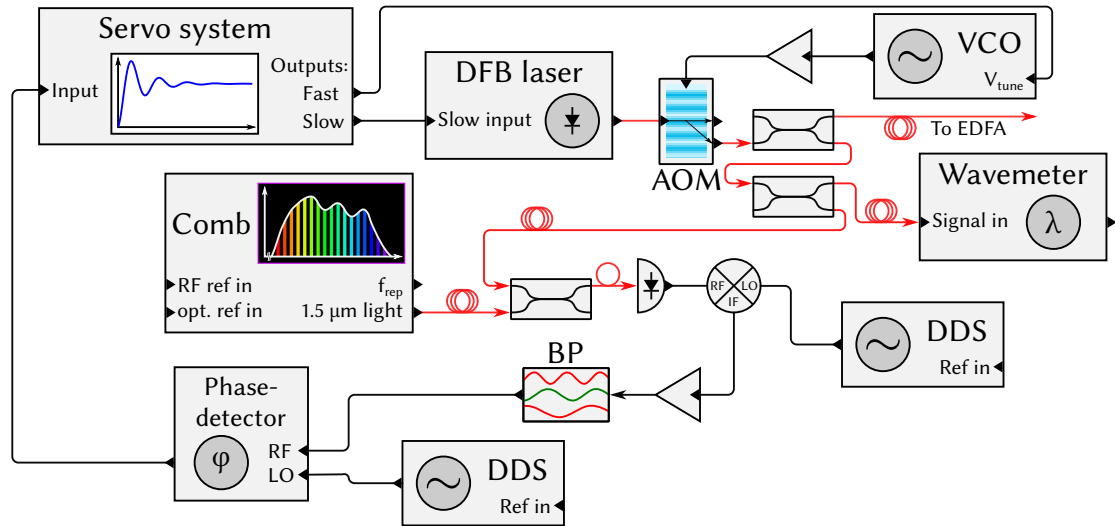


**Figure 3.18:** DFG generation system setup. The power stabilization system is the same as explained in section 3.2.3 on page 26. WDM: wavelength division multiplexer, TA: tapered amplifier.

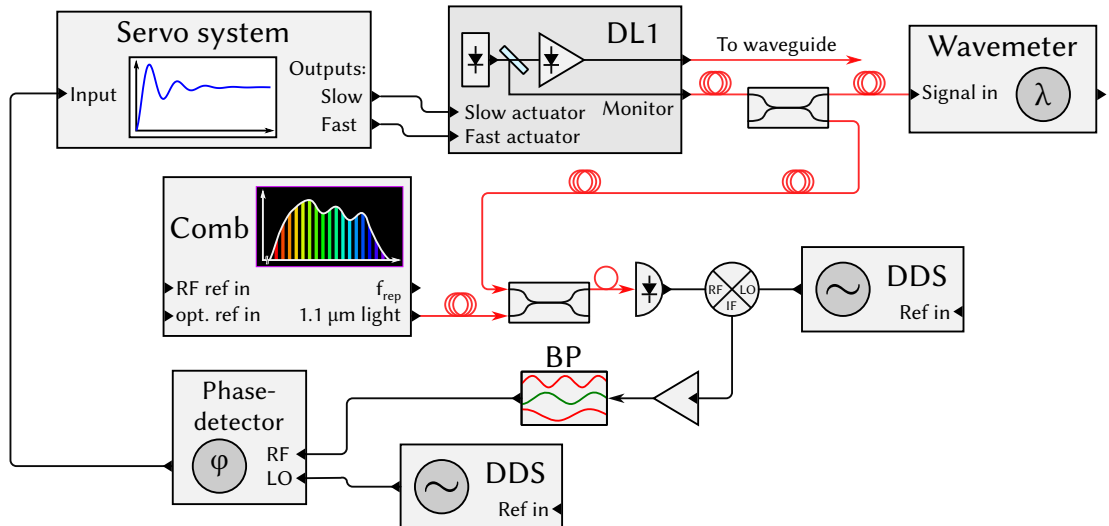
tuned by a mixing process as explained for the first diode laser. The beat between this laser and the frequency comb is shown in figure 3.23. Again, the carrier rises more than 60 dB above the pedestal at a resolution bandwidth of 1 Hz.

Since the approach of using waveguides for difference-frequency generation is universal and requires only a fiber connection between the pump lasers and the waveguide, the system can be extended to other spectroscopy tasks easily by acquiring more waveguides with other phase-matching conditions. The ECDL can be tuned over several 10 s over more than 50 nm and therefore provides a flexible pump source. In order to further enhance the coverage, a second ECDL was phase-locked to the frequency comb using the same setup. Its beats with the the frequency comb under phase-lock are shown in figure 3.22 and are of similar structure as the beats of the first ECDL.

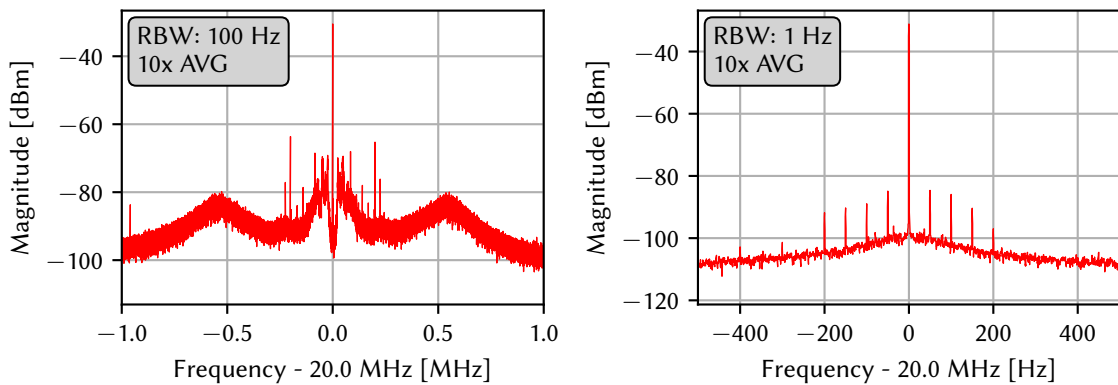
Both pump lasers are phase-locked to the frequency comb, resulting in very narrow beat signals relative to the comb, plus additional noise added by the fiber length between the comb and the lasers. Spectroscopic results are presented in section 5.2.2 on page 48, indicating a linewidth of the difference-frequency radiation of less than 200 Hz.



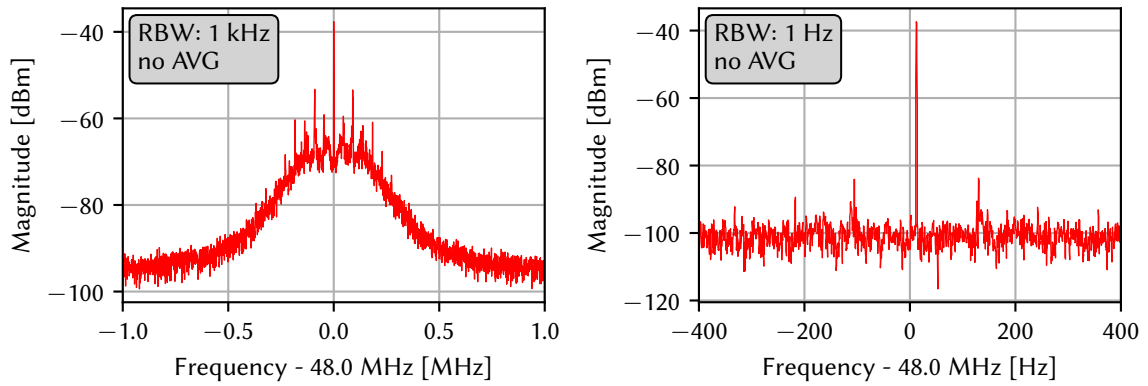
**Figure 3.19:** Outline of the servo system for phase-locking the 1540 nm DFB laser to the frequency comb. BP: band-pass filter.



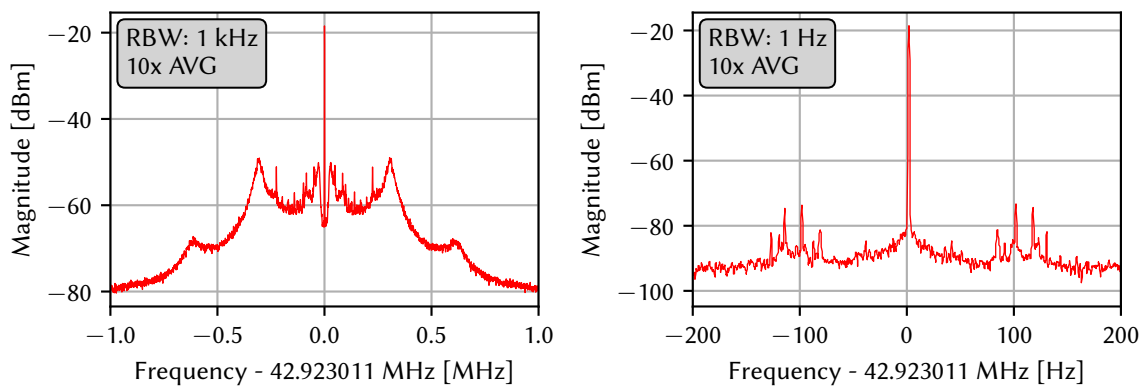
**Figure 3.20:** Outline of the servo system for phase-locking the ECDL diode laser systems to the frequency comb. BP: band-pass filter.



**Figure 3.21:** Beat signals of the DFB laser at 1540 nm used for DFG. Note that the spectra “hide” the fiber noise.



**Figure 3.22:** Beat signals of the first ECDL diode laser used for DFG. Note that the spectra “hide” the fiber noise.



**Figure 3.23:** Beat signals of the second ECDL diode laser which can be used for other DFG applications. Note that the spectra “hide” the fiber noise.

### 3.4 Frequency comb

Ultra-narrow linewidth reference lasers with low drift are a key requirement for today's spectroscopic applications. In case of the spectroscopy lasers used for ro-vibrational spectroscopy in this thesis, an optical frequency comb stabilized to such a reference laser is used to provide a narrow-linewidth frequency reference for the spectroscopy lasers to be stabilized to. Also in case of rotational spectroscopy, the output spectrum of the synthesizer driving the THz-source was verified by mixing it with a harmonic of the repetition rate of the highly stable frequency comb. In these cases, the reference lasers at 1064 nm [84] and 1562 nm [85] were locked to high-finesse cavities based on ULE spacers. As was outlined in the description of the THz linewidth measurement and in the description of the QCL frequency stabilization, the drift of the 1064 nm laser still had to be actively compensated by means of an AOM in order to achieve the desired measurement accuracy.

Another spectroscopic application requiring highly-stable lasers are optical clocks. Here, a low linewidth and low drift clock laser is needed in order to be able to precisely determine the resonance frequency of the clock transition.

The linewidth of the reference lasers is determined by the short-term stability of the reference cavity, namely the optical path length between its mirrors. This stability is limited on one hand by the influence of vibrations in the environment, which cause the distance between the mirrors to change. Thermal noise, on the other hand, is a more fundamental limit.

In the following two sections, the optical frequency comb was used to investigate two possible improvements for mostly the short-term, but to a certain extend also the long-term stability of reference lasers.

#### 3.4.1 Application: Characterization of new cavity materials

Depending on the requirements for optical resonators, their spacers are commonly made of Invar, ULE (Corning, Inc.) or Zerodur (Schott AG). These materials show low coefficients of thermal expansion. ULE and Zerodur show a zero-crossing in their coefficients of thermal expansion near room temperature. One promising candidate for new spacer materials is NEXCERA, a ceramic developed by the Krosaki Harima Corporation (Japan). It also shows a zero-crossing near room temperature and is highly polishable and machinable.

Table 3.1 lists some of its material properties. It has a larger ratio of Young's modulus to density than ULE and Zerodur, which can be an indication of a lower acceleration sensitivity, which is a key requirement for cavities with potentially lower linewidth. Previous characterizations (table 3.2) indicate a good long-term stability. The result of [89] is compatible with zero drift.

In this work, a more detailed analysis of the suitability of this material for optical resonators was performed, focusing primarily on the long-term stability. The investigation was performed by means of the optical resonator technique. To this end, a suitable NEXCERA spacer for an optical cavity was obtained. The shape of the spacer was optimized by Qun-Feng Chen using finite-element modeling in order to reduce its susceptibility to vibrations. High-finesse mirrors were attached to

Material	Young's modulus $E$	Density $\rho$	Ratio $E/\rho$
ULE [86]	67.6 GPa	2.21 g/cm <sup>3</sup>	30.6 GPa · cm <sup>3</sup> /g
Zerodur, expansion class 0 [87]	90.3 GPa	2.53 g/cm <sup>3</sup>	35.7 GPa · cm <sup>3</sup> /g
NEXCERA N118C [88]	140 GPa	2.58 g/cm <sup>3</sup>	54.3 GPa · cm <sup>3</sup> /g

**Table 3.1:** Specifications of various low-expansion materials. A higher ratio  $E/\rho$  can be an indication for low vibration sensitivity.

Material	Linear drift rate $L^{-1}d\Delta L/dt$
ULE	$0.64 \times 10^{-8} \text{ yr}^{-1}$ [92] $0.44 \times 10^{-8} \text{ yr}^{-1}$ [93] $0.15 \times 10^{-8} \text{ yr}^{-1}$ [94, 95]
Zerodur	$9 \times 10^{-8} \text{ yr}^{-1}$ [95]
NEXCERA	$(1.1 \pm 1.1) \times 10^{-8} \text{ yr}^{-1}$ [89] $< 1.2 \times 10^{-7} \text{ yr}^{-1}$ [90] N118C: $(1.74 \pm 0.01) \times 10^{-8} \text{ yr}^{-1}$ [96] N117B: $5.6 \times 10^{-10} \text{ yr}^{-1}$ [91]

**Table 3.2:** Drift rates of low-expansion materials reported in the literature.

the spacer by optical contacting. The cavity was placed in a custom vacuum chamber with active temperature stabilization.

The setup for measuring the resonance frequency of a particular cavity resonance is shown in figure 3 on page 72. In order to measure the resonance frequency of the cavity, light from a stable reference laser at  $1.5 \mu\text{m}$  is sent through an EOM to generate sidebands. The light is then coupled into the cavity. By scanning the frequency of the sidebands, the frequency distance between the reference laser and the next cavity resonance can be determined. The absolute frequency of the cavity resonance can be measured by also measuring the absolute frequency of the  $1.5 \mu\text{m}$  reference laser using the optical frequency comb.

The zero-CTE temperature of the cavity was determined by observing the frequency of a particular cavity resonance while changing the temperature of the cavity over several days, as shown in figure 6 on page 73. The zero-CTE temperature was determined to be

$$T_0 = 22.9 \pm 0.2^\circ\text{C}. \quad (15)$$

The long-term drift of the cavity was determined by operating the cavity at its zero-CTE temperature and measuring the drift of the resonance over 67 days. The linear drift rate was determined to be:

$$L^{-1}d\Delta L/dt = (1.74 \pm 0.01) \times 10^{-8} \text{ yr}^{-1} \quad (16)$$

Table 3.2 allows a comparison of the result with results for other materials and results obtained by other researchers. The obtained drift-rate is larger than for ULE and Zerodur. Unlike [89], it is not compatible with zero, but smaller than [90]. The drift rate obtained by [91] is two orders of magnitude smaller, but for a different variant of NEXCERA. Given these results, NEXCERA is indeed a promising material for highly-stable cavities. Further work will be needed to fully access and quantify the possibility of NEXCERA cavities with less vibration sensitivity.

### 3.4.2 Application: Spectroscopy of Europium

The short-term frequency stability of lasers stabilized to optical resonators is in practice limited by vibrations, with a fundamental limit given by thermal noise. Spectroscopy of persistent spectral holes in rare-earth-doped crystals, while held at cryogenic temperatures, is investigated as an alternative to overcome both limitations. Even though the holes are called “persistent”, their properties change under the influence of a laser field which probes them. Therefore, care must be taken to minimize the effects of the spectroscopy lasers. To this end, a sufficiently large amount of spectral



holes spread over a broad frequency range is usually created and subsequently only subgroups of the holes are probed by the lasers.

Spectral holes can provide enough contrast in order to allow a laser to be locked to them by means of the Pound-Drever-Hall method and thus serve as an alternative to optical resonators.

The setup for the spectroscopy of spectral holes is shown in figure 1 on page 78. The frequency comb is stabilized to a reference laser at 1064 nm (not shown). Spectroscopy is performed using a frequency-doubled 1160 nm laser. The fundamental frequency of the laser is measured using the frequency comb. Its second harmonic is used to stabilize it to a high-finesse optical resonator and also to perform the spectroscopy.

The relationship between the burn-time and the linewidth of the obtained spectral holes is investigated (figure 2 on page 79), allowing reliable production of spectral holes with a mean FWHM linewidth of 0.61(7) kHz while keeping a sufficiently good signal contrast (figure 3 on page 79).

The long-term frequency drift and broadening of spectral holes was measured near 1.2 K. In order to be able to measure the long-term properties of spectral holes, a series of holes was burned and during subsequent measurements, only previously untouched spectral holes were investigated. The linewidth increase after 49 days was found to be 35% (figure 7 on page 81), compatible with results reported in the literature previously [97]. An upper limit of  $2.3 \times 10^{-19}$  /s for the drift of spectral holes could be set (figure 10 on page 82), which is on par with results obtained for cryogenic cavities [98].

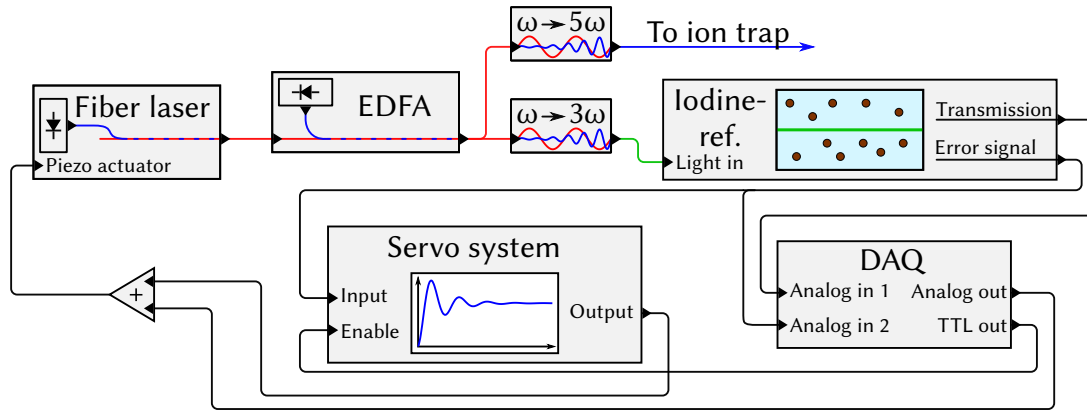
These results indicate that using spectral holes as a frequency reference for a highly-stable laser with low linewidth is feasible. Work is currently underway to overcome the effects of linewidth broadening and contrast loss while stabilizing lasers to spectral holes.

## 4 Supporting laser systems

The spectroscopic goals of this thesis require the use of some supporting laser systems, which are needed to prepare the ions in the desired states. Work done on three of these supporting laser systems is described in this section.

### 4.1 UV1: Automated frequency tuning

The Beryllium cooling laser for trap 1 [99] is frequency stabilized to molecular Iodine at the third harmonic of the seed laser, as shown in figure 4.1. When the cooling laser is close to the Beryllium cooling transition at its fifth harmonic UV output (313 nm), the third harmonic at 522 nm can interrogate the P58(2-49) absorption line in molecular Iodine, which has 14 hyperfine components. The hyperfine structure can be resolved by frequency modulation transfer spectroscopy. By appropriate frequency modulation, an error signal can be generated at each hyperfine component, allowing the laser to be frequency stabilized to it. Coarse control over the detuning of the cooling laser relative to the  $\text{Be}^+$  cooling transition can be set by locking to one of the hyperfine components. Fine tuning is accomplished using two AOMs. During experiments with ion crystals, the detuning has to be changed in order to provide optimum Doppler cooling depending on the temperature of the ion crystal. Loading of the crystal happens at a large detuning (roughly 1.1 GHz) corresponding to locking the laser to the “first” Iodine line. Here, the lines are counted starting at the line with the largest red-detuning from the  $\text{Be}^+$  transition frequency at the fifth harmonic of the seed laser. After cleaning the crystal, it can be further cooled down by slowly tuning the laser closer to the transition. The tuning speed must not be faster than the crystal is transitioning to cooler temperatures, including phase transitions. Otherwise, the coldest temperatures can not be reached. The coldest temperatures are reached close to line 12, which is also where spectroscopy on  $\text{HD}^+$  is performed.



**Figure 4.1:** Setup for automating the frequency tuning of the UV1 source.

The detuning has to be changed back to line 1 after a few spectroscopic runs, when the crystal has to be cleaned from remaining  $\text{HD}^+$  and possible contaminants.


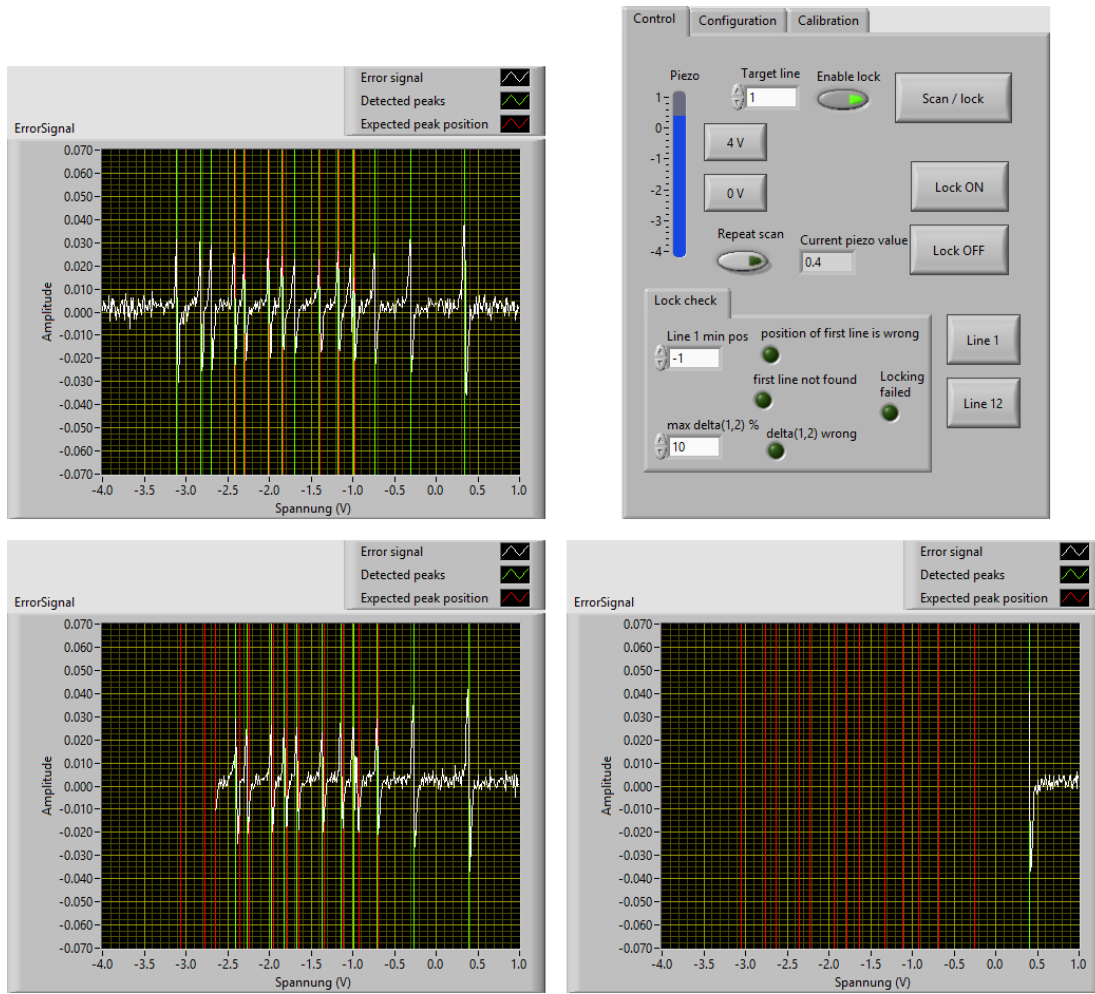
In order to reduce manual operator intervention at each cleaning, automation of the change of detuning was implemented in the scope of the Bachelor thesis of Jana Scheuer [100], which Soroosh Alighanbari  and I supervised. Figure 4.1 shows how the automation system interacts with the servo system of the UV laser. Both the DC transmission signal of the gas cell and the derived error signal are recorded by the data acquisition card. An analog output is used to add an offset to the Piezo driver on top of the output of the servo system. A digital output is used to interrupt the servo loop.


Figure 4.2 shows the relevant parts of the user interface of the control program. To start the automation system, the user has to manually lock the laser to the first Iodine line using the servo system's controls. Then, the program can perform a scan over the entire hyperfine structure in order to calibrate a look-up table for the Piezo offset voltage for each line, relative to the position of the first line. Lines are detected during the calibration by setting a threshold for the excursions of the error signal. The top left picture in figure 4.2 shows a scan over the hyperfine structure after calibration. Recognized hyperfine lines are highlighted using green vertical lines. The expected positions are marked by red vertical lines, which can not be seen in this plot since the expected line positions and the recorded line positions match very well. Only in some cases, some lines appear yellow because the red and green lines are very close together.

For tuning to individual lines, purely counting the detected lines while moving through the spectrum to the target frequency was not found to work reliably enough. One reason is the change in height of the error signals peaks over time, until the signal-to-noise ratio is too low for reliable counting, even though locking of the system still works. Another problem is the slow scanning speed when moving through the spectrum, which can cause the system to miss lines when the laser is drifting during the scan. The scanning speed is limited by the speed at which the ion crystal can follow the detuning of the cooling laser with its temperature, as mentioned earlier. Therefore, a scheme combining the look-up table created during calibration together with some consistency checks on the relative positions of the first lines was implemented.

After successful calibration, the UI in the top left part of figure 4.2 can be used to jump to individual lines. The first line is expected near 0 V of offset output. Therefore, in order to go to a specific line, the system moves the laser frequency further beyond line 1 by increasing the offset voltage slowly up to 1 V and subsequently starts scanning through the lines by decreasing the offset voltage. If a lock to line 1 is desired, line 1 is only detected using a threshold value. If a lock to a higher line number is requested, an additional consistency check is performed: The distance



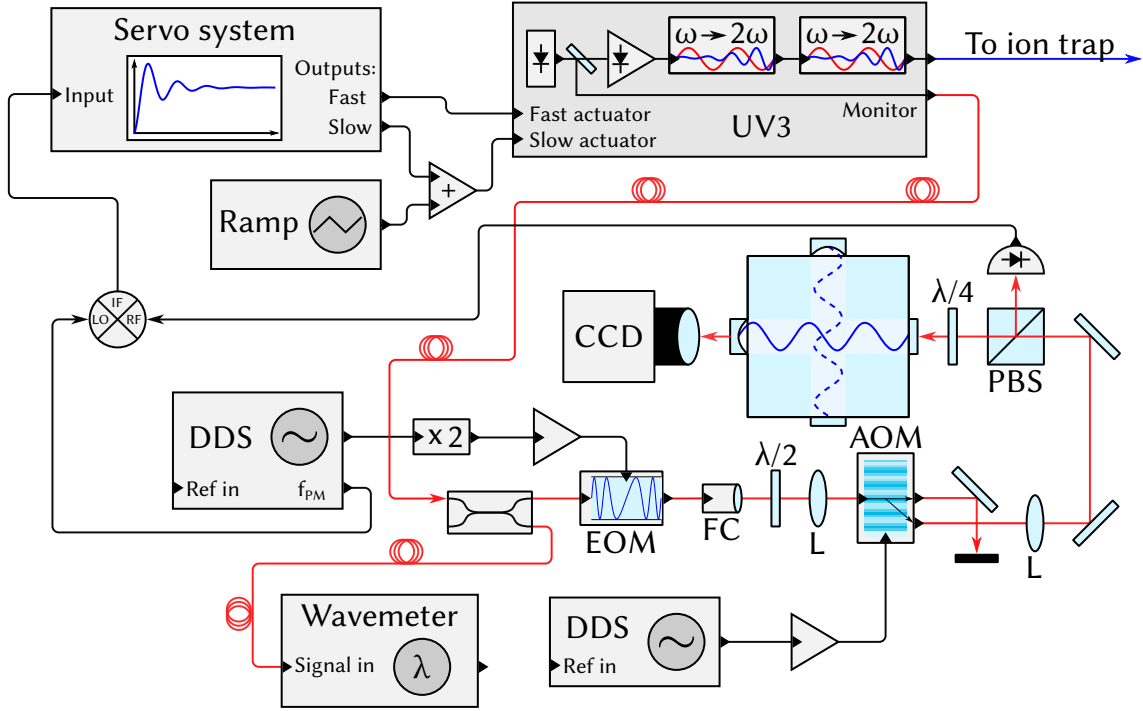
**Figure 4.2:** User interface of the cooling laser frequency control program. Top left: Scan over all hyperfine components immediately after calibration. Top right: Control UI showing the current output voltage, control buttons, and error detection indicators. Bottom left: Laser locked to line 12. Bottom right: laser locked to line 1.

between lines 1 and 2 is checked against the look-up table. If that distance does not match within a certain range, the locking attempt is cancelled and the laser is moved back to the left of line 1. This check was implemented to detect strong long-term drifts of the laser, where line 1 would drift beyond 1 V offset voltage and the scan would therefore erroneously start at line 2. The most important aspect of the locking is not to accidentally lock beyond line 12, because then the cooling laser will be blue-detuned with respect to the cooling transition, leading to ion loss. If a scan fails, the violated criteria are indicated in the UI, allowing the user to take manual action in case the system can not find the locking conditions after a few attempts. The photos on the bottom of figure 4.2 show line detection results while moving the laser to line 1 (right photo) and line 12 (left photo). During normal day-to-day operation, according to Soroosh Alighanbari's  experiences, locking works on the first try most of the time during the course of one spectroscopy session.

## 4.2 UV3: Stabilization of a cooling laser to a ULE cavity

A new tightly confining ion trap for single ions is currently under development in the institute [101]. Like the trap used for spectroscopy in this thesis, it is a Paul trap. However, it was designed to contain only a single Beryllium ion, which sympathetically cools a single  $\text{HD}^+$  or  $\text{H}_2^+$  ion. Its tight

confinement is designed such that ions will be in the Lamb-Dicke regime even at a wavelength of  $\sim 1 \mu\text{m}$ , as described in section 1.2. This will allow Doppler-free spectroscopy of overtone transitions in  $\text{HD}^+$  at a wavelength of  $\sim 1.1 \mu\text{m}$ , allowing for a fractional resolution of  $10^{-13}$ .



**Figure 4.3:** Setup of the locking system of UV3. PBS: polarizing beam splitter, L: lens, FC: fiber collimator, x2: RF frequency doubler.

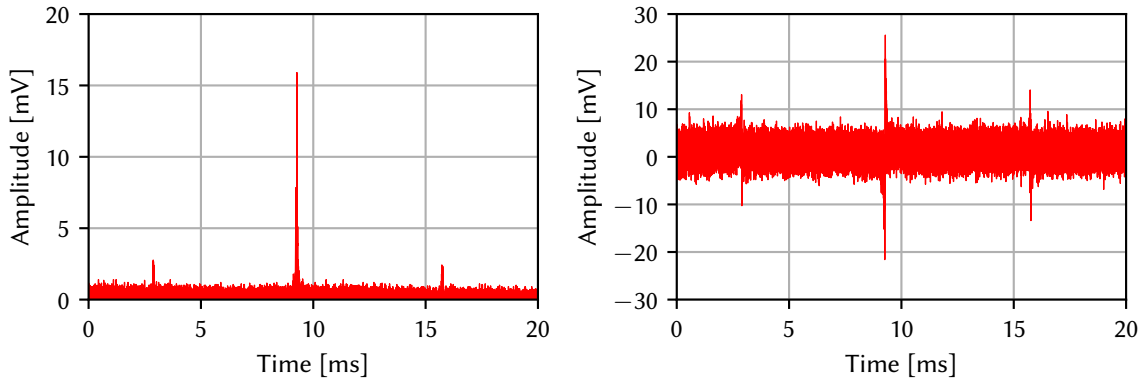
The trap has been designed to allow Raman-sideband cooling [69, 70] of the Beryllium ions. With this technique, the Beryllium ion can be cooled into the motional ground state of the trap. Via sympathetic cooling, the  $\text{HD}^+$  ion is also cooled to the motional ground state. When both ions are in their motional ground state, a non-destructive quantum logic spectroscopy method can be employed for performing spectroscopy.

In order for the Raman-sideband cooling of Beryllium to work, the linewidth of the cooling laser has to be significantly smaller than the secular frequency of the cooled ion in the trap. For this trap, the secular frequency is estimated to be 2.6 MHz [101, Table 4.1 page 55,  $\omega_{\text{sec}}, z$ ].

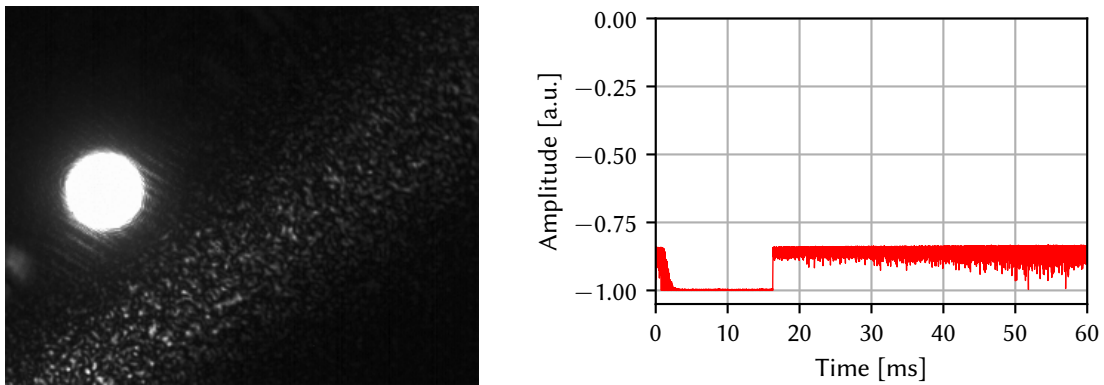
The cooling laser is a commercial system (Toptica) based on the resonant quadrupling of 1252 nm to 313 nm. For this laser, no molecular/atomic reference has been set up so far. It is only frequency-stabilized to a wavemeter via the pump-laser at 1252 nm. Since the calibration of the wavemeter is only performed periodically when the cooling laser of trap 1 is at a specific frequency, the residual drift of the laser wavelength over time is unknown.

The frequency drift of the laser causes the ions' fluorescence to change over time. Since the trap is still under development, changes in the ions' fluorescence due to drift of the laser frequency can not be distinguished from effects due to changes in the trap settings, which still need to be optimized.

The ULE cavity used for the stabilization of the QCL was therefore repurposed as a frequency reference for the UV cooling laser. The optical and electrical setup is shown in figure 4.3. The frequency of the cooling laser has to be in the vicinity of the Beryllium ion cooling transition and needs to be changed during the cooling process, in order to find the optimum detuning. This can not be accomplished by tuning the cavity's resonance frequencies, since it is a ULE cavity with a

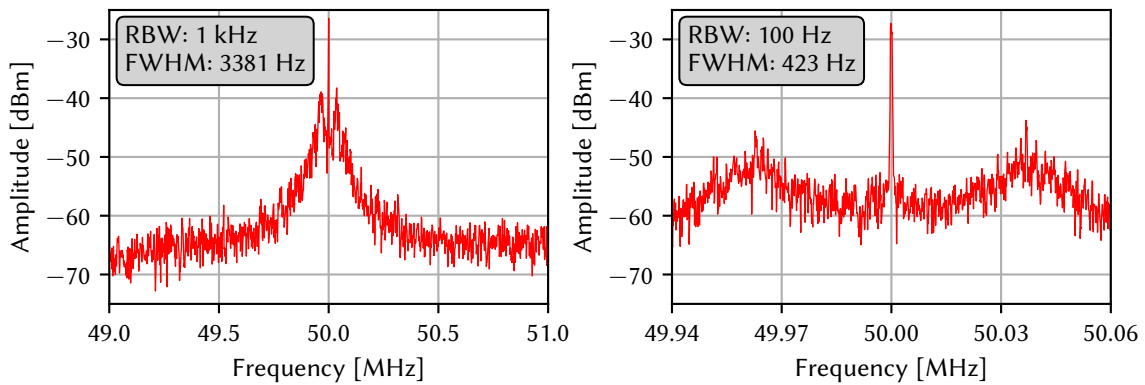


**Figure 4.4:** Generation of error signal. Left: Sideband with sidebands-of-sideband. Right: Corresponding error signal.

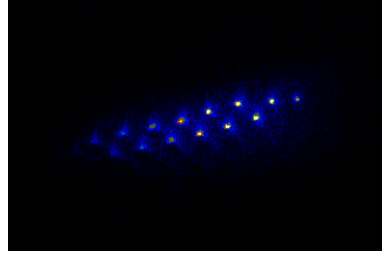



**Figure 4.5:** Left: TEM00-mode of locking the sideband of UV3 to the resonator. The spurious reflections (diagonal bottom left to top right) are only visible if locked to a first-order sideband and are therefore helpful during locking. Resolving the sideband order via the wavemeter is not always reliable due to its drift.

Right: A simple lower limit estimation of the incoupling efficiency of lock to sideband, namely 16.8 %. The plot shows the DC reflection signal, containing the sum of power of carrier and sidebands at all orders. However, the maximum possible incoupling for the sideband is given by the power in that sideband, which can not be seen here.



**Figure 4.6:** Beat of UV3 with frequency comb. Left: 1 kHz RBW, right: 100 Hz, 423 Hz FWHM. The linewidth does not decrease when increasing the resolution.



**Figure 4.7:** 14 Beryllium ions cooled via UV3 after optimization of trap parameters. Lifetime: 27 minutes, image courtesy Christian Wellers .

very small temperature dependence. Therefore, frequency stabilization of the laser to the cavity is implemented using the sideband-of-sideband technique [102].

This scheme is based on the Pound-Drever-Hall technique [103], but the laser is not locked to a cavity mode directly. Instead, an EOM is used to generate a strong sideband on the laser frequency in the range of 30 to 800 MHz. The radio frequency used to generate the sideband is then phase-modulated at 11 MHz in order to generate a set of sidebands. These sidebands are then also imposed on the optical sidebands generated by the EOM and can be used to generate a PDH-error signal when the sideband comes into resonance with a cavity mode. A servo is then used to lock the laser to the cavity. By changing the frequency of the sideband, the laser can be tuned without changing to another cavity mode manually and without changing the temperature of the cavity spacer.

Since the employed direct-digital-synthesizer (DDS, type: AD9910, Analog Devices) only works up to a frequency of 400 MHz, it is frequency-doubled using an RF doubler (ZX90-2-13-S+, MiniCircuits) in order to extend its working range. The obtained spectrum is sufficiently pure, such that the EOM can be driven without any additional bandpass filters. It is important to note that the sideband-of-sideband's frequency is not changed during frequency doubling.

The operating parameters of the system are determined by finding the two cavity modes which are closest to the target frequency of the cooling laser. The difference frequency to these modes at the pump laser wavelength is then determined and one of the two is picked as the target mode. For tuning of the laser, the steps in the UV and on the DDS are related by:

$$\Delta f_{313\text{ nm}} = 4 \cdot 2 \cdot \Delta f_{\text{DDS}} \quad (17)$$

The factor 4 is due to the quadrupling of the pump laser and the factor 2 is due to the doubling of the DDS. The obtained error-signal is shown in figure 4.4. In order to discern higher order cavity modes from true  $\text{TEM}_{00}$  modes, the transmission of the cavity is observed using a camera, as shown in figure 4.5. This is needed since higher order modes are still present close to the  $\text{TEM}_{00}$  mode and the different modes can not always be clearly distinguished using the wavemeter alone.

The linewidth of the cooling laser is determined by observation of a beat with the optically referenced frequency comb, which is shown in 4.6. The pump laser has a linewidth of 400 Hz FWHM, which is assumed to be widened to 1.2 kHz during the quadrupling. This linewidth is sufficiently small in order to satisfy the condition for Raman-sideband cooling.

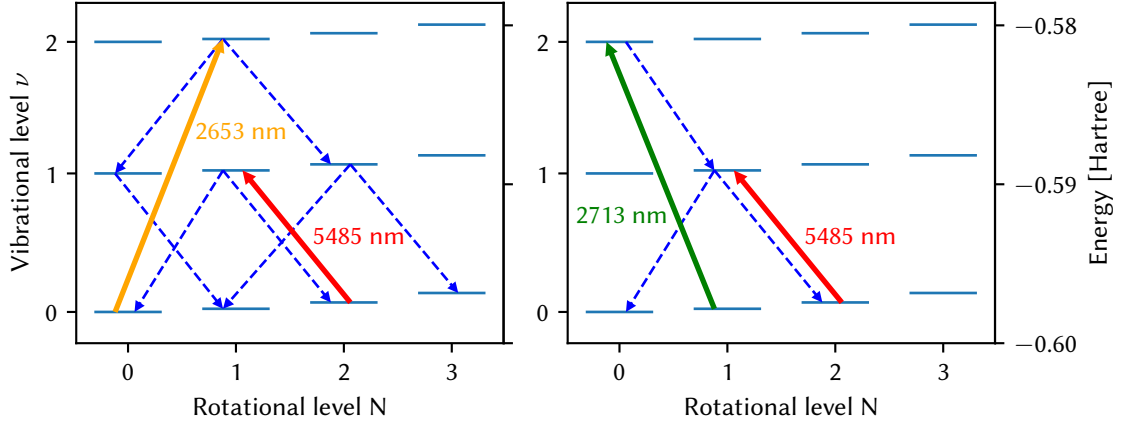
The system is stable enough for later use during spectroscopy: It routinely remains in lock for more than 8 hours during normal lab usage while the DDS was tuned in 100 kHz steps in a 1 MHz range. This stability allowed an optimization of the trap parameters, such that a stable ion crystal as shown in figure 4.7 can be produced and stored for 27 minutes.



### 4.3 DFB: Improved frequency agility for optical state preparation lasers

In order to achieve a good signal-to-noise ratio during spectroscopy, the ions have to be prepared such that the lower spectroscopic level is well populated, while the upper spectroscopic level, from which the number of excited ions is determined, should be rather empty. Most spectroscopic schemes in this thesis start in the  $(v = 0, N = 0)$  state. This state is populated via optical pumping using a quantum-cascade laser at  $5.5 \mu\text{m}$  [72] and a distributed-feedback laser at  $2.713 \mu\text{m}$ .

The optical pumping scheme shown in figure 4.8. The plot on the right side shows the state transfer to the  $(v = 0, N = 0)$  state, while state preparation for the  $(v = 0, N = 1)$  state is shown on the left side.



**Figure 4.8:** Optical pumping strategies for DFB lasers. Solid lines: Transitions used for optical pumping: Orange: DFB0 at  $2.653 \mu\text{m}$ , green: DFB1 at  $2.713 \mu\text{m}$ , red: QCL at  $5.485 \mu\text{m}$ . Dashed blue lines: spontaneous emission. Left: DFB0, used to populate the  $(v = 0, N = 1)$  state, right: DFB1, used to populate the  $(v = 0, N = 0)$  state. The QCL is used for emptying the  $(v = 0, N = 2)$  state in both scenarios.

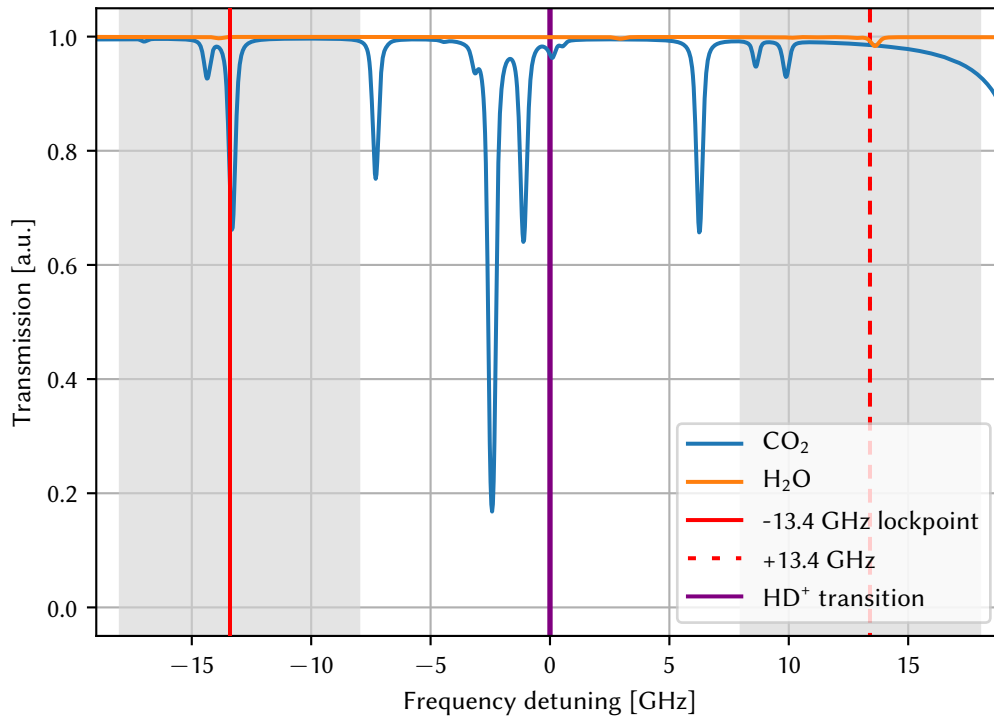
The  $2.713 \mu\text{m}$  DFB laser (called DFB1 from now on) was stabilized to a gas absorption line in  $\text{CO}_2$ , whose spectrum relative to the spinless frequency of the relevant  $\text{HD}^+$  transition is shown in figure 4.9. The position of the gas absorption line is not at the center of the respective  $\text{HD}^+$  transition. This necessitated a lock not to the transition center, but instead a slight detuning had to be introduced by changing the offset voltage of the lockbox input. Since the gas absorption line was quite weak, the offset was very sensitive to changes in the environment and had to be checked several times during a spectroscopy session.

For preparation of spectroscopy of transitions starting from a lower level of  $(v = 0, N = 1)$  (pumping scheme in the left plot of figure 4.8), a new pumping laser at  $2.653 \mu\text{m}$  (called DFB0 from now on) needed to be added to the setup. For this laser, no suitable gas transition could be found in the vicinity of the respective optical pumping transition.

In order to overcome the difficulties faced for both lasers, a system based on locking to a sideband using an EOM was implemented as part of the Master's thesis of Soroosh Alighanbari [104] (note that the numbering of the DFB lasers used in the thesis is different from the numbering used in later publications and here). The setup is shown in figure 4.10. It is conceptionally similar to the locking scheme used in section 4.2, but not as flexible due to technical difficulties. New housings for each DFB laser were set up, as shown in figure 4.11. The DFB lasers are overlapped using a 50:50 beam splitter. One output of the beam splitter is sent through a pseudo-isolator consisting of a  $\text{L}/4$  plate and a wire grid polarizer. The light is then coupled into an optical fiber for delivery to the ion trap.

This improves the stability of the system, because the free-space path from the laser to the trap is shorter. For the DFB0 laser, fiber delivery is also important because the relevant  $\text{HD}^+$  transition is very close to a very strong water absorption line. In order to reduce the water absorption in the free-space parts of the DFB setup, it was purged with Nitrogen.

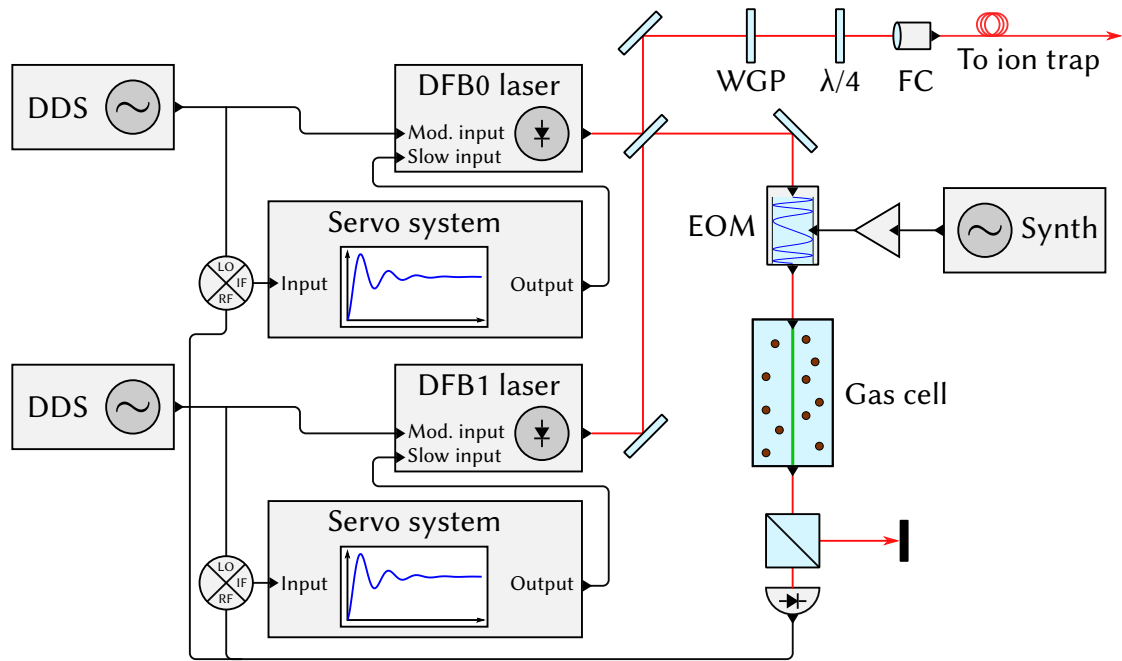
The other output of the beam splitter is used for frequency stabilization. A microwave-EOM (active material CdTe, design described in [105]) generates a sideband, which is then guided through the gas cell. Unfortunately, the synthesizers available for this project do not feature phase-modulation capabilities. Therefore, the frequency modulation needed to derive an error signal has to be created by modulating the laser current directly, in contrast to the sideband-locking technique used in other setups [102]. This has the disadvantage that the carrier also produces an error signal. This is a problem when locking DFB0, since the water absorption near the  $\text{HD}^+$  transition also creates an error signal which shifts the lock point.



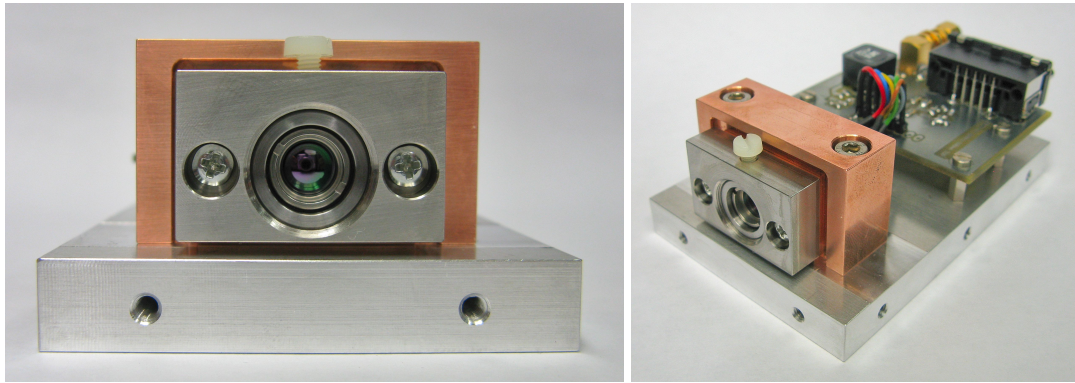
**Figure 4.9:** Simulation of the relevant gas absorption lines for the frequency stabilization of DFB1, relative to the  $(0, 1) \rightarrow (2, 0)$  transition in  $\text{HD}^+$  at 2712.9717 nm [75]. Length of the gas cell: 100 cm, pressure: 25 mBar, room temperature. The working range of the EOM is indicated by the gray regions. DFB1 is locked to the  $\text{CO}_2$  transition indicated by the red line at  $-13.4$  GHz. At  $+13.4$  GHz (dashed red line), there is no  $\text{CO}_2$  transition which would interfere with the locking. The transition at 0 detuning is sufficiently weak such that it does not disturb the locking. Gas absorption data obtained from SpectralCalc [106]. DFB0 is locked to  $\text{N}_2\text{O}$  in a similar way, however a strong water absorption line near the carrier causes the lockpoint to shift due to introduction of an additional offset.

In case of DFB1, a suitable gas absorption line in  $\text{CO}_2$  is at  $-13.4$  GHz from the  $\text{HD}^+$  transition, as shown in figure 4.9. Luckily, the previously used absorption line close 0 Hz detuning is weak enough in order not to interfere with the locking to the absorption line interrogated by the sideband.





**Figure 4.10:** Setup of the DFB laser locking system. WGP: wire-grid polarizer, FC: fiber collimator.



**Figure 4.11:** The distributed feedback laser at  $2.653\ \mu\text{m}$  in its housing. The design is based on a design of Alexander Nevsky. Left: Front view of the collimation lens. The distance between the lens and the laser diode can be adjusted by turning the lens, which is attached to a holder with an outer thread with  $0.5\ \text{mm}$  pitch. Horizontal alignment of the lens is performed by slightly loosening the Philips head screws and pushing the lens holder block with a screwdriver inserted into the notch behind the holder. Right: The laser diode is fixed in the copper block, which acts as a heatsink for the temperature stabilization element in the laser diode housing. A second stage temperature stabilization, acting on the copper block, was added later. To this end, a Peltier element was placed between the copper block and the aluminium baseplate. The circuit board in the back provides a D-sub connector for temperature and current control as well as an SMA-connector for direct current control of the laser diode.

Since the frequency of the DFB lasers can now be tuned by changing the frequency of the sideband generated by the EOM, hyperfine-resolved optical state preparation is now in principle possible. At the moment, the tuning functionality is only used to scan the laser over the hyperfine transitions which pump from the most populated hyperfine states.

## 5 Results

### 5.1 Rotational spectroscopy

The results summarized in this section are from the publications presented in sections 6.2 and 6.6.

Even on molecular ions cooled to the 10 to 15 mK regime, Doppler broadening still limits the achievable resolution as indicated by equation 9. One way to suppress any Doppler broadening is confinement of the ions to a range smaller than the spectroscopy wavelength. The molecular ions will then be in the Lamb-Dicke regime, as described in section 1.2. For the trap used throughout this thesis, the exact wavelength where the Lamb-Dicke regime begins was initially not known. Therefore, a transition with a large transition wavelength was chosen to have the highest chances of exploiting this regime. The largest transition wavelengths for transitions starting in the ground state are for pure rotational transitions. Therefore, the  $(v = 0, N = 0) \rightarrow (0, 1)$  fundamental rotational transition at roughly 1.3 THz was chosen as a first candidate.

A first demonstration of this THz transition was shown in the work [107]. The molecular ions were first prepared in the  $(v = 0, N = 0)$  groundstate via optical state preparation [72]. Even so, the achievable signal-to-noise ratio was not very high due to the distribution of the population across the hyperfine states, with an added Zeeman splitting on top of it. The knowledge of the magnetic field inside the trap was very limited. In order to produce a reasonable spectrum, spectroscopy was performed in such a way that the population of several hyperfine states could be probed together. This was achieved by stepping the THz-source through a list of 4 different hyperfine transitions for each datapoint, as shown in table 1 on page 55. In order to obtain a spectrum of the combined transitions, the frequency lists were detuned from the expected line centers by the same amounts. The observed spectrum (figure 6 on page 57) is more than 2 MHz broad, which is significantly wider than expected from Doppler broadening alone (which would be 70 kHz). The spectral broadening can be due to either the magnetic field, in the form of Zeeman splitting, or due to power broadening.

Work on THz spectroscopy was advanced in publication [77]. Here, the THz radiation was not any more irradiated in the axial direction, but in the transverse direction. The spatial confinement of the ions in the transverse direction is much smaller than in the axial direction, thus allowing for spectroscopy in the Lamb-Dicke regime. Using the method described in [108], the magnetic field in the trap could be reduced to almost 0.040 (6) mT. This allowed the individual Zeeman components of each hyperfine state to be overlapped, thus increasing the addressed population and therefore the signal-to-noise ratio. By systematic reduction of the THz power (to reduce power broadening), a spectrum with a linewidth of 1.3 kHz was obtained. The obtained value for the line center is in agreement with the expected theory value for zero magnetic field:

$$f_{rot,theory} = 1,314,935.8273 (10)_{theo} \text{ MHz} \quad (18)$$

$$f_{rot,exp} = 1,314,935.8280 (4)_{stat} (3)_{syst} \text{ MHz} \quad (19)$$

In order to be able to extract the value of the proton mass  $m_p$  from the measurement results, the theoretical transition frequency is calculated using the values of CODATA2014 [1] for the needed constants and treating  $m_p$  as an independent parameter. Using this method, the following value for  $m_p$  can be derived:

$$m_p = 1.0072764669 (13) \text{ u} \quad (20)$$

This result has a larger relative uncertainty ( $1.3 \times 10^{-9}$ ) than the value of  $m_p$  reported in CO-DATA2014 ( $9 \times 10^{-11}$ ), but it is consistent with it and therefore provides an independent verification.

## 5.2 Ro-vibrational spectroscopy

In this section, results of single-photon spectroscopy on the  $(v = 0, N = 0) \rightarrow (1, 1)$  transition in  $\text{HD}^+$  are presented. Due to its long wavelength of  $5.1 \mu\text{m}$ , the Doppler broadening at typical ion temperatures of 10 mK is only 3.4 MHz (see equation 9). Therefore, individual hyperfine lines can be resolved using single-photon spectroscopy.

### 5.2.1 Doppler-limited ro-vibrational spectroscopy

The results summarized in this section are from the publication presented in section 6.3.

First spectroscopic results were obtained using the  $5.1 \mu\text{m}$  source described in section 3.3.1 on page 30. The energy diagram and the labeling of the transitions are shown in figure 2 on page 62. The obtained spectra for some of the transitions are shown in figure 3 on page 63. At a magnetic field of 0.8 G, the Zeeman sublevels are not resolved. In order to be able to also measure weak transitions with initially low population in their respective ground states, hyperfine-state optical pumping was employed, possible thanks to the good frequency resolution and control of the spectroscopic source. To this end, the spectroscopy source was tuned to drive the transitions W1 and W3, in order to increase the population in the ground state of transition W4. The results of hyperfine-state optical pumping are shown in figure 4 on page 63. The signal-to-noise ratio is increased by more than a factor of 2, which allowed to obtain a spectrum of the W4 transition suitable for further analysis.

The hyperfine structure of the ground state is fully described by the two constants  $E_4(0, 0)$  and  $E_5(0, 0)$ , which can be determined from suitable combinations of the obtained transition frequencies and subsequently be compared to the theoretical values of these constants [4, 73]:

$$(E_4(0, 0), E_5(0, 0))_{exp} = (906 (17), 142.33 (25)) \text{ MHz} \quad (21)$$

$$(E_4(0, 0), E_5(0, 0))_{theoretical} = (925.38 (1), 142.29 (1)) \text{ MHz} \quad (22)$$

An alternative comparison between theory and experiment is possible by comparing the spin-independent frequency, which can be determined from the individual transition frequencies:

$$f_{0,exp} = 586\,050\,52.00 (.064) \text{ MHz} \quad (23)$$

$$f_{0,th} = 586\,050\,52.139 (11) (21) \text{ MHz} \quad (24)$$

The difference between the theoretical and experimental values is twice the combined theoretical and experimental error.

Besides the improved spectroscopic resolution, the presented results are also of importance, because they are the first measurement, at the  $10^{-9}$ -level, with a resolution high enough to be sensitive to QED contributions of order  $\alpha^5$ . They were also the first demonstration of driving weakly allowed

hyperfine transitions in the optical domain and showed the lowest transition linewidth, to the best of my knowledge.

The discrepancy between theory and experiment was later used by Salumbides et al. [56, page 5, chapter (C)] to obtain an upper limit on a fifth force in hadronic interactions (as described in section 1.1.3.1 on page 13):

$$\beta/\alpha < 1.1 \times 10^{-9} \text{ for } \lambda > 1 \text{ \AA} \quad (25)$$

Here,  $\beta$  is an expression for the strength of the force relative to the electromagnetic force, whose strength is given by  $\alpha$ , for an interaction range  $\lambda$ .

### 5.2.2 Ro-vibrational spectroscopy in the Lamb-Dicke regime

The results summarized in this section are from the publication presented in section 6.9.

Improved spectroscopic results were obtained by using the source described in section 3.3.2 on page 31 in such a way that the ions are in the Lamb-Dicke regime. The Lamb-Dicke regime was reached by irradiating the light onto the ions orthogonal to the trap axes, as in figure 3.18 on page 32.

A linewidth of 0.2 kHz ( $3 \times 10^{-12}$  fractionally) was reached on the  $(v = 0, N = 0) \rightarrow (1, 1)$  transition, allowing individual Zeeman components to be resolved. Due to the low linewidth, an absolute fractional uncertainty of  $3.3 \times 10^{-12}$  was reached. The two measurements share the same hyperfine state in the lower level. The two transition frequencies obtained are [109, eq. 1]:

$$f_{12}^{(exp)} = 58,605,013,478,03 (19)_{exp} \text{ kHz} \quad (26)$$

$$f_{16}^{(exp)} = 58,605,054,772,08 (26)_{exp} \text{ kHz} \quad (27)$$

From these two measurements, the spin-averaged frequency value is obtained. It agrees to the  $2.9 \times 10^{-11}$  level with the theoretical value. Note that the experimental value is slightly more precise than the value from theory [109, eq. 4]:

$$f_{spin-avg}^{(exp)} = 58,605,052,164.24 (16)_{exp} (85)_{theor,spin} \text{ kHz} \quad (28)$$

$$f_{spin-avg}^{(theor)} = 58,605,052,163.0 (5)_{theor,QED} (13)_{CODATA2018} \text{ kHz} \quad (29)$$

For the determination of the proton-to-electron mass ratio  $\mu_p = m_p/m_e$ , the function  $f_{spin-avg}^{(theor)}$  is fitted using  $\mu_p$  as an independent parameter, such that

$$f_{spin-avg}^{(theor)}(\mu_p) = f_{spin-avg}^{(exp)}. \quad (30)$$

The required fundamental constants are taken from CODATA2018[2], except for the ratio  $m_d/m_p$ , which is taken from a recent precise Penning trap measurement[110]. The resulting value has a total fractional uncertainty  $u_r = 3.5 \times 10^{-11}$ [109, eq. 6]:

$$m_p/m_e = 1,836.152\,673\,383 \quad (11)_{exp} (31)_{theor,QED} (55)_{theor,spin} (13)_{CODATA2018,Fink-Meyers} \quad (31)$$

It is consistent with recent results obtained from two-photon spectroscopy of  $\text{HD}^+$  by another group [12], the value previously obtained in [10] and values obtained from Penning trap measurements [111, 112]. Alternatively, the ratio of the reduced nuclear mass  $\mu$  to the electron mass can be determined [109, eq. 5]:

$$\mu = \frac{m_p \cdot m_d}{m_p + m_d} \quad (32)$$

$$\mu/m_e = 1,223.899\,228\,668\,(7)_{\text{exp}}\,(20)_{\text{theor,QED}}\,(37)_{\text{theor,spin}}\,(3)_{\text{CODATA2018}} \quad (33)$$

This value is consistent with CODATA2018, Penning trap measurements [11, 110, 112, 113] and the value obtained in [10].

The results obtained in this section are of importance, because they extend the previous work of spectroscopy in the Lamb-Dicke regime from rotational to ro-vibrational transitions, providing access to tests of more aspects of the theoretical calculations. The fact that they agree with results obtained from other work on  $\text{HD}^+$ , which relies on different transitions and a different spectroscopy method, show that both the theoretical and experimental aspects of the work are well under control. Also, they provide a good consistency check for the determinations of constants with other methods, like Penning traps.

## 6 Cumulative part of the dissertation

## **6.1 Article: UV source for laser-cooling based on quintupling**

The material presented in this chapter has been published as:

S. Vasilyev, A. Nevsky, I. Ernsting, M. Hansen, J. Shen, and S. Schiller, “Compact all-solid-state continuous-wave single-frequency UV source with frequency stabilization for laser cooling of  $\text{Be}^+$  ions,” *Applied Physics B*, volume 103, number 1, pages 27–33, 2011, ISSN: 1432-0649. DOI: 10.1007/s00340-011-4435-1

### **6.1.1 Contributions of the various authors**

Sergey V. Vasliyev and Alexander Nevsky built the source. Ingo Ernsting performed the frequency stability measurements. Jianwei Shen and I performed the integration of the system into the ion-trap setup. Stephan Schiller conceived the study and supervised the work.

### **6.1.2 Copyright**

Unfortunately, due to copyright restrictions, the final, peer-reviewed version of the article can not be reproduced in this thesis. The interested reader is advised to obtain the final version from the journal, as linked to in the above citation.

## 6.2 Article: Rotational THz spectroscopy

The material presented in this chapter has been published as:

J. Shen, A. Borodin, M. Hansen, and S. Schiller, “Observation of a rotational transition of trapped and sympathetically cooled molecular ions,” *Physical Review A*, volume 85, page 032 519, issue 3, 2012. DOI: 10.1103/PhysRevA.85.032519. arXiv: 1202.5672 [quant-ph]

### 6.2.1 Contributions of the various authors

I integrated the THz-source into the spectroscopy system’s control software. Further, I improved the data recording and evaluation system in such a way that the system operator could easily visualize the acquired spectrum in near real time. Jianwei Shen and Andrii Borodin performed the measurements. Stephan Schiller conceived the study, supervised the work and wrote the publication. All authors mentioned above contributed to the manuscript.

### 6.2.2 Copyright

Copyright 2012 by the American Physical Society

I have obtained permission from the publisher to reproduce this article in this thesis.



**Observation of a rotational transition of trapped and sympathetically cooled molecular ions**Copyright 2012 by the American Physical Society. Weblink: <http://dx.doi.org/10.1103/PhysRevA.85.032519>

J. Shen, A. Borodin, M. Hansen, and S. Schiller

*Institut für Experimentalphysik, Heinrich-Heine-Universität Düsseldorf, 40225 Düsseldorf, Germany*

(Received 16 January 2012; published 29 March 2012)

We demonstrate rotational excitation of molecular ions that are sympathetically cooled by laser-cooled atomic ions to a temperature as low as approximately 10 mK. The molecular hydrogen ions  $\text{HD}^+$  and the fundamental rotational transition  $(v = 0, N = 0) \rightarrow (v' = 0, N' = 1)$  at 1.3 THz, the most fundamental dipole-allowed rotational transition of any molecule, are used as a test case. This transition has not been observed before. Rotational laser cooling was employed in order to increase the signal, and resonance-enhanced multiphoton dissociation was used as detection method. The black-body-radiation-induced rotational excitation is also observed. The extension of the method to other molecular species is briefly discussed.

DOI: [10.1103/PhysRevA.85.032519](https://doi.org/10.1103/PhysRevA.85.032519)

PACS number(s): 33.20.Bx

**I. INTRODUCTION**

High-resolution laboratory rotational spectroscopy of molecules is an important and very well-developed technique in molecular physics. It has provided extensive data on and insight into the structure and dynamics of molecules and has several applications, including the identification of molecular species in interstellar clouds. In the recent past, the accessible spectral region has been extended from the microwave region to the terahertz (submillimeter wavelength) region, thanks to the development of appropriate terahertz radiation sources attaining useful power levels. Continuous-wave, narrow-linewidth terahertz radiation, suitable for high-resolution molecular spectroscopy, is available from backward-wave oscillators or via frequency upconversion using Schottky diodes [1,2] or semiconductor superlattices [3,4].

The resolution of rotational spectroscopy has been increased beyond the Doppler limit by several techniques, such as molecular beams [5], velocity-class selection [6], Lamb-dip spectroscopy, and two-photon spectroscopy [7]. For example, sub-Doppler spectral lines with widths of approximately 15 kHz around 100 GHz [8] and 30–40 kHz at 0.7–1 THz [9,10] have been reported. However, the resolution of such methods is limited by transition time broadening and/or pressure broadening. In order to eventually overcome these limitations, it is interesting to explore a fundamentally different regime: trapping cold ( $<1$  K) molecules in an interaction-free (ultra-high-vacuum) environment and localization to submillimeter extension. Then, transition time broadening and pressure broadening, as well as Doppler broadening, may be strongly reduced or even eliminated altogether. This regime may be reached with cold neutral molecules stored in e.g. optical traps or with cold molecular ions in radio-frequency traps. The production methods of cold molecules have been reviewed elsewhere; see, for example, Refs. [11,12].

In this work, we take a step toward applying high-resolution rotational spectroscopy on cold molecules: we demonstrate rotational excitation on sympathetically cooled and strongly confined molecular ions, using here secular temperatures as low as 10–15 mK. Our spectroscopic technique is a destructive one, resonance-enhanced multiphoton dissociation (REMPD). The particular implementation used here is  $1 + 1' + 1''$  REMPD, where the molecule absorbs sequentially three photons of different energies. In our work, the transitions

induced by each photon corresponds to the three main energy scales of a molecule: rotational (here ca. 1 THz), vibrational (here: overtone, ca. 200 THz), and electronic (ca. 1100 THz).

With respect to the temperature of the ions and the detection method, our work is complementary to the recent demonstration of terahertz rotational spectroscopy of trapped, helium-buffer-gas-cooled  $\text{H}_2\text{D}^+$  and  $\text{D}_2\text{H}^+$  ions at kinetic ion temperatures of approximately 24 K, where Doppler broadening is limiting the linewidth to approximately 1 MHz [13].

**II. THE  $\text{HD}^+$  MOLECULE AND THE SPECTROSCOPIC TECHNIQUE**

The molecule we consider here,  $\text{HD}^+$ , is the most fundamental molecule with electric dipole-allowed rotational transitions [14]. Its potential as a test system for molecular quantum mechanics and for novel fundamental physics studies has been described previously [14–19]. Vibrational spectroscopy of sympathetically cooled  $\text{HD}^+$  with the highest resolution of any molecular ion to date has recently been reported by us [20]. Pure rotational transitions have so far been observed only for the last and penultimate vibrational levels,  $v = 21, 22$ , close to the dissociation limit [21,22], where their  $N = 0 \rightarrow N' = 1$  transition frequencies lie in the microwave range (ca. 50 and 9.4 GHz, respectively). Here we report on the rotational transition in the  $v = 0$  ground vibrational level, at much higher frequency. The rovibrational transition frequencies have been calculated *ab initio* with high precision [18,19], greatly facilitating the experimental search. The  $(v = 0, N = 0) \rightarrow (v' = 0, N' = 1)$  fundamental rotational transition studied here occurs at  $f_{0,\text{theor}} = 1\,314\,925.752$  MHz (“spinless” value, i.e., excluding hyperfine energy contributions), with an estimated theoretical error of approximately 2 kHz [23]. The  $f_{0,\text{theor}}$  value includes (among others) a contribution of approximately 48.8 MHz from relativistic effects (order  $\alpha^2$ ) and approximately  $-9.4$  MHz from QED effects of order  $\alpha^3$ .

An important aspect of this work is the use of laser rotational cooling [24]; see Fig. 1. It is used to transfer most of the molecular population, initially distributed among several rotational levels in  $v = 0$ , into the rovibrational ground state ( $v = 0, N = 0$ ) and it also empties the spectroscopy target state ( $v' = 0, N' = 1$ ). It modifies the difference in fractional population of the lower and upper spectroscopy levels, from

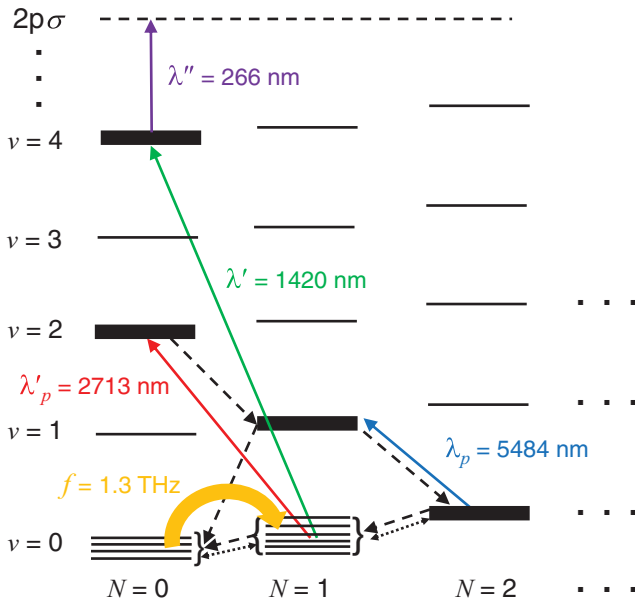


FIG. 1. (Color online) Simplified energy level scheme of  $\text{HD}^+$  with transitions relevant to this work. Full thin arrows, laser-induced transitions; dashed arrows, some relevant spontaneous emission transitions; and dotted double arrows, some relevant black-body-radiation-induced transitions. The terahertz wave (thick arrow) is tuned so that the four hyperfine states in  $(v=0, N=0)$  are excited to corresponding hyperfine states in  $(v'=0, N'=1)$ . Resonant laser radiation at  $\lambda'$  (1420 nm) and nonresonant radiation at  $\lambda''$  (266 nm) transfer the rotationally excited molecules to a vibrationally excited level  $(v''=4, N''=0)$  and then further to electronically excited molecular states (predominantly  $2p\sigma$ ), from which they dissociate. Rotational cooling is performed by radiation at  $\lambda_p$  (5.5  $\mu\text{m}$ ) and  $\lambda'_p$  (2.7  $\mu\text{m}$ ). The level energy differences are not to scale. Hyperfine structure is indicated very schematically for the levels  $(v=0, N=0, 1)$  and as thick lines for some other participating levels. The waves at  $\lambda', \lambda'', \lambda_p, \lambda'_p$  have relatively large spectral linewidths.

approximately  $-0.15$  in thermal equilibrium to approximately  $0.7$ , and thus significantly increases the detectable signal.

The hyperfine structure and the Zeeman effect of the lower and upper rovibrational levels are important aspects in the rotational spectroscopy [25,26]. As Fig. 2 shows, the ground state possesses four hyperfine states and 12 magnetic substates (with magnetic quantum number  $J_z$ ). In the region occupied by the ions in our apparatus, the magnetic field is nonzero, lifting the magnetic degeneracy. The spectrum contains a large number of transitions with relatively large transition dipole moments; see Fig. 3. Most transitions, even the  $\Delta J_z = 0$  ones, shift by approximately 100 kHz or more in a field of strength 1 G. Exceptions include five (strong)  $J_z = 0 \rightarrow J'_z = 0$  transitions, whose quadratic Zeeman shifts in 1 G are at most 6.2 kHz in absolute value [26]. From each lower hyperfine state there is at least one such transition; the state  $(F=0, S=1, J=1, J_z=0)$  has two. Three of them are indicated by the first, third, and fourth arrows (from the top) in Fig. 2. A fourth is the hyperfine transition  $(F=1, S=1, J=1, J_z=0) \rightarrow (F'=1, S'=1, J'=2, J'_z=0)$ . Its transition frequency  $f = f_{0,\text{theor}} + 11.78$  MHz is close to other transition frequencies and is therefore

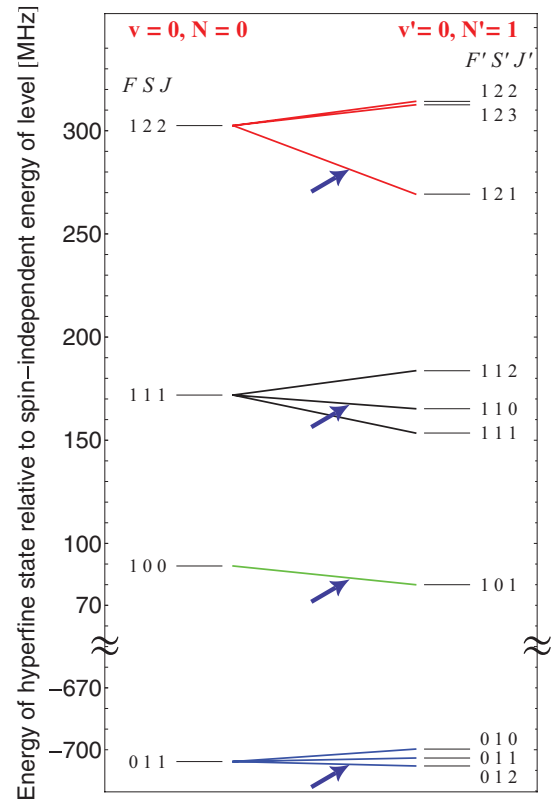


FIG. 2. (Color online) Energy diagram of the hyperfine states and main electric-dipole transitions in zero magnetic field. Left side, rovibrational ground level  $(v=0, N=0)$ ; right side, rotationally excited level  $(v'=0, N'=1)$ . The hyperfine states are labeled by the (in part approximate) quantum numbers  $(F, S, J)$ . The degeneracy factor of each hyperfine state is  $(2J+1)$ . Transitions that do not change the quantum numbers  $F, S$  are relatively strong and are indicated, starting from the top of the figure, by red, black, green, and blue lines. The four transitions addressed consecutively in this work are indicated by arrows.

not considered suitable for the present work. Instead, we use the  $(F=1, S=1, J=1, J_z=0) \rightarrow (F'=1, S'=1, J'=0, J'_z=0)$  transition (second arrow from the top in Fig. 2), which, however, exhibits a much larger quadratic Zeeman effect (78 kHz at 1 G). The magnetic field in the trap region is not spatially constant in direction and magnitude, so some line broadening can be expected.

The theoretical Doppler linewidth, considering only secular motion, is approximately 55–70 kHz for the lowest temperatures used here (10–15 mK) and approximately 150–200 kHz if the ion ensemble is in the liquid state (100–200 mK). Note that the values are relatively large due to the low mass of the  $\text{HD}^+$  ion. At 10–15 mK, the molecular ions are well confined along the axis of the trap and their motion in transverse direction is restricted to a range smaller than the terahertz wavelength (0.23 mm). In the axial direction, the confinement is not as strong, since diffusive motion of the ions is still occurring along the crystal axis, which exceeds in length (ca. 1.5 mm) the terahertz wavelength. Thus, Doppler broadening may still be present in our experiment, even at the lowest temperatures. The terahertz source [27] has a linewidth below

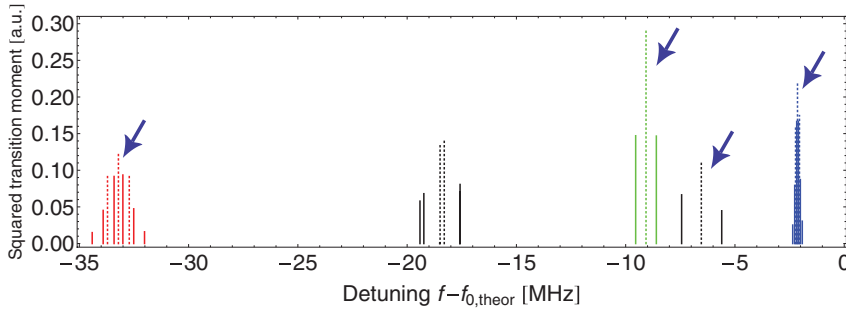


FIG. 3. (Color online) Section of the theoretical stick spectrum of the rotational transition in the frequency range relevant to this work, showing the Zeeman splittings and shifts in a 1 G magnetic field. Dashed lines are  $\pi$  transitions; full lines are  $\sigma$  transitions.  $f_{0,\text{theor}}$  is the theoretical “spinless” transition frequency. The four terahertz frequencies of list A (see Table I) are indicated by the arrows. The colors used correspond to those used in Fig. 2.

100 Hz and subhertz absolute frequency stability, values that are not relevant in comparison to other line-broadening effects.

The Doppler linewidth is smaller than the typical spacing between hyperfine transitions originating from different ground hyperfine states, even in the presence of a magnetic field on the order of 1 G. This is in principle advantageous, since it could permit resolution of the hyperfine structure. However, detecting individual hyperfine lines would also lead to a small signal-to-noise ratio: The individual hyperfine levels each contain only a fraction of the total population. If a statistical population distribution were produced by action of the black-body radiation field (BBR) and of the rotational cooling lasers, each substate would contain  $1/12$  of the total population, this fraction being typically 20 to 30 molecules. The individual populations are likely to vary significantly in time, requiring the collection of substantial data and averaging. We do not attempt to do so here and in order to obtain a sufficiently strong rotational excitation signal we have applied the following strategy.

We irradiate the molecules sequentially on terahertz frequencies corresponding to strong hyperfine transitions. Different frequency sets are used; see Table I. Each frequency from a set is irradiated for 200 ms and is meanwhile frequency-modulated by  $\pm 2$  kHz at a 5 Hz rate. The list is repeated several times for a total of 3 s or more, depending of the excitation approach used.

The frequency lists include three of the five above mentioned low-Zeeman-shift  $J_z = 0 \rightarrow J'_z = 0$  transitions, which originate from three of the four hyperfine states of ( $v = 0, N = 0$ ), and the respective frequency values have been chosen to correspond to an assumed magnetic field of 1 G. As mentioned above, the chosen transition starting from the fourth hyperfine state ( $F = 1, S = 1, J = 1$ ) has a substantial quadratic Zeeman effect. We therefore attempt to

compensate for the lack of precise knowledge of the magnetic field distribution by exciting at four distinct frequencies, corresponding to the shifts induced by the magnetic field values 0.25, 0.5, 0.75, and 1 G (the detuning for 0 G is  $-6.617$  MHz). Altogether, this list of frequencies (denoted by  $A'$ ; see Table I) should nominally excite four of the twelve Zeeman substates. However, in the presence of a significant Doppler broadening, more substates (with larger Zeeman shifts) will be addressed. Indeed, the frequencies necessary to excite all Zeeman substates of the ground hyperfine states fall into ranges of approximately  $\pm 0.5, \pm 1, 0, \pm 0.22$  MHz at 1 G, relative to the frequencies of the list  $A'$ . These spreads have a partial overlap with the Doppler broadening at the higher molecular temperatures (100–200 mK) employed here.

In order to obtain information about the detuning dependence of the rotational excitation, we also apply “detuned-frequency lists.” Lists labeled  $B$  and  $C$  are detuned to smaller and larger frequencies, respectively, relative to list  $A'$  (relative detunings of list  $B$ :  $-1.782, -1.311, -0.704, -0.327$  MHz, relative detunings of list  $C$ :  $1.803, 1.443, 0.714, 0.326$  MHz). The detunings are larger than the shift induced by the Zeeman effect in a 1 G field. Lists  $D$  and  $E$  have relative detunings approximately half as large as those of lists  $B$  and  $C$ , respectively (list  $D$ :  $-0.891, -0.655, -0.352, -0.163$  MHz, list  $E$ :  $0.901, 0.722, 0.357, 0.163$  MHz). Finally, list  $A$  is also used, which is a simplified version of list  $A'$ . Frequency modulation is used in all cases.

### III. EXPERIMENTAL APPARATUS AND PROCEDURE

A schematic of our apparatus [28] is shown in Fig. 4. The ultra-high vacuum (UHV) chamber houses a linear ion trap driven at 14.2 MHz. HD gas is loaded into the chamber by opening a piezoelectric valve, after which it is ionized by an

TABLE I. Frequency lists used for excitation of the rotational transition.  $f_i$  is the terahertz frequency.

Lower hyperfine level ( $F, S, J$ )	Frequency $f_i - f_{0, \text{theor}}$ (MHz)						
	(1,2,2)		(1,1,1)			(1,0,0)	(0,1,1)
List $A'$	-33.211	-6.597	-6.578	-6.558	-6.539	-9.069	-2.138
List $A$	-33.211			-6.539		-9.069	-2.138
List $B$	-34.993			-7.850		-9.773	-2.465
List $C$	-31.408			-5.096		-8.355	-1.812
List $D$	-34.102			-7.194		-9.421	-2.301
List $E$	-32.310			-5.817		-8.712	-1.975
500-MHz detuning				500			

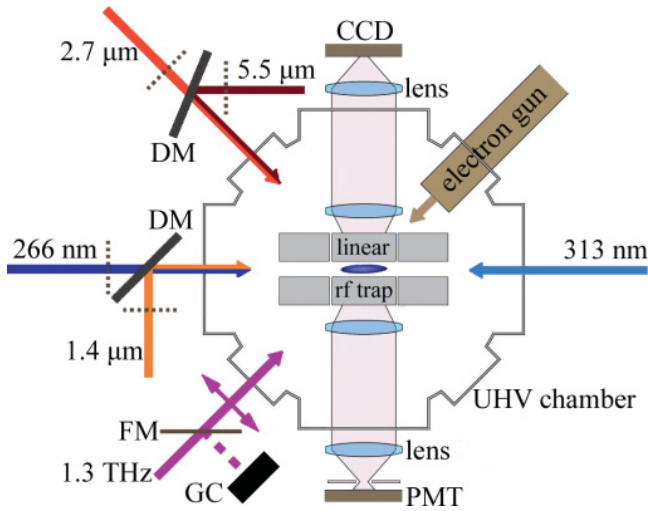


FIG. 4. (Color online) Schematic of the apparatus and beams. GC, Golay cell; FM, flip mirror; DM, dichroic mirror; and dotted lines, electrically controlled laser beam shutters. The double arrow indicates the polarization of the terahertz wave. Not to scale.

electron gun. The laser radiation for REMP enters from the left and the 313 nm cooling radiation [29] enters from the right. The rotational cooling radiation enters diagonally. The terahertz source is positioned close to the vacuum chamber and its wave is focused into the chamber center by a concave paraboloidal mirror oriented at right angle to the beam. With a manual flip mirror, the wave can be sent to a Golay cell detector for power-monitoring purposes. The terahertz source has been described previously [27]. It is driven at the 72nd subharmonic of the desired frequency, near 18 GHz. This signal is provided by a microwave synthesizer, which is frequency locked to a global positioning system (GPS)-referenced hydrogen maser. The first REMP laser is a diode laser emitting at the wavelength  $\lambda = 1420$  nm and exciting the  $(v = 0, N = 1) \rightarrow (v' = 4, N' = 0)$  transition. The second REMP laser excitation is nonresonant and is provided by a resonantly frequency-doubled 532 nm laser. Initially, a  $\text{Be}^+$  ion crystal is produced in the trap. Typically, the same  $\text{Be}^+$  ion crystal is used for several hours of experimentation.

The molecular sample preparation routine starts by frequency stabilization of the cooling laser to a frequency a few tens of MHz to the red of the frequency for optimal  $\text{Be}^+$  cooling, using a hyperfine transition of molecular iodine as reference. Then, a small amount of HD gas is let into the chamber and ionized by the electron gun. Both  $\text{HD}^+$  ions as well as heavy impurity ions are generated, trapped, and quickly sympathetically cooled. In order to remove these impurity ions, the DC quadrupole potential is briefly increased, reducing the quasipotential strength in one transverse direction. The heavy ions then escape from the trapping region. This ends the preparation procedure; the produced cold  $\text{HD}^+$  sample contains typically approximately 300 molecules.

The acquisition of one data point proceeds as follows: (i) The terahertz excitation is initially effectively kept off by detuning the frequency by 500 MHz from the rotational resonance, and the REMP lasers are also blocked. (ii) The rotational cooling laser beams are unblocked, and a

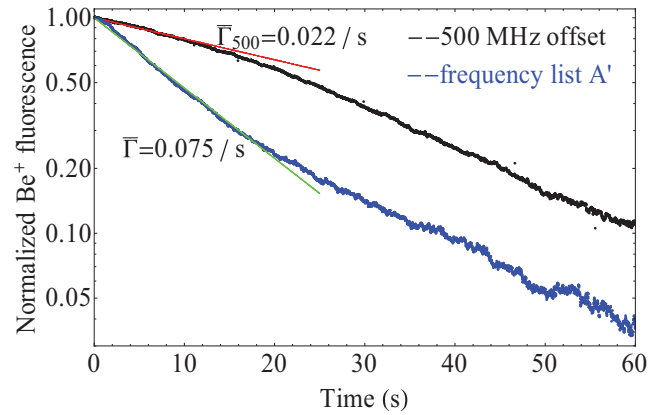


FIG. 5. (Color online) Atomic fluorescence signal during continuous secular excitation of the  $\text{HD}^+$  ions (method I, liquid state). The time axis starts after the  $2.7 \mu\text{m}$  rotational cooling laser is turned off and the two REMP lasers and terahertz radiation are turned on. The upper (black) trace, where the terahertz radiation is detuned from resonance, shows the molecular ion number decay due mainly to the effect of BBR-induced rotational excitation. Lower (blue) trace is for terahertz radiation on resonance. Each trace is the average of 10 individual decays. The lines are exponential fits to the first 10 s of the data.

repeated secular frequency scan (740–900 kHz) is activated and kept on during the remainder of the measurement cycle (method I). The heating of the molecular ions heats the  $\text{Be}^+$  ions sympathetically and spectrally broadens their 313 nm absorption line. This leads to a substantial increase of the cooling-laser-stimulated atomic fluorescence, due to the laser's relatively large detuning from atomic resonance. The fluorescence signal level is indicative of the initial number of  $\text{HD}^+$  in the ion ensemble. (iii) For a duration  $T_c = 35$  s, the rotational cooling takes place, after which the  $2.7 \mu\text{m}$  rotational cooling laser is blocked (not the  $5.5 \mu\text{m}$  laser). (iv) The REMP lasers are unblocked and simultaneously the terahertz frequency scan is initiated. The resulting molecule loss reduces the heating and thus the atomic fluorescence signal. (v) The change in fluorescence as a function of time is followed until the signal essentially reaches the level in the absence of molecules. (Figure 5 displays the first 60 s only.) The secular excitation is kept on all the time. This concludes acquisition of one data point.

In an alternative measurement mode (method II), the secular scan activated in step (ii) to obtain a normalization signal is turned off after a few seconds while the rotational cooling continues. At the end of step (iii), both rotational cooling lasers are blocked. In step (iv), the terahertz source and the REMP lasers are turned on only for 3 s. Immediately afterward, in step (v) the secular excitation is turned on again and the reduced fluorescence level is recorded during a few seconds. The ratio of the two fluorescence levels defines our signal and gives approximately the relative decrease in  $\text{HD}^+$  number after REMP.

At the end of either procedure, residual  $\text{HD}^+$  and product ions are removed from the trap by applying the following cleaning procedure. (In method II, we do not “reuse” the remaining molecules, as we prefer to excite molecular samples prepared in the same way each time.) The cooling laser is



detuned by a few 100 MHz to the red of the atomic cooling transition, causing melting of the crystal into a liquid. A secular excitation frequency scan covering the frequencies of  $\text{HD}^+$  and lighter ions is turned on. The cooling laser is briefly blocked and unblocked several times. Light ions are thereby ejected from the trap. The secular excitation is turned off and the system is ready for a new molecule loading.

#### IV. RESULTS AND DISCUSSION

The first set of measurements was taken in the liquid state using method I. Figure 5 shows two atomic fluorescence traces. The upper (black, “background”) trace was obtained with the terahertz wave frequency detuned by 500 MHz from  $f_{0,\text{theor}}$ , a value where no transition line exists. The REMPD only dissociates molecules in the ( $v = 0$ ,  $N = 1$ ) level. This level has initially been depopulated by the  $2.7\text{ }\mu\text{m}$  rotational cooling laser, which is favorable for the purpose of the spectroscopy. As soon as the spectroscopy phase starts, the level receives population not only by terahertz rotational excitation (if the frequency is near resonance), but also by BBR-induced excitation from all hyperfine states of the ground rovibrational level (rate ca. 0.09/s at 300 K). In addition, the population still present in the ( $v = 0$ ,  $N = 2$ ) level or reaching it from higher-lying rotational levels is transferred into ( $v = 0$ ,  $N = 1$ ) by BBR-stimulated emission (rate ca. 0.12/s) and spontaneous emission (rate ca. 0.06/s). Therefore, a REMPD-induced molecule loss is always present.

A rate equation simulation yields a BBR-induced molecule number decay rate that depends on REMPD laser intensities and reaches ca. 0.075/s in the limit of very high intensities. After partial optimization of the UV dissociation laser alignment onto the ion crystal and therefore maximization of its intensity, we observed values of ca. 0.04/s at 25 s after the REMPD laser was turned on. The rate at this time rather than at 0 s is considered since at 0 s the number of molecules present is larger and this may lead to some saturation of the secular excitation signal. We explain the difference compared to the theoretical maximum by the actually available laser power and possibly imperfect REMPD laser beams overlap. With an improved alignment of the UV laser, an increase of the BBR-induced decay rate to ca. 0.060/s was observed.

The lower (blue) trace represents the decay in the presence of resonant terahertz radiation, using frequency list  $A'$ . We observe a large difference in the initial rate of signal decrease as compared to the background trace. Note that the decay occurring in the presence of resonant terahertz radiation also contains the background decay.

We also performed measurements with the two frequency lists  $B$  and  $C$ , for which the frequencies were detuned from those of list  $A'$  by different amounts for the four hyperfine states. As Fig. 6 (top) shows, the decay rates do not differ significantly from the background decay rates, and we can therefore deduce an upper limit for the magnetic field of 1.5 G, as the influence of the Doppler width is not significant here.

A second set of measurements was taken with method II; see Fig. 6 (bottom). Here, the terahertz radiation

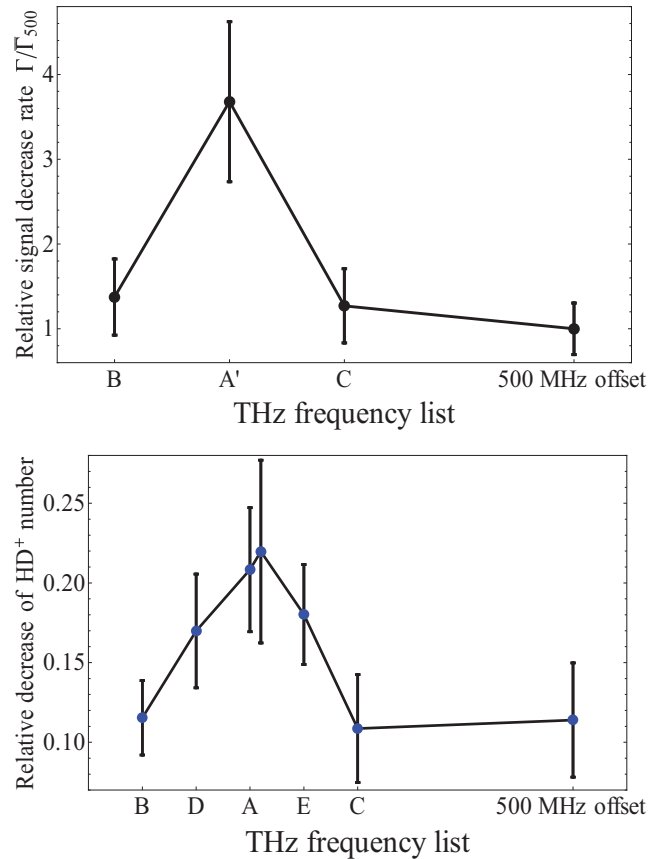


FIG. 6. (Color online) Frequency dependence of the rotational excitation. Top, in the liquid state, at ca. 100–200 mK, using method I.  $\bar{\Gamma}_{500}$  is the average decay rate when the terahertz radiation frequency is detuned by 500 MHz. Each data point results from nine individual decays. Bottom, in the crystallized state, at 10–15 mK, using method II. Each data point represents the mean of nine or ten measurements. The two close points were taken with the same list  $A$  on different days and are shown separated for clarity. The error bars in both plots show the standard deviations of the data, not of the mean. The lines are guides for the eye.

is applied only when the ion ensemble is well crystallized, at temperatures of approximately 10–15 mK. Data points were taken alternately at 500 MHz detuning, with list  $A$ , with list  $B$  ( $D$ ), and with list  $C$  ( $E$ ). Again, a finite (background) signal is observed when the terahertz radiation is far detuned, since BBR excites the rotational transition significantly on the used time scale of 3 s. Irradiation with the frequency list  $A$  provides a clear signal that rotational excitation induced by terahertz radiation takes place. We find again no significant difference in the rotational excitation efficiency for the detunings of lists  $B$  and  $C$ , compared to the background measurement. However, reducing the detunings to half the values (lists  $D$  and  $E$ ) shows an increase of signal. This increase can be explained by the presence of a magnetic field of ca. 1 G or a Doppler width of several 100 kHz, or a combination of both. However, the Doppler width is at most 70 kHz under the operating conditions, and therefore we conclude that we observed the effect of the magnetic field on the hyperfine transition frequencies.

## V. CONCLUSION

We observed a pure rotational excitation of a sympathetically cooled molecular ion ensemble. In order to facilitate the observation, we applied a scheme adapted to the particularities of the apparatus. As the available detection scheme is a destructive one that employs photodissociation of the rotationally excited molecules, a new molecular ion loading cycle has to be implemented for each data point, and the data acquisition rate is very low. The number of ions sympathetically cooled is also small. Therefore, the preparation of a significant fraction (ca. 70%) of the molecular ions in the lower spectroscopic level was essential. Even so, the detection of a rotational transition originating from a single hyperfine state has too low of a signal-to-noise ratio. This is also due to the concurrent process of BBR-induced rotational excitation, which yields a finite background signal (decay rate) in connection with the photodissociation.

We therefore applied terahertz radiation at four frequencies that nominally excite the four hyperfine states in the lower spectroscopic level. This allowed a clear observation of the rotational excitation, using two different methods. By applying terahertz radiation detuned from the nominal resonance frequencies by amounts varying from 0.16 to 0.9 MHz (absolute) for the four frequencies, we found a significantly reduced but still observable excitation. This can be explained by the presence of a magnetic field with values up to approximately 1 G. In comparison, the contribution of secular ion motion to the linewidth when the ions are at approximately 10 mK and well-confined is negligible.

There is a strong motivation for further development of the method demonstrated here, since a resolution of the hyperfine structure of  $\text{HD}^+$  and an accurate measurement of the hyperfine transition frequencies would represent a significant test of the *ab initio* calculations of this molecule. Possible improvements are the application of hyperfine state preparation techniques, recently demonstrated [20], and accurate control of the magnetic field in the trap region.

Finally, it is useful to consider the extension of this work to other molecular species. These can be characterized by their mass and their rotational constant, which are to a certain extent related. For many species, the masses will be significantly larger and the rotational constants significantly smaller than in the case of  $\text{HD}^+$ . The smaller rotational constant will lead to a significantly smaller transition frequency, in the microwave regime. It is likely that the Lamb-Dicke regime will then be effective, in particular if the microwave propagation direction is along the narrow width of the molecular ion ensemble, and Doppler broadening would be absent altogether. The smaller rotational constant will also lead to a smaller black-body-radiation excitation rate (at 300 K), which is very favorable, since it will make possible REMPD with near-zero background. The experimentally demonstrated fraction of molecules in the ground state obtained by applying rotational cooling on such heavier molecules is so far significantly below the level used here on  $\text{HD}^+$  [30], but simulations [31] show that similar levels should be achievable with appropriate laser cooling schemes and laser systems. Hyperfine structure and Zeeman shift coefficients will be molecule-specific. Molecular ions in an electronic spin singlet state are particularly interesting, as they would have a reduced number of hyperfine states, of Zeeman substates, and much reduced linear Zeeman shift coefficients, simplifying and narrowing the spectrum. Thus, the extension of rotational spectroscopy of sympathetically cooled molecular ions to other species appears very promising.

## ACKNOWLEDGMENTS

This work was funded by the DFG (Project Schi 431/11-1) and by an equipment grant of the Heinrich-Heine-Universität. We thank F. Lewen for the loan of equipment and V. Korobov for communication of unpublished results. We are indebted to B. Roth and T. Schneider for their contributions in the initial phase of this study.

- 
- [1] F. Lewen, S. P. Belov, F. Maiwald, T. Klaus, and G. Winnewisser, *Z. Naturforsch. A* **50**, 1182 (1995).
  - [2] A. Maestrini, J. Ward, G. Chattopadhyay, E. Schlecht, and I. Mehdi, *Frequenz—J. RF Engineer.* **62**, 118 (2008).
  - [3] F. Klappenberger, K. F. Renk, P. Renk, B. Rieder, Y. I. Koshurinov, D. G. Pavelev, V. Ustinov, A. Zhukov, N. Maleev, and A. Vasilyev, *Appl. Phys. Lett.* **84**, 3924 (2004).
  - [4] C. P. Endres, F. Lewen, T. F. Giesen, S. Schlemmer, D. G. Pavelev, Y. I. Koschurinov, V. M. Ustinov, and A. E. Zhucov, *Rev. Sci. Instrum.* **78**, 043106 (2007).
  - [5] See, e.g., H. W. Kroto, *Molecular Rotation Spectra* (Wiley, London, 1975).
  - [6] S. Carocci, A. Di Lieto, A. Menciassi, P. Minguzzi, and M. Tonelli, *J. Mol. Spectrosc.* **175**, 62 (1996).
  - [7] L. A. Surin, B. S. Dumes, F. S. Rusin, G. Winnewisser, and I. Pak, *Phys. Rev. Lett.* **86**, 2002 (2001).
  - [8] G. Cazzoli, L. Dore, C. Puzzarini, and S. Beninati, *Phys. Chem. Chem. Phys.* **4**, 3575 (2002).
  - [9] G. Winnewisser, S. P. Belov, Th. Klaus, and R. Schieder, *J. Mol. Spectrosc.* **184**, 468 (1997).
  - [10] V. Ahrens, F. Lewen, S. Takano, G. Winnewisser, S. Urbana, A. A. Negirev, and A. N. Koroliev, *Z. Naturforsch. A* **57**, 669 (2002).
  - [11] R. Krems, B. Friedrich, and W. C. Stwalley, eds., *Cold Molecules* (CRC Press, Boca Raton, FL, 2009).
  - [12] I. W. M. Smith, ed., *Low Temperatures and Cold Molecules* (World Scientific Publishing, Singapore, 2008).
  - [13] O. Asvany, O. Ricken, H. S. P. Müller, M. C. Wiedner, T. F. Giesen, and S. Schlemmer, *Phys. Rev. Lett.* **100**, 233004 (2008).
  - [14] W. H. Wing, G. A. Ruff, W. E. Lamb, and J. J. Spezeski, *Phys. Rev. Lett.* **36**, 1488 (1976).
  - [15] A. Carrington, I. R. McNab, and C. A. Montgomery, *J. Phys. B* **22**, 3551 (1989).
  - [16] J. C. J. Koelemeij, B. Roth, A. Wicht, I. Ernsting, and S. Schiller, *Phys. Rev. Lett.* **98**, 1730024 (2007).

- [17] S. Schiller and V. Korobov, [Phys. Rev. A \*\*71\*\*, 032505 \(2005\)](#).
- [18] V. I. Korobov, [Phys. Rev. A \*\*74\*\*, 052506 \(2006\)](#).
- [19] V. I. Korobov, [Phys. Rev. A \*\*77\*\*, 022509 \(2008\)](#).
- [20] U. Bressel *et al.*, to appear in *Phys. Rev. Lett.* (2012).
- [21] A. Carrington, C. A. Leach, A. J. Marr, R. E. Moss, C. H. Pyne, and T. C. Steimle, [J. Chem. Phys. \*\*98\*\*, 5290 \(1993\)](#).
- [22] A. Carrington, I. R. McNab, C. A. Montgomerie, and J. M. Brown, [Mol. Phys. \*\*66\*\*, 1279 \(1989\)](#).
- [23] V. I. Korobov (private communication).
- [24] T. Schneider, B. Roth, H. Duncker, I. Ernsting, and S. Schiller, [Nat. Phys. \*\*6\*\*, 275 \(2010\)](#).
- [25] D. Bakalov, V. I. Korobov, and S. Schiller, [Phys. Rev. Lett. \*\*97\*\*, 243001 \(2006\)](#).
- [26] D. Bakalov, V. I. Korobov, and S. Schiller, [J. Phys. B \*\*44\*\*, 025003 \(2011\)](#).
- [27] S. Schiller, B. Roth, F. Lewen, O. Ricken, and M. Wiedner, [Appl. Phys. B \*\*95\*\*, 55 \(2009\)](#).
- [28] P. Blythe, B. Roth, U. Fröhlich, H. Wenz, and S. Schiller, [Phys. Rev. Lett. \*\*95\*\*, 183002 \(2005\)](#).
- [29] S. Vasilyev, A. Nevsky, I. Ernsting, M. Hansen, J. Shen, and S. Schiller, [Appl. Phys. B \*\*103\*\*, 27 \(2011\)](#).
- [30] P. Sta anum, K. Højbjerg, P. Skyt, A. Hansen, and M. Drewsen, [Nat. Phys. \*\*6\*\*, 271 \(2010\)](#).
- [31] See the Supplemental Materials in Ref. [24].

### 6.3 Article: Ro-vibrational spectroscopy of $\text{HD}^+$

The material presented in this chapter has been published as:

U. Bressel, A. Borodin, J. Shen, M. Hansen, I. Ernsting, and S. Schiller, “Manipulation of Individual Hyperfine States in Cold Trapped Molecular Ions and Application to  $\text{HD}^+$  Frequency Metrology,” *Physical Review Letters*, volume 108, page 183 003, issue 18, 2012. DOI: 10.1103/PhysRevLett.108.183003. arXiv: 1203.2153 [physics.atom-ph]

#### 6.3.1 Contributions of the various authors

Ulf Bressel built the source and operated it during the measurements. Ingo Ernsting performed the frequency metrology of the source’s radiation. I integrated the spectroscopic source into the control software of the measurement system and performed improvements on the evaluation scripts, allowing the operator to produce a spectrum in near real time. Jianwei Shen and Andrii Borodin operated the ion trap. Stephan Schiller conceived the study, performed the data analysis, wrote the manuscript and supervised the work. All authors mentioned above contributed to the manuscript.

#### 6.3.2 Copyright

Copyright 2012 by the American Physical Society

I have obtained permission from the publisher to reproduce this article in this thesis.



**Manipulation of Individual Hyperfine States in Cold Trapped Molecular Ions and Application to  $\text{HD}^+$  Frequency Metrology**

U. Bressel, A. Borodin, J. Shen, M. Hansen, I. Ernsting, and S. Schiller

*Institut für Experimentalphysik, Heinrich-Heine-Universität Düsseldorf, Universitätsstr. 1, 40225 Düsseldorf, Germany*

(Received 20 November 2011; published 3 May 2012)

Advanced techniques for manipulation of internal states, standard in atomic physics, are demonstrated for a charged molecular species for the first time. We address individual hyperfine states of rovibrational levels of a diatomic ion by optical excitation of individual hyperfine transitions, and achieve controlled transfer of population into a selected hyperfine state. We use molecular hydrogen ions ( $\text{HD}^+$ ) as a model system and employ a novel frequency-comb-based, continuous-wave 5  $\mu\text{m}$  laser spectrometer. The achieved spectral resolution is the highest obtained so far in the optical domain on a molecular ion species. As a consequence, we are also able to perform the most precise test yet of the *ab initio* theory of a molecule.

DOI: [10.1103/PhysRevLett.108.183003](https://doi.org/10.1103/PhysRevLett.108.183003)

PACS numbers: 37.10.Pq, 33.15.Mt, 33.15.Pw, 42.50.Xa

Cold trapped molecules [1,2] currently represent an intense field of activity relying on sophisticated methods of molecule production, translational and internal cooling, spectroscopy and sensitive detection. Many applications, such as chemical reaction studies [3,4], tests of molecular quantum theory [5], fundamental physics [6,7] and quantum computing [8] would benefit strongly from the availability of advanced manipulation techniques, already standard in atomic physics. These are not straightforward for molecules, and for charged molecules have not been demonstrated yet. Production methods for molecular ions (usually, e.g., by electron impact ionization) and, if heteronuclear, their interaction with the blackbody radiation of the surrounding vacuum chamber, usually lead to significant population of a substantial number of internal states. A first, important step in the manipulation of internal states of molecular ions is population transfer between rotational states (heteronuclear molecules usually being cold vibrationally, i.e., are all in the  $v = 0$  ground vibrational state). It has been demonstrated that a significant fraction (ca. 75%) of an ensemble of diatomic molecular ions can be pumped into the vibrational and rotational ground level ( $v = 0, N = 0$ ) [9,10]; see Fig. 1.

For a general diatomic molecule, however, this pumping is usually not capable of preparing molecules in a single quantum state, because spin interactions generate a hyperfine structure with several states in each rovibrational level. For example, a diatomic molecule with one unpaired electron ( $s_e = 1/2$ ), and nuclei with nuclear spins  $I_1 = 1/2$  and  $I_2 = 1$  (such as  $\text{HD}^+$ ) has 4 hyperfine states in zero magnetic field if the rotational angular momentum is  $N = 0$ , but 10 if  $N = 1$ , and 12 if  $N \geq 2$ ; see Fig. 2(a). The ability to address selectively molecules in one particular hyperfine state (or even in a single quantum state with a particular magnetic quantum number  $J_z$ ) and to transfer molecules from one hyperfine state to another are clearly important tools of a molecular

quantum toolbox that can be part of a full quantum state preparation procedure.

Complicating the addressing, the number of strong transitions between two given rovibrational levels ( $v, N$ ), ( $v', N'$ ) is equal to the larger of the two numbers of hyperfine states, i.e., potentially high, and with only small differences in transition frequency. Figure 2(b) shows as an example the case of the fundamental vibrational transition ( $v = 0, N = 0$ )  $\rightarrow$  ( $v' = 1, N' = 1$ ) in  $\text{HD}^+$ , where 10 strong transitions occur over a range of about 60 MHz ([11,12]). Addressing a single hyperfine state in a multispin molecule thus requires a spectroscopy that can resolve individual hyperfine lines in the spectrum.

In this work, our approach is based on one-photon laser excitation of the fundamental vibrational transition ( $0, 0$ )  $\rightarrow$  ( $1, 1$ ) at the wavelength  $\lambda_f$ , see Fig. 1. The relatively low transition frequency,  $\lambda_f > 2.5 \mu\text{m}$  for diatomics, in combination with the low secular kinetic energy  $k_B T_{\text{sec}}$  achievable by sympathetic cooling, yields a Doppler broadening  $\Delta\nu_D$  of the transitions that is smaller than many line spacings. This provides the desired quantum state selectivity for addressing some of the hyperfine states, using strong transitions. For our test case  $\text{HD}^+$ ,  $\lambda_f = 5.1 \mu\text{m}$ ,  $T_{\text{sec}} \approx 10 \text{ mK}$ ,  $\Delta\nu_D \approx 3 \text{ MHz}$ . Additionally, excitation of weak transitions [which violate the approximate selection rules  $\Delta F = 0$ ,  $\Delta S = 0$ , see Fig. 2(b)], provides selectivity for all hyperfine states, since for these transitions the frequency spacings are larger. Compared to the use of a pure rotational excitation ( $0, 0$ )  $\rightarrow$  ( $0, 1$ ) [13] or a microwave transition within a rovibrational level, the use of a vibrational transition has the advantage that the excitation may be followed by a much faster spontaneous decay from ( $1, 1$ ), either back into the ground rovibrational level (rate approx.  $6 \text{ s}^{-1}$ ) or into the relatively long-lived rotational level ( $v'' = 0, N'' = 2$ ) (rate approx.  $12 \text{ s}^{-1}$ ). This allows reasonably rapid pumping of the molecule (possibly after repeated absorption and spontaneous emission events) into

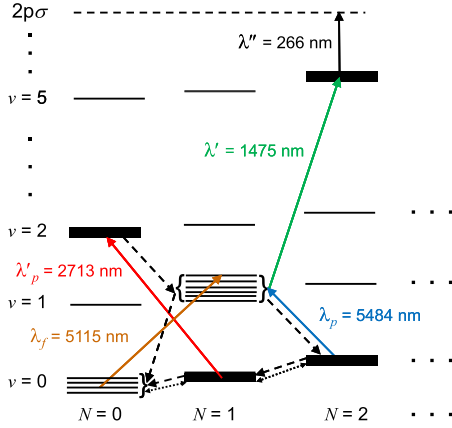


FIG. 1 (color online). Schematic energy level scheme of  $\text{HD}^+$  with transitions relevant to this work. Hyperfine structure is shown schematically only for the  $(v=0, N=0)$  and  $(1,1)$  levels as lines, but is implied for all other levels as well (thick bars). Full lines: laser-induced transitions; dashed lines: some relevant spontaneous emission transitions; dotted lines: some blackbody induced transitions. The spectrally narrow wave  $\lambda_f$  selectively excites molecules from a particular hyperfine state  $(v=0, N=0, F, S, J)$  to a single hyperfine state  $(1,1, F', S', J')$ . Quantum state preparation is performed by irradiating alternately the appropriately tuned waves  $\lambda_f$  and  $\lambda_p$ , in conjunction with spontaneous emission from the level  $(1,1)$ . Resonant laser radiation at  $\lambda'$  and nonresonant radiation at  $\lambda''$  is used to detect that hyperfine-state-selective excitation to the  $(1,1)$  level has occurred, by transferring the excited molecules to the electronically excited molecular state  $2p\sigma$  from which they dissociate. Initially, rotational cooling is performed by radiation at  $\lambda_p$  and  $\lambda'_p$ . The level energy differences are not to scale. The waves at  $\lambda', \lambda'', \lambda_p, \lambda'_p$  have large spectral linewidths and do not excite hyperfine state selectively.

another long-lived state, a necessary condition for efficient quantum state preparation, as shown below.

The experiment is performed on ensembles of  $\text{HD}^+$  ions trapped in a linear quadrupole radio-frequency trap (14.2 MHz), sympathetically translationally cooled by co-trapped, laser-cooled Beryllium atomic ions [14] and rotationally cooled by lasers. The  $\text{HD}^+$  molecule is of interest since it is a fundamental quantum system that allows precision measurements of QED effects and fundamental constants [5]. Our laser system consists of four subsystems: a  $\lambda_f = 5.1 \mu\text{m}$  laser spectrometer referenced to an atomic frequency standard [15] (see Supplemental Materials [16]), a reliable, frequency-stabilized fiber-laser-based 313 nm laser for cooling of Beryllium ions [17], a rotational cooling laser system (a  $\lambda_p = 5.5 \mu\text{m}$  quantum cascade laser and, for part of the measurements, a  $\lambda'_p = 2.7 \mu\text{m}$  diode laser), and a pair of lasers ( $\lambda, \lambda'$ ) for resonance-enhanced multiphoton dissociation (REMPD); see Fig. 1. Rotational cooling [9] is a crucial tool here, as it significantly increases the fractional population of molecules in the lower rovibrational level

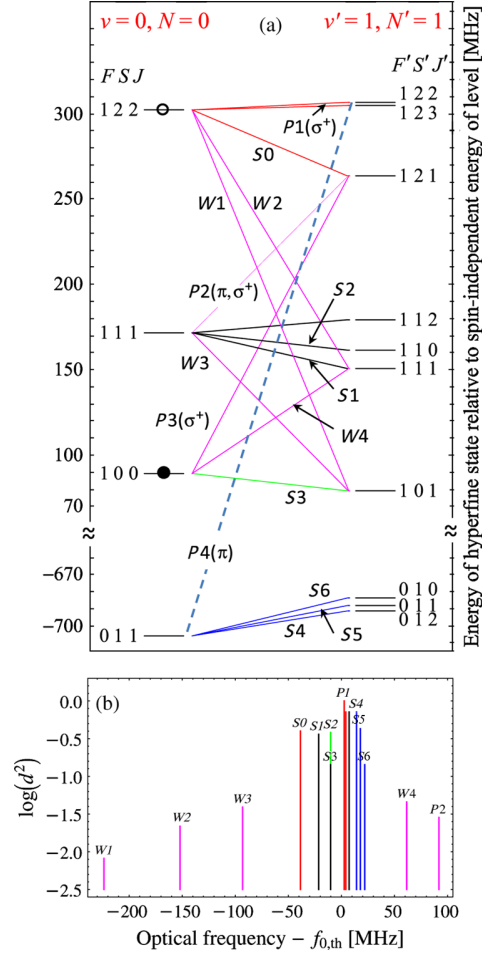


FIG. 2 (color online). (a) Energy diagram of the hyperfine states and main electric-dipole transitions in zero magnetic field. (b) Stick spectrum of the transitions (in zero magnetic field; values of the squared transition moment  $d^2$  are normalized to the strongest transition). The states are labeled by the quantum numbers  $(F, S, J)$ . Weak transitions are shown in pink [12]. Very weak transitions are not shown, except for  $P4$  (dashed). The “spin-independent” transition frequency  $f_{0,\text{th}}$  is the value if nuclear and electron spin were zero.  $S0, S1, S2, S3, S4, S5, S6, W1, W2, W3, W4, P2$  are transitions studied here (“W, S, P” mean “weak”, “strong”, and “pumping”, respectively). All were observed except  $S4$ .  $W1, W3$  are the transitions used here to achieve population transfer from the hyperfine states  $(v=0, N=0, F=1, S=2, J=2, J_z)$  (empty circle) and  $(0,0,1,1,1,J_z')$  into the hyperfine state  $(0,0,1,0,0,J_z')$  (filled circle).  $P1, P2, P3$ , and  $P4$  are proposed optical pumping transitions (with indicated polarizations) for preparation of the molecule in the single quantum state  $(0, 0, 1, 2, 2, J_z = +2)$  (one of the Zeeman states in the open circled hyperfine state).

$(v=0, N=0)$ , from ca. 10% to 60%–75%. The possibility provided by our laser system to measure the  $\text{HD}^+$  fundamental vibrational transition frequency  $f = c/\lambda_f$  also allows us to perform a precise comparison with the *ab initio* theory of the molecular hydrogen ion.

Hyperfine-resolved rovibrational transitions are induced by the  $\lambda_f = 5.1 \mu\text{m}$  radiation tuned precisely to individual transitions. We then detect (without hyperfine-state selectivity) the population of the goal vibrational level ( $v' = 1, N' = 1$ ), by  $1 + 1'$  resonance-enhanced multiphoton dissociation (REMPD) [18]; see Fig. 1. Together, this represents a three-photon ( $1 + 1' + 1''$ ) REMPD process. The reduction of the  $\text{HD}^+$  number by the REMPD process is our spectroscopic signal [18].

Figure 3 shows the obtained hyperfine-state resolved spectrum. All theoretically predicted and addressed hyperfine transitions were observed; only the (nominally strong) transition S4 is barely detected, for unknown reason. Transition W4, which originates from a lower hyperfine state with only a small fractional population ( $J = 0$ , thus statistically containing only 5%–6% of all molecules), could only be made clearly evident using a preceding hyperfine pumping step (see below). Each of the 4 hyperfine states of the lower level was selectively addressed, and 5 of the 12 upper level hyperfine states were selectively populated. We also observed the line at  $-10.2 \text{ MHz}$ , which contains two nearly coinciding transitions S2 and S3, but originating from different ground hyperfine states. The remaining strong transitions (including the line marked P1 in Fig. 2) were also observed, but their small spacing prevents complete resolution, and they are not reported in the Fig. 3.

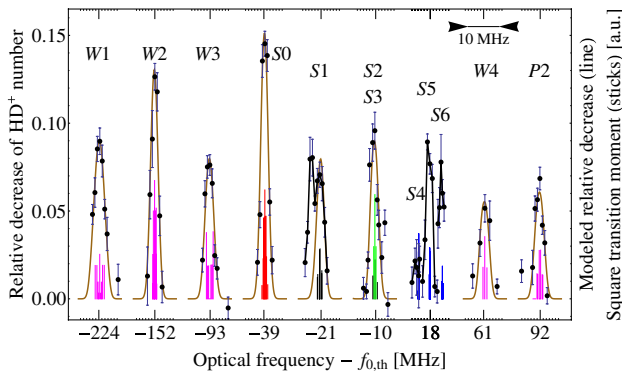


FIG. 3 (color online). Observed hyperfine spectrum of the  $(v = 0, N = 0) \rightarrow (1, 1)$  fundamental rovibrational transition in cold trapped  $\text{HD}^+$  ions. The effective intensity times irradiation duration product of the  $5.1 \mu\text{m}$  radiation varied from line to line, and was adapted to avoid saturation. Brown lines are the result of fitting  $f_{0,\text{exp}}$ , the individual line amplitudes, the Doppler temperature (9.5 mK) and the average magnetic field (0.8 G). The sticks are for illustration purpose and show the theoretical squared transition dipole moments for the Zeeman components at 0.8 G, assuming exciting radiation polarized at  $45^\circ$  to the magnetic field. They are scaled by different factors for presentation purpose. Color coding is as in Fig. 2. S4, S6 were taken at high intensity-irradiation time product, S5 at a lower value. The side peak of S1 is probably due to an ion micromotion sideband of S2/S3. The W4 line required hyperfine-state optical pumping for its detection (see Fig. 4).

We demonstrate hyperfine-state manipulation by optical pumping of individual hyperfine-state populations into a goal state. As a goal state we choose  $(v = 0, N = 0, F = 1, S = 0, J = 0, J_z = 0)$  which is nondegenerate ( $J = 0$ ) and thus a single quantum state (filled circle in Fig. 2). After rotational cooling, we apply the following sequence twice: W1 line (3 s), rotational repumping ( $\lambda_p$  and  $\lambda'_p$  simultaneously for 5 s), W3 line (3 s). A final 10 s of rotational repumping is performed before the spectroscopic excitation. The W1 and W3 transitions excite population from two initial hyperfine states  $(0, 0, 1, 2, 2, J_z)$ ,  $(0, 0, 1, 1, 1, J'_z)$  (without  $J_z$  selectivity) into the state  $(1, 1, 1, 0, 1, J''_z)$ . This state has dominant spontaneous decay to the goal state (green line S3 in Fig. 2). We find clear evidence that this hyperfine-state preparation is taking place by observing the transition W4 starting from the goal state by REMPD; see Fig. 4. This transition is not observable in our experiment without the preparation procedure, since then the population in the lower hyperfine state is too low.

Our hyperfine-state resolved spectrum represents the highest-resolution optical spectrum of any molecular ion so far [5,19,20]. This enables an accurate comparison of experimental frequencies with *ab initio* theory. We

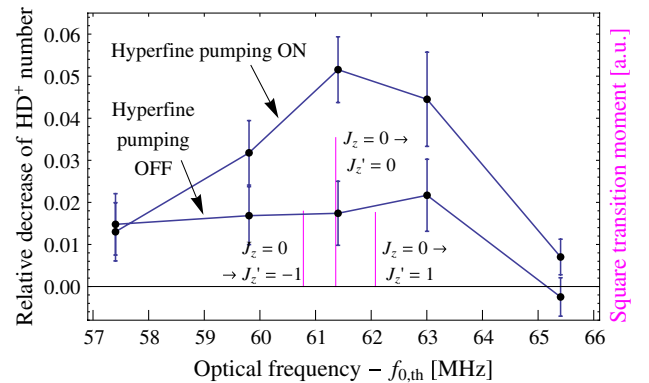


FIG. 4 (color online). Demonstration of hyperfine-state manipulation. The transition W4 shown here is observed only when hyperfine optical pumping is implemented. This transition represents the excitation from a single quantum state,  $(0,0,1,0,0, J_z = 0)$ . Data shown were taken alternating measurements preceded by hyperfine optical pumping (upper data points joined by line) and not (lower data points). The intensity of the  $5.1 \mu\text{m}$  laser radiation was set to its maximum both during hyperfine pumping on the W1 and W3 transitions and subsequent detection of the W4 transition. Irradiation time on the W4 transition was 3 s. Rotational cooling by the  $2.7 \mu\text{m}$  and  $5.5 \mu\text{m}$  laser was used. The zero level corresponds to the relative decrease measured when the  $5.1 \mu\text{m}$  spectroscopy laser was blocked. The three sticks show, for illustration purposes, the theoretical transition frequencies and strengths in a 0.8 G magnetic field and radiation polarized at  $45^\circ$  to the magnetic field. The shift of the central component is  $-0.05 \text{ MHz}$  relative to the zero-field frequency.

obtain two hyperfine-state separations in the ground state,  $\Delta f_{0,0,a} = (E(0, 0, 1, 2, 2) - E(0, 0, 1, 1, 1))/h$  and  $\Delta f_{0,0,b} = (E(0, 0, 1, 1, 1) - E(0, 0, 1, 0, 0))/h$ , from the measured transition frequency combinations  $f(S1) - f(W2)$ ,  $f(W3) - f(W1)$ ,  $f(P2) - f(S0)$ , and from  $f(W4) - f(S1)$ ,  $f(P3) - f(P2)$ , respectively. In addition, two excited state splittings,  $\Delta f_{1,1,c} = (E(1, 1, 1, 2, 1) - E(1, 1, 1, 1, 1))/h$  and  $\Delta f_{1,1,d} = (E(1, 1, 1, 1, 1) - E(1, 1, 1, 0, 1))/h$  are similarly obtainable by suitable frequency combinations. A fit of these hyperfine-state separations to the data (fitting also the spin-independent frequency) yields agreement with the *ab initio* results  $(\Delta f_{0,0,a}, \Delta f_{0,0,b}, \Delta f_{1,1,c}, \Delta f_{1,1,d}) = (130.60(1), 82.83(1), 113.33(1), 71.68(1))$  MHz [11,21], with deviations (experimental minus theoretical) of  $(-0.22(0.13), 0.28(0.38), -0.13(0.15), 0.27(0.19))$  MHz. The values in inner parentheses being the experimental uncertainties. The two measured hyperfine separations of the ground state also allow determining the two hyperfine constants  $E_4(0, 0)$ ,  $E_5(0, 0)$  [11] which fully describe the hyperfine structure of the ground state [12]. Our fit yields  $(E_4(0, 0), E_5(0, 0)) = (906(17), 142.33(25))$  MHz, whereas the theory values are  $(925.38(1), 142.29(1))$  MHz [11,21].

Assuming instead that the hyperfine energies are given by the theoretical values (this assumption being strengthened by the agreement of hyperfine theory and experiment for large- $\nu$  levels [11,22]), we can fit an overall frequency correction to the spectra  $W1, W2, W3, S0, S1, S2 + S3, W4, P2$ . We obtain the spin-independent frequency  $f_{0,\text{exp}} = 586\,050\,52.00$  MHz, with combined statistical and systematic error of 0.064 MHz (see Supplemental Material [16]). The theoretical value is  $f_{0,\text{th}} = 586\,050\,52.139(11)(21)$  MHz, where the first error is due to the uncertainty of the fundamental constants and the second is the theoretical error in the evaluation of the QED contributions [21,23,24]. The difference between experimental and theoretical results is  $-2.0$  times the combined theoretical plus experimental error. The relative experimental uncertainty of  $1.1 \times 10^{-9}$  represents the most accurate test of molecular theory to date. In particular, our measurement is the first molecular measurement sufficiently accurate to be explicitly sensitive to the QED contributions of order  $\alpha^5$  (relative to the nonrelativistic contribution to the transition frequency), calculated as 0.109(21) MHz for the transition studied here [21,24].

Based on the technique demonstrated here, we can propose a realistic optical pumping procedure for preparing most of the population in a single quantum state  $(\nu, N, F, S, J_z)$ , i.e., with well-defined projection of the total angular momentum. Under typical conditions, the relative statistical occupation of any individual quantum state in  $(\nu = 0, N = 0)$  is only  $\simeq (1/12) \times (60\%-75\%) \simeq 5\%-6\%$  under rotational cooling by a single laser ( $\lambda_p$ ) or two lasers ( $\lambda_p, \lambda'_p$ ). Exciting sequentially the four transitions  $P4$

$[(0, 0, 0, 1, 1) \rightarrow (1, 1, 1, 2, 2)], P3, P2, P1[(0, 0, 1, 2, 2) \rightarrow (1, 1, 1, 2, 3)]$  in a weak magnetic field and with polarizations chosen as indicated in Fig. 2(a) will cause transfer of the population of all Zeeman quantum states of  $(0, 0)$  to the single Zeeman quantum state  $(0, 0, 1, 2, 2, J_z = +2)$ , via spontaneous emission processes from  $(1, 1, 1, 2, J' = \{1, 2\}, J'_z)$ , which dominantly occur on strong transitions [red lines in Fig. 2(a)]. These excitations should be interleaved with rotational cooling (lasers  $\lambda_p, \lambda'_p$ ), which also serves as repumper following spontaneous decay into  $(\nu'' = 0, N'' = 2)$ . The optical pumping procedure should take a few ten seconds and lead to 60%–70% fractional population in the goal state.

In summary, we have shown that it is possible to address and prepare individual hyperfine states in cold, trapped diatomic molecular ions even in presence of a complex spin structure. A midinfrared laser spectrometer controlled by an atomic standard-referenced frequency comb, and sufficiently low ion kinetic energies were two important aspects. The observed, Doppler-limited, transition linewidths (3 MHz) are the lowest obtained to date on a molecular ion species in the optical domain [note that they scale as  $(\text{molecule mass})^{-1/2}$ ]. We also observed, for the first time to our knowledge, weakly allowed hyperfine transitions using optical excitation. As one application, we were able to directly determine the population fraction of molecules, in particular, hyperfine states. The largest value we found was 19%, clearly indicating the effectiveness of our rotational cooling. We also demonstrated excitation of a transition from a single quantum state. Since our test molecule  $\text{HD}^+$  is the simplest heteronuclear molecule and is excited from the rovibrational ground state, this study represents the first precision measurement of the most fundamental electric-dipole allowed rovibrational transition of any molecule [19]. A comparison of theory with experiment showed that (i) the hyperfine energies of small- $\nu, N$  rovibrational levels agree within deviations of less than 0.3 MHz and (ii) the spin-independent energy agrees within 2 times the relative error of  $1.1 \times 10^{-9}$ .

We are grateful to B. Roth, T. Schneider, A. Yu. Nevsky, and S. Vasilyev for help and support, and to V. Korobov for important discussions. Funding was provided by DFG project Schi 431/11-1.

- 
- [1] *Cold Molecules*, edited by R. Krems, B. Friedrich, and W. C. Stwalley (CRC Press, Boca Raton, 2009).
  - [2] *Low Temperatures and Cold Molecules*, edited by I. W. M. Smith (World Scientific Publishing, Singapore, 2008).
  - [3] B. Roth, P. Blythe, H. Wenz, H. Daerr, and S. Schiller, *Phys. Rev. A* **73**, 042712 (2006).
  - [4] P. F. Staunum, K. Højbjerg, R. Wester, and M. Drewsen, *Phys. Rev. Lett.* **100**, 243003 (2008).
  - [5] J. C. J. Koelemeij, B. Roth, A. Wicht, I. Ernsting, and S. Schiller, *Phys. Rev. Lett.* **98**, 173002 (2007).



- [6] S. Schiller and V. Korobov, *Phys. Rev. A* **71**, 032505 (2005).
- [7] H. Müller *et al.*, *Phys. Rev. A* **70**, 076004 (2004).
- [8] D. DeMille, *Phys. Rev. Lett.* **88**, 067901 (2002).
- [9] T. Schneider, B. Roth, H. Duncker, I. Ernsting, and S. Schiller, *Nature Phys.* **6**, 275 (2010).
- [10] P. Staantum, K. Højbjerg, P. S. Skyt, A. K. Hansen, and M. Drewsen, *Nature Phys.* **6**, 271 (2010).
- [11] D. Bakalov, V. I. Korobov, and S. Schiller, *Phys. Rev. Lett.* **97**, 243001 (2006).
- [12] D. Bakalov, V. I. Korobov, and S. Schiller, *J. Phys. B* **44**, 025003 (2011).
- [13] J. Shen, A. Borodin, M. Hansen, and S. Schiller, *Phys. Rev. A* **85**, 032519 (2012).
- [14] P. Blythe, B. Roth, U. Fröhlich, H. Wenz, and S. Schiller, *Phys. Rev. Lett.* **95**, 183002 (2005).
- [15] U. Bressel, I. Ernsting, and S. Schiller, *Opt. Lett.* **37**, 918 (2012).
- [16] See Supplemental Materials at <http://link.aps.org/supplemental/10.1103/PhysRevLett.108.183003> for details.
- [17] S. Vasilyev, A. Nevsky, I. Ernsting, M. Hansen, J. Shen and S. Schiller, *Appl. Phys. B* **103**, 27 (2011).
- [18] B. Roth, J. C. J. Koelemeij, H. Daerr, and S. Schiller, *Phys. Rev. A* **74**, 040501-4 (2006).
- [19] The  $(0, 1) \leftrightarrow (1, 0)$  transition has been measured in an ion beam experiment, with a linewidth  $\geq 7$  MHz and a frequency uncertainty  $\simeq 21$  MHz, W. H. Wing *et al.*, *Phys. Rev. Lett.* **36**, 1488 (1976); J. J. Spezeski, Ph.D. dissertation, Yale University, 1977.
- [20] H. C. Miller, M. Al-Za'al, and J. W. Farley, *Phys. Rev. Lett.* **58**, 2031 (1987).
- [21] V. I. Korobov, (private communication).
- [22] A. Carrington, I. R. McNab, C. A. Montgomerie-Leach, and R. A. Kennedy, *Mol. Phys.* **72**, 735 (1991).
- [23] V. I. Korobov, *Phys. Rev. A* **74**, 052506 (2006).
- [24] V. I. Korobov, *Phys. Rev. A* **77**, 022509 (2008).

## 6.4 Article: Frequency stabilization of a mid-IR QCL to a frequency comb

The material presented in this chapter has been published as:

M. G. Hansen, I. Ernsting, S. V. Vasilyev, A. Grisard, E. Lallier, B. Gérard, and S. Schiller, “Robust, frequency-stable and accurate mid-IR laser spectrometer based on frequency comb metrology of quantum cascade lasers up-converted in orientation-patterned GaAs,” *Optics Express*, volume 21, number 22, pages 27 043–27 056, 2013. DOI: 10.1364/OE.21.027043. arXiv: 1308.6430 [physics.optics]

### 6.4.1 Contributions of the various authors

Arnaud Grisard, Eric Lallier and Bruno Gérard fabricated the GaAs crystal used in this setup. I built the optical setup and worked with Ingo Ernsting on the frequency stabilization and measurement with the comb. We also performed the measurements. Sergey Vasilyev advised on the optical setup. Stephan Schiller conceived the system, wrote the manuscript and supervised the work. All authors mentioned above contributed to the manuscript.

### 6.4.2 Copyright

Unfortunately, due to copyright restrictions, the final, peer-reviewed version of the article can not be reproduced in this thesis. The interested reader is advised to obtain the final version from the journal or to obtain the pre-print version from [arxiv.org](http://arxiv.org), as linked to in the above citation.

## 6.5 Article: Linewidth-narrowing of a QCL

The material presented in this chapter has been published as:

M. G. Hansen, E. Magoulakis, Q.-F. Chen, I. Ernsting, and S. Schiller, “Quantum cascade laser-based mid-IR frequency metrology system with ultra-narrow linewidth and  $1 \times 10^{-13}$ -level frequency instability,” *Optics Letters*, volume 40, number 10, pages 2289–2292, 2015. DOI: 10.1364/OL.40.002289. arXiv: 1504.06216 [physics.optics]

### 6.5.1 Contributions of the various authors

Qun-Feng Chen implemented the optical setup around the cavity. Qun-Feng Chen, Evangelos Magoulakis and I implemented the lock to the cavity. Evangelos Magoulakis and I performed the measurements. Ingo Ernsting advised on interfacing the system with the frequency comb. Stephan Schiller conceived the study, wrote the manuscript and supervised the work. All authors mentioned above contributed to the manuscript.

### 6.5.2 Copyright

Unfortunately, due to copyright restrictions, the final, peer-reviewed version of the article can not be reproduced in this thesis. The interested reader is advised to obtain the final version from the journal or to obtain the pre-print version from [arxiv.org](https://arxiv.org), as linked to in the above citation.

## 6.6 Article: Rotational spectroscopy in the Lamb-Dicke regime

The material presented in this chapter has been published as:

S. Alighanbari, M. G. Hansen, V. I. Korobov, and S. Schiller, “Rotational spectroscopy of cold and trapped molecular ions in the Lamb-Dicke regime,” *Nature Physics*, volume 14, pages 555–559, 2018. DOI: 10.1038/s41567-018-0074-3. arXiv: 1802.03208 [quant-ph]

### 6.6.1 Contributions of the various authors

I supervised the implementation of a new stabilization system for the 2.7  $\mu\text{m}$  DFB laser, which was done by Soroosh Alighanbari during his master’s thesis [104]. More details about this work can be found in section 4.3. This increased the frequency agility and precision of the optical state preparation laser at 2.7  $\mu\text{m}$ , allowing for precise addressing of hyperfine states.

The components required for the automatized cleaning of the cold Beryllium host crystals were set up by Jana Scheuer during her Bachelor thesis [100], which Soroosh Alighanbari and I supervised. This led to an increase in the effective measurement time. I designed a new set of coils for generation of the magnetic field based on discussions with Soroosh Alighanbari. This helped to reduce fluctuations in the magnetic field, which in turn improved the reproducibility of the acquired spectra. Changes in the magnetic field lead to shifts in the transition frequencies. These shifts force the experimentator to first do a rough scan to find the peak position, before precision spectroscopy can be performed. The improved reproducibility can be seen in figure 4 of this publication. Here, the power dependency of the transition linewidth was measured in three measurement runs, which were performed on different days. The observed shift in the center of the peak is very small.

Using the frequency comb, I also verified the linewidth and spectral purity of the RF generator which drives the THz source. In this regard, the influence of stray ground currents on the reference to the hydrogen maser was also investigated and improved. Details and extensions of this work can be found in section 3.1.1 on page 18

Soroosh Alighanbari, Vladimir Korobov and Stephan Schiller performed theoretical calculations. Stephan Schiller conceived the study, wrote the manuscript and supervised the work. All authors mentioned above contributed to the manuscript.

### 6.6.2 Copyright

Unfortunately, due to copyright restrictions, the final, peer-reviewed version of the article can not be reproduced in this thesis. The interested reader is advised to obtain the final version from the journal or to obtain the pre-print version from arxiv.org, as linked to in the above citation.



## 6.7 Article: Characterization of a NEXCERA-resonator

The material presented in this chapter has been published as:

C. J. Kwong, M. G. Hansen, J. Sugawara, and S. Schiller, “Characterization of the long-term dimensional stability of a NEXCERA block using the optical resonator technique,” *Measurement Science and Technology*, volume 29, number 7, page 075 011, 2018. DOI: 10.1088/1361-6501/aac3b0. arXiv: 1805.08073 [physics.ins-det]

### 6.7.1 Contributions of the various authors

I advised on the setup for the frequency measurement of the 1064 nm reference laser using the frequency comb and helped with the interpretation of fluctuations in the measured frequency. I also verified the performance of the frequency comb with respect to the environmental conditions in the laboratory. Chang Jian Kwong built the setup and performed the measurements. Stephan Schiller conceived the study, wrote the manuscript and supervised the work. All authors mentioned above contributed to the manuscript. Jun Sugawara provided the cavity spacer.

### 6.7.2 Copyright

© IOP Publishing. Reproduced with permission. All rights reserved.

I have obtained permission from the publisher to reproduce this article in this thesis.

# Characterization of the long-term dimensional stability of a NEXCERA block using the optical resonator technique

Reprinted with permission from C. J. Kwong, M. G. Hansen, J. Sugawara, and S. Schiller, *Measurement Science and Technology*, volume 29, page 075011, 2018.

© IOP Publishing. Reproduced with permission. All rights reserved. Weblink: <http://dx.doi.org/10.1088/1361-6501/aac3b0>

**Chang Jian Kwong<sup>1</sup>**, **Michael G Hansen<sup>1</sup>**, **Jun Sugawara<sup>2</sup>**  
and **Stephan Schiller<sup>1</sup>**

<sup>1</sup> Institut für Experimentalphysik, Heinrich-Heine-Universität Düsseldorf, 40225 Düsseldorf, Germany

<sup>2</sup> Technical Management Department, Krosaki Harima Corporation, Kitakyushu-City 806-8586, Japan

E-mail: [Step.Schiller@hhu.de](mailto:Step.Schiller@hhu.de)

Received 2 January 2018, revised 12 April 2018

Accepted for publication 10 May 2018

Published 4 June 2018



## Abstract

NEXCERA is a machinable and highly polishable ceramic with attractive properties for use in precision instruments, in particular because its coefficient of thermal expansion exhibits a zero crossing at room temperature. We performed an accurate measurement of the long-term drift of the length of a 12 cm long NEXCERA block by using it as a spacer of a high-finesse optical cavity. At room temperature, we found a fractional length drift rate  $L^{-1}dL/dt = (-1.74 \pm 0.01) \times 10^{-8} \text{ yr}^{-1}$ .

**Keywords:** NEXCERA, dimensional stability, optical resonator, ULE, low thermal expansion ceramic, long-term frequency drift

(Some figures may appear in colour only in the online journal)

## 1. Introduction

Materials with ultra-low thermal expansion and high long-term dimensional stability are highly desirable in the field of precision instruments and metrology. Two well-known examples are ULE (ultra-low expansion glass) from Corning, Inc. and Zerodur from Schott AG. Both ULE and Zerodur have a small coefficient of thermal expansion  $\alpha$ , quoted as  $0 \pm 0.03 \times 10^{-6} \text{ K}^{-1}$  in the range 278 K–308 K [1], and  $0 \pm 0.006 \times 10^{-6} \text{ K}^{-1}$  in the range 273 K–323 K [2], respectively. The long-term dimensional stability of materials has been the subject of many studies, e.g. [3, 4]. For ULE, values of the fractional length drift rate  $L^{-1}dL/dt \approx -2.5 \times 10^{-8} \text{ yr}^{-1}$  have been reported [5], as well as significantly lower ones,  $-0.4 \times 10^{-8} \text{ yr}^{-1}$  [6]. Zerodur has a relatively large dimensional instability,  $-0.1 \times 10^{-6}$  to  $-0.2 \times 10^{-6} \text{ yr}^{-1}$  [5, 7], making it less suitable for applications requiring extreme long-term stability.

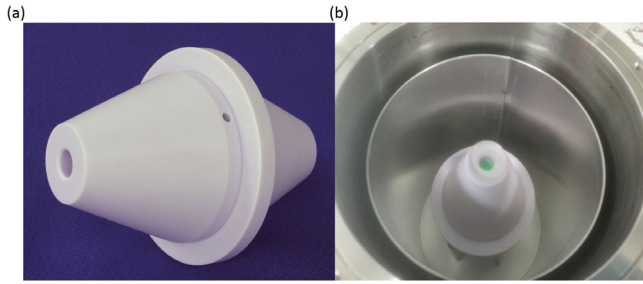
A relatively recent ultra-low thermal expansion ceramic, NEXCERA, developed by Krosaki Harima (Japan), is also a material of interest in instrumentation. NEXCERA can be produced with a thermal expansion coefficient

$|\alpha| < 0.03 \times 10^{-6} \text{ K}^{-1}$  at 23 °C. The Young's modulus, 140 GPa, is higher than that of both ULE (67.6 GPa) and Zerodur (90.3 GPa). NEXCERA's bulk density,  $2.58 \text{ g} \cdot \text{cm}^{-3}$ , is comparable to Zerodur ( $2.53 \text{ g} \cdot \text{cm}^{-3}$ ) but moderately higher than ULE's ( $2.21 \text{ g} \cdot \text{cm}^{-3}$ ).

The first characterization of the dimensional stability of NEXCERA was recently reported by Takahashi [8]. Length measurements of line scales made from NEXCERA showed that the ceramic has good long-term dimensional stability. The fractional length change  $\Delta L/L$  over a time interval of 13 months was determined as  $(1.1 \pm 1.1) \times 10^{-8}$  ( $2\sigma$  error) [8], which is consistent with zero length change. On fundamental grounds and for extremely demanding applications it is desirable to determine the dimensional stability of NEXCERA more precisely. This was the purpose of the present work.

An extremely sensitive method for determining the long-term dimensional stability of a material consists of manufacturing the material into a spacer for an optical cavity. One of the mode frequencies of such a cavity is then measured repeatedly against an atomic frequency standard.

For ULE, such measurements have been done in many laboratories worldwide. The lowest long-term linear drift



**Figure 1.** (a) NEXCERA spacer. (b) NEXCERA optical resonator within its vacuum chamber.

rates  $L^{-1}d\Delta L/dt \approx 5 \times 10^{-17} \text{ s}^{-1}$  ( $0.15 \times 10^{-8} \text{ yr}^{-1}$ ) have recently been found [9, 10]. Other measurements of ULE long-term linear drift include  $L^{-1}d\Delta L/dt = 2.04 \times 10^{-16} \text{ s}^{-1}$  ( $0.64 \times 10^{-8} \text{ yr}^{-1}$ ) [11] and  $L^{-1}d\Delta L/dt = 1.45 \times 10^{-16} \text{ s}^{-1}$  ( $0.44 \times 10^{-8} \text{ yr}^{-1}$ ) [12]. A measurement of the long-term linear drift rate of a Zerodur optical resonator has shown  $L^{-1}d\Delta L/dt = 3.05 \times 10^{-15} \text{ s}^{-1}$  ( $9 \times 10^{-8} \text{ yr}^{-1}$ ) [10], measured over 2 years.

A NEXCERA optical resonator has been realised by Hosaka *et al* [13]. It consisted of a 75 mm long cylindrical NEXCERA spacer and a pair of ULE mirror substrates. The temperature at which the coefficient of thermal expansion of the resonator is zero (zero-CTE temperature), was found to be at  $T_0 = 16.4 \pm 0.1 \text{ }^\circ\text{C}$  [13]. As an upper limit of the drift rate,  $L^{-1}|d\Delta L/dt| < 1.2 \times 10^{-7} \text{ yr}^{-1}$  was given. This corresponds to a drift of the optical frequency of  $1 \text{ Hz s}^{-1}$  at  $1.064 \text{ }\mu\text{m}$  wavelength.

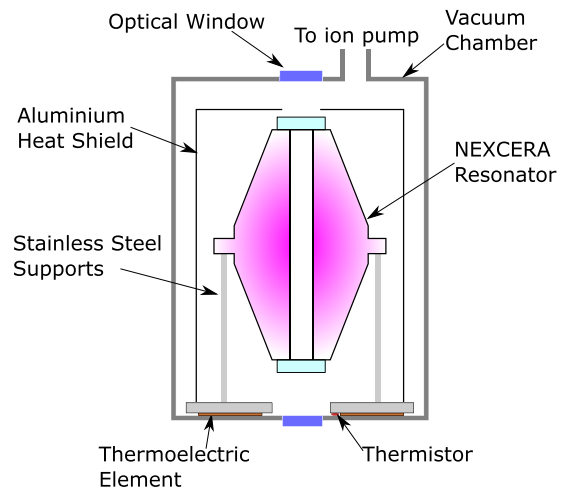
In this work, we present the first accurate measurement of the long-term drift of a NEXCERA N118C optical resonator, which is found to be nonzero.

This paper is structured as follows: the experimental setup is presented in section 2. The characterization of the zero-CTE temperature and the characterization of the long-term drift of the NEXCERA resonator are discussed in section 3. We draw conclusions in section 4.

## 2. Experimental setup

The NEXCERA sample we used (sample number N118C) was sintered in December 2015 and machined in March 2016. The resonator consists of a NEXCERA spacer of biconical shape with a central rim, see figure 1(a). The length is 120 mm, the conical angle is  $20^\circ$ . The diameter at the endfaces and of the rim are 30 mm and 90 mm respectively. A 10 mm diameter center bore allows the confined light to propagate in vacuum. Evacuation occurs via a 4 mm diameter transverse pumping hole.

Two ULE concave mirror substrates with 0.5 m radius of curvature, having a high reflectivity coating for 1064 nm, are optically contacted to the cavity spacer in-house. The contacting was done on 21 December 2016. The resonator linewidth was measured to be 20 kHz (FWHM) (finesse of  $6.2 \times 10^4$ ). Figures 1(b) and 2 illustrate the mounting of the NEXCERA resonator within a custom-made vacuum chamber. The NEXCERA cavity is placed vertically on three



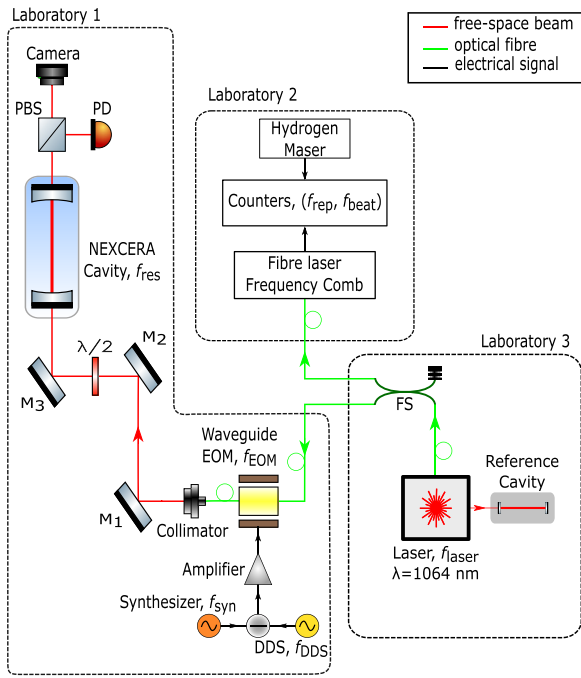
**Figure 2.** Schematic diagram of the NEXCERA resonator mounted within its vacuum chamber.

stainless steel supports with viton cylinders (approximately 5 mm long and 1.5 mm in diameter) placed in-between the supports and the resonator. These provide thermal insulation and mechanical damping. The steel supports are fixed to a base plate. Thermoelectric elements glued onto the bottom side of the base plate, together with a thermistor for temperature measurement, allow active stabilization of the temperature by a PID controller. The resonator and base plate are placed inside a polished aluminium heat shield which provides for further thermal insulation by reflecting radiative heat from the environment.

Figure 3 shows the optical setup. The frequency of a particular  $\text{TEM}_{00}$  mode of the resonator is interrogated by a Nd:YAG reference laser (frequency  $f_{\text{laser}}$ ) which is stabilized in frequency to an independent ultra-stable ULE reference cavity [14]. With a fibre splitter, the light from the reference laser is split into two arms. One arm directs the light to an erbium-doped fibre-based frequency comb referenced to a hydrogen maser, while the other arm sends the light to the NEXCERA cavity. The laser's frequency, as measured with the frequency comb, is determined from

$$f_{\text{laser}} = n f_{\text{rep}} \pm f_{\text{beat}} \pm f_{\text{offset}}, \quad (1)$$

where  $f_{\text{rep}}$  is the frequency comb repetition rate,  $f_{\text{beat}}$  is the frequency of the beat note between the selected mode of the frequency comb and the Nd:YAG laser,  $f_{\text{offset}}$  is the carrier envelope offset frequency and  $n$  is the number of the selected mode. In our apparatus,  $f_{\text{rep}} \approx 250 \text{ MHz}$ ,  $f_{\text{offset}} = 20 \text{ MHz}$ ,  $f_{\text{beat}} = 50 \text{ MHz}$ ,  $n \approx 1.126 \times 10^6$ . The sign of  $f_{\text{offset}}$  is determined by a particular setting of the locking electronics. The frequency of the laser is first coarsely measured with a wavemeter and the measured value,  $f_{\text{laser,w}}$  is used as a starting point for the more precise measurement with the frequency comb. The correct sign for  $f_{\text{beat}}$  in equation (1) is chosen so that the measured value of  $f_{\text{laser}}$  is closest to  $f_{\text{laser,w}}$ . With  $f_{\text{beat}}$  fixed at 50 MHz, the change in the frequency comb's repetition rate due to drifts of the reference laser  $f_{\text{laser}}$  can be determined with high precision.  $f_{\text{laser}}$ , as measured by the comb, is

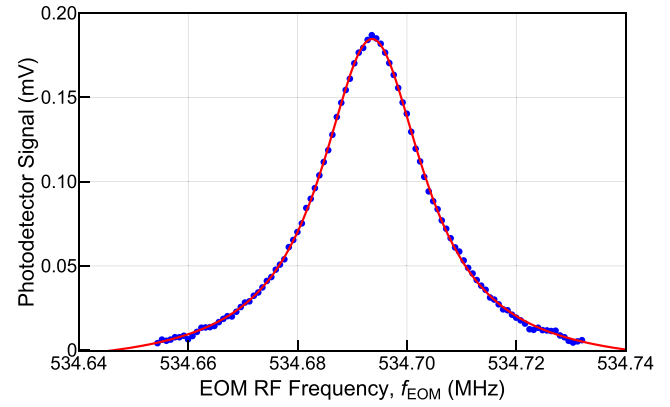


**Figure 3.** Schematic diagram of the optical setup for the characterization of the resonator's long-term frequency drift.

then averaged over the 15 s duration of each frequency scan, resulting in the average laser frequency,  $f_{\text{laser,av}}$  corresponding to each frequency scan. The averaging time of 15 s is chosen because it corresponds to the duration of one frequency scan of the NEXCERA cavity as explained below. Since the drift of the frequency-stabilized Nd:YAG laser is small ( $df_{\text{laser}}/dt = 0.055 \text{ Hz} \cdot \text{s}^{-1}$ ), its frequency does not change significantly during the averaging time.

The other part of the laser light that is transmitted through the NEXCERA cavity is split by a polarising beam splitter (PBS) and sent to a camera and a photodetector (PD) for measurement. A half-wave plate ( $\lambda/2$ ) is used for maximisation of the PD signal. Using a waveguide electro-optic modulator (EOM), we generate two sidebands on the laser wave before the light is sent to the NEXCERA cavity. The wave exiting from the EOM is coupled into a TEM<sub>00</sub> mode of the resonator. Due to frequency bandwidth limitations of the RF sources used, the RF signal driving the EOM (frequency  $f_{\text{EOM}}$ ) is produced by mixing an RF signal having constant frequency ( $f_{\text{syn}} = 607.663 \text{ MHz}$ ) with an RF signal (frequency  $f_{\text{DDS}} \approx 60 \text{ MHz}$ ) from a direct digital synthesizer (DDS),  $f_{\text{EOM}} = f_{\text{syn}} - f_{\text{DDS}}$ . By varying  $f_{\text{DDS}}$ , one of the laser sidebands can be scanned across the resonator's mode frequency. Thus, the resonator's frequency can be determined, as well as its linewidth. The synthesizer and the DDS are both referenced to the maser.

A computer controls the DDS and acquires the PD signal. The employed DDS frequency scan has a span of 100 kHz and a step size of 1 kHz with a dwell time of 150 ms. This amounts to 15 s duration per line scan. Such frequency scans are typically repeated for approximately 1 h during the measurement of resonator's frequency. The optical frequency measurement of the laser using the frequency comb is performed in parallel to the interrogation.



**Figure 4.** A resonator transmission signal recorded during a laser frequency scan. Blue: The transmission signal measured with PD. Red: Lorentzian fit to the data.

The determination of the Nd:YAG laser frequency and of the EOM drive frequency at which the resonator mode is maximally excited,  $f_{\text{EOM,res}}$ , allows us to determine the absolute resonator frequency  $f_{\text{res}} = f_{\text{laser,av}} \pm f_{\text{EOM,res}}$ . The sign is chosen according to which of the two sidebands interrogates the resonator.

### 3. Results and discussion

#### 3.1. Transmission signal measurement

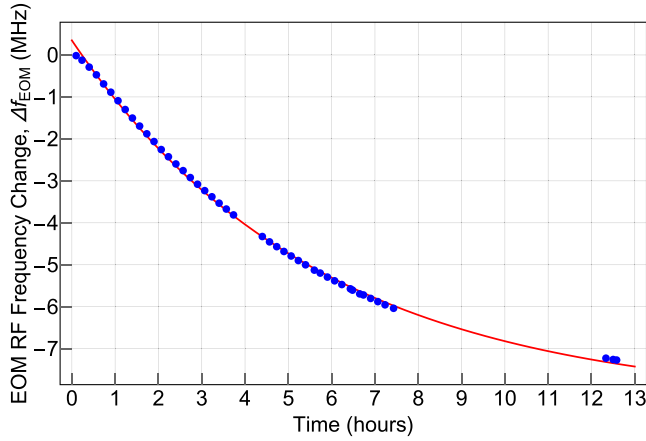
An example of a frequency scan over the resonance is shown in figure 4. A Lorentzian fit yields the sideband frequency for achieving resonance,  $f_{\text{EOM,res}}$ .

#### 3.2. Characterization of thermal expansion

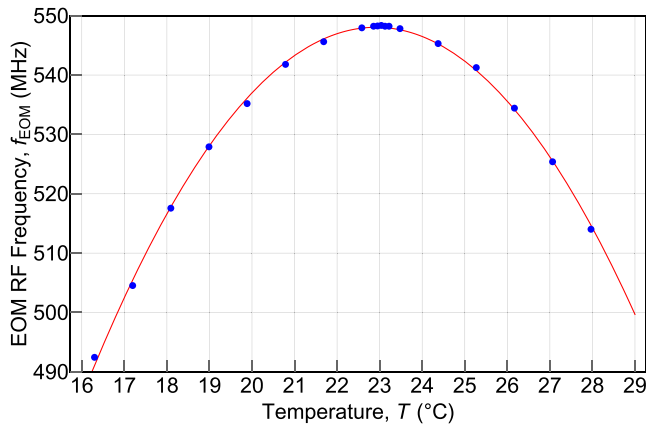
In order to achieve an accurate characterization of the resonator's long-term frequency drift, we first determine its thermal time constant. The resonator was initially set to 20 °C. After the set temperature was changed to 19 °C, the resonator's frequency was repeatedly measured at intervals of 10 min. The result is shown in figure 5. The thermal time constant is determined to be  $2 \times 10^4 \text{ s} \approx 5.6 \text{ h}$ , by fitting an exponential decay curve to the data.

Since the thermal settling follows an exponential decay, we decided to perform measurements always 8 h after the temperature change to allow for two measurements per workday and finding the zero-CTE point within a reasonable time. The resonator frequencies  $f_{\text{res}}(T)$  at temperatures  $T$  between 16 °C and 29 °C were measured at intervals of 1 K or smaller, in order to obtain a precise determination of the zero-CTE temperature. Here, measurement of only  $f_{\text{EOM}}$  is sufficient because the change in the resonator's frequency due to change in temperature is much larger than any drifts in the laser frequency. Figure 6 shows the data. A quadratic fit to the data was performed, and the zero-CTE temperature was determined from the turning point of the fit function.

The zero-CTE temperature is found to be at  $T_0 = 22.9 \pm 0.2 \text{ °C}$ . Both our measurement and the result by Hosaka *et al* [13], 16.4 °C, yield values near room temperature.



**Figure 5.** Determination of thermal time constant from the reaction of the resonator frequency to a 1 K temperature change of the set point. The EOM RF frequency change,  $\Delta f_{\text{EOM}} = f_{\text{EOM}} - f_{\text{EOM},0}$ . Blue: Data. Red: Exponential decay fit.



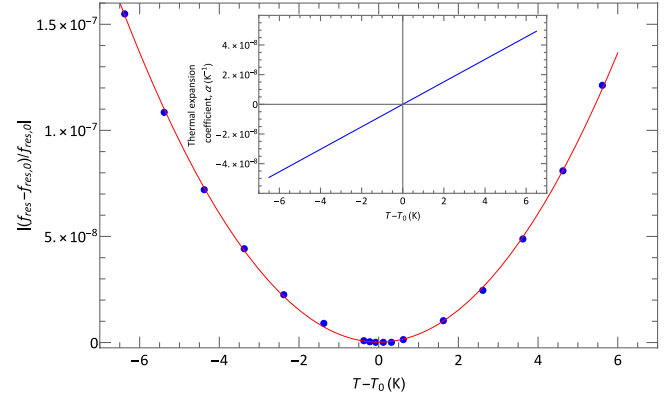
**Figure 6.** NEXCERA resonator frequency at temperatures between 16 °C and 29 °C. Blue: Measurement data. Red: A quadratic fit to the data.

From figure 7, a quadratic function is fitted to the experimental data. The thermal expansion coefficient,  $\alpha$ , i.e. the derivative of the fitted function, is shown in the inset. Our CTE temperature derivative,  $d\alpha(T_0)/dT = (7.58 \pm 0.08) \times 10^{-9} \text{ K}^{-2}$ , is approximately 2 times larger than the value of Hosaka *et al*  $(3.86 \pm 0.03) \times 10^{-9} \text{ K}^{-2}$ .

The NEXCERA resonator temperature was maintained at its zero-CTE temperature value throughout the characterization of its long-term frequency drift.

### 3.3. Absolute frequency measurements

For the characterization of long-term frequency drift, the cavity interrogations and Nd:YAG laser frequency measurements were performed once per weekday. Laser frequency measurements and sideband frequency  $f_{\text{EOM},\text{res}}$  were both averaged over approximately 30 min, and the resonator frequency  $f_{\text{res}}$  was computed from these time-averaged frequencies. The frequency change was then given by the difference between the resonator frequency relative to the initial frequency  $f_{\text{res}}(0)$ , i.e.  $\Delta f_{\text{res}}(t) = f_{\text{res}}(t) - f_{\text{res}}(0)$ . The initial



**Figure 7.** Normalised resonator frequency change around its zero-CTE temperature,  $T_0$ . Blue: Experimental data. Red: Quadratic fit to data. Inset: thermal expansion coefficient,  $\alpha$  as a function of temperature.

frequency measurement was performed on 25 April 2017, 125 d after optical contacting.

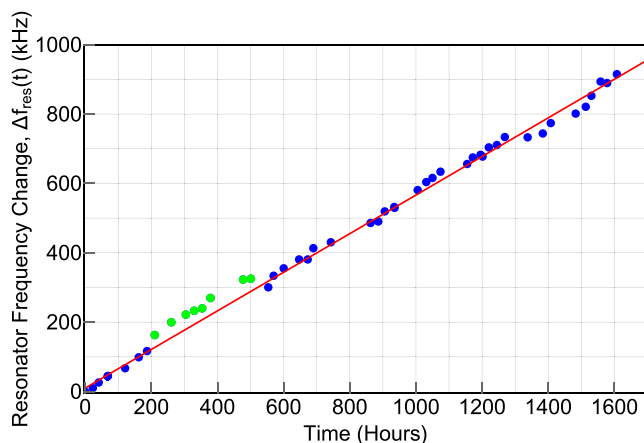
Figure 8 shows the resonator frequency change plotted against time. The frequency measurement was carried out over a period of approximately 1608 h, i.e. 67 d, as shown in figure 8. The data points, plotted in green, exhibit a temporary offset of 125 kHz which is likely due to external mechanical perturbations on the experimental setup. Over a period of approximately two weeks, a piezo-electric shaker was tested and characterised by using it to apply an external vibration onto the optical breadboard on which our experiment was set up. The data points plotted in green correspond to the frequency measurements made during this period. Hence, we suspect that the temporary offset is due to the residual effect of the strong vibration on the optical breadboard being transferred to the optical resonator.

From a linear fit to the data, we find  $d\Delta f_{\text{res}}/dt = (0.155 \pm 0.001) \text{ Hz} \cdot \text{s}^{-1}$ . The fit to the data was done excluding the green data points. This rate corresponds to a fractional frequency drift rate  $f_{\text{res}}(0)^{-1} d\Delta f_{\text{res}}/dt = (5.50 \pm 0.04) \times 10^{-16} \text{ s}^{-1}$ . The error is the statistical  $1\sigma$  standard error; systematic errors due to the frequency measurement technique are negligible.

## 4. Discussion and conclusion

We have precisely measured the drift of the frequency of a resonator comprising a NEXCERA spacer and a pair of high-finesse ULE mirrors. We have found a nonzero drift rate. If we neglect a possible contribution of the optical contacts between the ULE mirror substrates and the NEXCERA spacer, we can assign this frequency drift to an equal but opposite length drift rate  $L^{-1} dL/dt = -f_{\text{res}}(0)^{-1} d\Delta f_{\text{res}}/dt$ . Thus, we find a length contraction of  $(0.383 \pm 0.002) \text{ nm}$  over a period of approximately 67 d, i.e. a fractional length contraction rate of  $L^{-1} d\Delta L/dt = (-1.74 \pm 0.01) \times 10^{-8} \text{ yr}^{-1}$ . This rate is of the same sign and comparable in magnitude to that of ULE resonators. Indeed, the drift rate of our own ULE-resonator stabilized Nd:YAG laser (see figure 3) amounted





**Figure 8.** Long-term frequency drift of the NEXCERA resonator. The red line is a linear fit to the blue data points. The green data points are ignored.

to  $f_{\text{laser}}(0)^{-1} d\Delta f_{\text{laser}}/dt = (0.625 \pm 0.003) \times 10^{-8} \text{ yr}^{-1}$ . The error of our NEXCERA drift rate measurement is approximately  $0.01 \times 10^{-8} \text{ yr}^{-1}$ , 50 times lower compared to the measurement in [8].

To ensure that the long-term frequency drift measurement was not affected by the quality of the optical contacts, we tested them visually and mechanically after completion of the measurements. No conspicuous features were found.

In order to perform the optical contact bonding, both the resonator's spacer end faces and the contacting annulus of the high-finesse mirrors, which are highly polished, were cleaned thoroughly with lens tissue wet with ethanol. Inspection of the cleaned surfaces with a camera microscope allowed us to determine if the surfaces were cleaned satisfactorily. A thin film of air was formed in between the two thoroughly cleaned surfaces, allowing the mirror to frictionlessly 'glide' on the resonator's end face. A thoroughly cleaned surface enabled us to achieve contact bonding that fully covers the spacer-mirror interface. Partial bonding can be easily detected from the internal reflection of light at the interface that manifests itself as Newton's rings (in case of particle contamination) or as an interference pattern (in case of liquid contamination and inherent roughness of the surface). During our contacting, no partial bonding was detected. Moreover, tilting, shaking and pulling of the cavity mirrors from the resonator's spacer did not break the optical contact bonding. Our tests show that optical contact bonding was achieved fully across the resonator spacer-mirror interface. We believe that the present contacts were similar in quality as those made on ULE spacers in other work. On those, a resonator frequency drift due to contacting is not observed, also because of the inherent short 'length' of the contact region as compared to the spacer length. We therefore expect that the present optical contacts have, if any, only a minor effect on the observed drift.

Upon the completion of this work, an independent study on NEXCERA N117B has been published [15], where a significantly lower drift,  $0.005 \text{ Hz} \cdot \text{s}^{-1}$  was measured at the wavelength of 1064 nm. The NEXCERA N118C, used in our work and the N117B have similar chemical compositions and microstructures but are sintered in different atmospheres, the

N117B being sintered in argon atmosphere while N118C is sintered in air. In view of the differences in long-term drift between the materials, it is of interest to characterize more samples of these materials, in order to determine whether the observed drift rate difference is indeed a reproducible property.

Despite the difference in the measurement results of the long-term drifts for optical resonators made from different type of NEXCERA ceramic, the material remains promising for applications in the field of laser frequency stabilization. For such applications, first proposed by Hosaka *et al* [13], NEXCERA offers the advantage of larger ratio of Young's modulus to density, hence potentially lower acceleration sensitivity than ULE. Also, it can be produced in larger sizes (up to 1 m), potentially opening an avenue to lower thermal noise by increasing the resonator's length. The larger CTE temperature derivative compared to ULE can be compensated by advanced passive and active temperature stabilization.

## Acknowledgments

We are indebted to A Nevsky for help with the vacuum chamber as well as helpful discussions on this work, U Rosowski for help with the frequency comb measurement and E Wiens for help with the resonator scans. We thank D Iwaschko also for his support in providing the electronics of the experimental setup. We acknowledge useful discussions with D V Sutyryn, E Magoulakis, S Alighanbari and M Schioppo. This work was funded by European Union grants FP7-PEOPLE-2013-ITN Number 607491 'COMIQ' and FP7-PEOPLE-2013-ITN Number 607493 'FACT'.

## ORCID iDs

Chang Jian Kwong <https://orcid.org/0000-0001-5328-5853>  
 Michael G Hansen <https://orcid.org/0000-0001-5180-2511>  
 Stephan Schiller <https://orcid.org/0000-0002-0797-8648>

## References

- [1] Corning Inc. 2017 Manufacturer's Specification, ULE [www.corning.com/media/worldwide/csm/documents/7972%20ULE%20Product%20Information%20Jan%202016.pdf](http://www.corning.com/media/worldwide/csm/documents/7972%20ULE%20Product%20Information%20Jan%202016.pdf) (Accessed: 26-09-17)
- [2] Schott AG 2017 Manufacturer's Specification, Zerodur [www.schott.com/d/advanced\\_optics/f7ae3c11-0226-4808-90c7-59d6c8816daf/1.0/schott\\_zerodur\\_katalog\\_july\\_2011\\_en.pdf](http://www.schott.com/d/advanced_optics/f7ae3c11-0226-4808-90c7-59d6c8816daf/1.0/schott_zerodur_katalog_july_2011_en.pdf) (Accessed: 26-09-17)
- [3] Berthold J W, Jacobs S F and Norton M A 1977 Dimensional stability of fused silica, Invar, and several ultra-low thermal expansion materials *Metrologia* **13** 9
- [4] Jacobs S F and Bass D 1989 Improved dimensional stability of Corning 9600 and Schott Zerodur glass ceramics *Appl. Opt.* **28** 4045–6
- [5] Zhu M and Hall J L 1992 Short and long term stability of optical oscillators *Proc. 1992 IEEE Frequency Control Symp.* pp 44–55
- [6] Marnett L, Madej A A, Siemsen K J, Bernard J E and Whitford B G 1997 Precision frequency measurement of

- the  $^2S_{1/2}$ – $^2D_{5/2}$  transition of  $\text{Sr}^+$  with a 674 nm diode laser locked to an ultrastable cavity *IEEE Trans. Instrum. Meas.* **46** 169–73
- [7] Takahashi A 2010 Long-term dimensional stability and longitudinal uniformity of line scales made of glass ceramics *Meas. Sci. Technol.* **21** 105301
- [8] Takahashi A 2012 Long-term dimensional stability of a line scale made of low thermal expansion ceramic NEXCERA *Meas. Sci. Technol.* **23** 035001
- [9] Häfner S, Falke S, Grebing C, Vogt S, Legero T, Merimaa M, Lisdat C and Sterr U 2015  $8 \times 10^{-17}$  fractional laser frequency instability with a long room-temperature cavity *Opt. Lett.* **40** 2112–5
- [10] Keupp J, Douillet A, Mehlstäubler T E, Rehbein N, Rasel E M and Ertmer W 2005 A high-resolution Ramsey–Bordé spectrometer for optical clocks based on cold Mg atoms *Eur. Phys. J. D* **36** 289–94
- [11] Alnis J, Matveev A, Kolachevsky N, Udem T and Hänsch T W 2008 Subhertz linewidth diode lasers by stabilization to vibrationally and thermally compensated ultralow-expansion glass Fabry–Pérot cavities *Phys. Rev. A* **77** 053809
- [12] Keller J, Ignatovich S, Webster S A and Mehlstäubler T E 2014 Simple vibration-insensitive cavity for laser stabilization at the  $10^{-16}$  level *Appl. Phys. B* **116** 203–10
- [13] Hosaka K, Inaba H, Akamatsu D, Yasuda M, Sugawara J, Onae A and Hong F-L 2013 A Fabry–Pérot etalon with an ultralow expansion ceramic spacer *Japan. J. Appl. Phys.* **52** 032402
- [14] Chen Q-F, Nevsky A, Cardace M, Schiller S, Legero T, Häfner S, Uhde A and Sterr U 2014 A compact, robust, and transportable ultra-stable laser with a fractional frequency instability of  $1 \times 10^{-15}$  *Rev. Sci. Instrum.* **85** 113107
- [15] Ito I, Silva A, Nakamura T and Kobayashi Y 2017 Stable CW laser based on low thermal expansion ceramic cavity with  $4.9 \text{ mHz s}^{-1}$  frequency drift *Opt. Express* **25** 26020–8

## 6.8 Article: Europium hole-burning spectroscopy

The material presented in this chapter has been published as:

R. Oswald, M. G. Hansen, E. Wiens, A. Yu. Nevsky, and S. Schiller, “Characteristics of long-lived persistent spectral holes in  $\text{Eu}^{3+}:\text{Y}_2\text{SiO}_5$  at 1.2 K,” *Physical Review A*, volume 98, page 062516, issue 6, 2018. DOI: 10.1103/PhysRevA.98.062516. arXiv: 1811.08346 [physics.atom-ph]

### 6.8.1 Contributions of the various authors

I advised on the setup for the frequency measurement of the spectroscopy laser using the frequency comb. I also verified the performance of the frequency comb with respect to the environmental conditions in the laboratory. Eugen Wiens and I helped with the interpretation of fluctuations in the measured frequency. Alexander Nevsky and René Oswald built the setup and performed the measurements. René Oswald analyzed the data. Eugen Wiens programmed the control software, helped with cryogenic work and helped with frequency measurement. Stephan Schiller conceived the study, wrote most of the publication and supervised the work. All authors mentioned above contributed to the manuscript.

### 6.8.2 Copyright

Copyright 2018 by the American Physical Society

I have obtained permission from the publisher to reproduce this article in this thesis.



**Characteristics of long-lived persistent spectral holes in  $\text{Eu}^{3+}:\text{Y}_2\text{SiO}_5$  at 1.2 K**René Oswald, Michael G. Hansen, Eugen Wiens, Alexander Yu. Nevsky, and Stephan Schiller\*  
*Institut für Experimentalphysik, Heinrich-Heine-Universität Düsseldorf, 40225 Düsseldorf, Germany*

(Received 2 October 2018; published 21 December 2018)

Properties of persistent spectral holes (SHs) relevant for frequency metrology have been investigated in the system  $\text{Eu}^{3+}:\text{Y}_2\text{SiO}_5$  (0.5%) at crystallographic site 1 and a temperature of 1.2 K. Hole linewidths as small as 0.6 kHz have been reliably achieved. The theoretically predicted  $T^4$  dependence of the frequency shift with temperature has been confirmed with high precision. The thermal hysteresis of the SH frequency between 1.15 and 4.1 K was measured to be less than  $6 \times 10^{-3}$  fractionally. After initially burning a large ensemble of SHs, their properties were studied on long time scales by probing different subsets at different times. SHs could still be observed 49 days after burning if not interrogated in the meantime. During this time, the SH linewidth increased by 1.5 kHz, and the absorption contrast decreased from 35% to 15%. During a 14-day interval the absolute optical frequencies of previously unperturbed spectral holes were measured with respect to a Global-Positioning-System-monitored active H maser, using a femtosecond frequency comb. The fractional frequency drift rate exhibited an upper limit of  $2.3 \times 10^{-19} \text{ s}^{-1}$ , 65 times smaller than the most stringent previous limit.

DOI: [10.1103/PhysRevA.98.062516](https://doi.org/10.1103/PhysRevA.98.062516)**I. INTRODUCTION**

Recent progress in the performance of optical clocks, based on cold-atom ensembles or single ions [1–4], has become possible due to a strong improvement of the short-term frequency stability of the “clock” lasers that interrogate the atomic transitions [5,6]. Today’s clock lasers are realized by using macroscopic solid-state references, high-finesse optical cavities. Ultimately, the frequency stability of a clock laser corresponds to the stability of the cavity’s length. The latter is fundamentally limited by thermal noise and often also by vibrations induced by environmental noise. Nevertheless, excellent frequency instabilities have been reached, with the lowest values currently at  $4 \times 10^{-17}$  fractionally [7]. As of today, only very few approaches have been identified that have the potential of surpassing the resonator approach [8].

One solution is the use of persistent spectral holes in rare-earth-doped crystals at cryogenic temperatures. Here, a large ensemble of atomic ions ( $\sim 10^{20}$ ) is embedded in a crystalline host; on the order of  $10^{14}$  ions contribute to a single spectral hole (SH) and provide a narrow-linewidth frequency reference. This approach, suggested already more than two decades ago [9–13], combines advantageous features of atomic and macroscopic solid-state references.

The first report of frequency stabilization of a laser to an SH, using the Pound-Drever-Hall technique, dates back to 1999 [11]. A complication in this approach is that an SH is not a “static” reference but is modified dynamically by the interrogating laser field [14], a fact that must be taken into account in the experimental scheme. More recent work showed that SHs with narrow, kHz-level linewidths persist for times up to weeks with a high signal contrast [15]. In order to minimize the modification of the SHs by the laser radiation

to be stabilized, Cook *et al.* [16] have developed a technique that uses a pattern of hundreds of SHs for frequency stabilization. An excellent frequency instability at the  $1 \times 10^{-16}$  fractional level was thereby achieved for a 580-nm laser resonant with the  $F_0 \rightarrow D_0$  transition of the  $\text{Eu}^{3+}:\text{Y}_2\text{SiO}_5$  system at 580 nm. Recently, in the same system, a heterodyne detection technique for laser frequency locking to a single spectral hole was demonstrated [17]. Both techniques allow continuous (uninterrupted) frequency stabilization of a laser.

The long-term frequency stability of an SH on timescales of minutes and longer and therefore its utility for long-term frequency stabilization of lasers or for potential studies of fundamental physics depends also on systematic effects caused by external disturbances. Disturbances such as variations of temperature and of magnetic field, and also energy exchange on the atomic scale, result in SH frequency shift, SH contrast decrease and SH linewidth increase over time. These issues have been studied in detail in the system  $\text{Eu}^{3+}:\text{Y}_2\text{SiO}_5$  at 4 K [15,16,18] and at 3 K [19], including accurate determinations of the temperature dependence of the SH frequency. To minimize the influence of this latter effect, Thorpe *et al.* [15] implemented a compensation system making use of the dependence of SH frequency on gas pressure.

In laser frequency stabilization on long time intervals, an extreme case is the time scale of days and weeks after burning SHs. On this time scale the drift of the SH frequency and the modification of the SH line shape was first investigated in Ref. [19]. A drift consistent with  $0 (< 1.5 \times 10^{-17} \text{ s}^{-1})$  at  $1 \sigma$  level) was observed at 3 K, which was later confirmed in Ref. [20]. In this paper we extend the study of the long-term properties of persistent SHs to lower temperature, near 1.2 K. This is one of the lowest temperatures used so far in SH studies. One particular aspect of our approach was to probe the spectral holes cautiously. For example, SHs were left unperturbed spectrally for up to 49 days until interrogation occurred and then interrogated only once by a single absorption scan.

\*step.schiller@hhu.de; <http://www.exphy.uni-duesseldorf.de/>

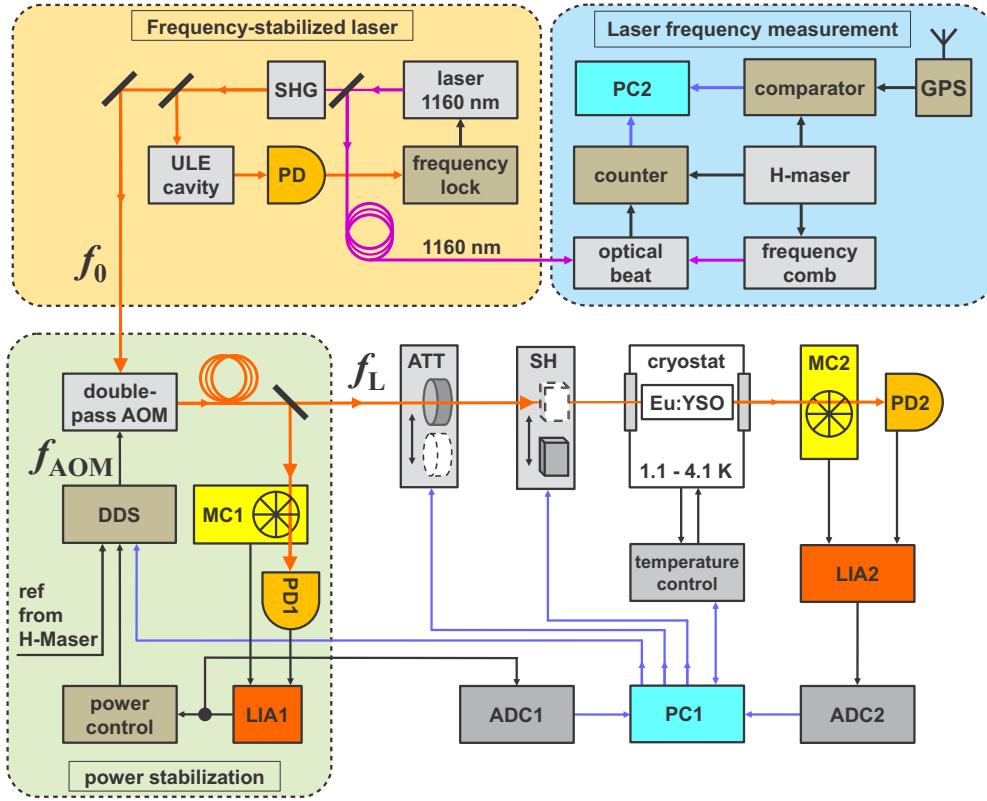


FIG. 1. Experimental setup. PD, photo detector; SHG, second harmonic generation; ULE, high-finesse ultralow thermal expansion glass optical cavity; AOM, acousto-optic modulator; DDS, direct digital synthesizer; MC, mechanical chopper; LIA, lock-in amplifier; ATT, attenuator; SH, shutter; ADC, analog-to-digital converter; and PC, personal computer.

## II. EXPERIMENT

Absorption spectroscopy experiments were carried out on the  ${}^7F_0 \rightarrow {}^5D_0$  transition of  $\text{Eu}^{+}$  ions of the crystallographic site 1 in a  $\text{Y}_2\text{SiO}_5$  host crystal [9], in the temperature range of 1.15 – 4.1 K. A schematic of the experimental setup is shown in Fig. 1.

The  $\text{Eu}^{+} : \text{Y}_2\text{SiO}_5$  crystal with 0.5% rare-earth ion concentration has dimensions of  $5 \times 5.5 \times 10 \text{ mm}^3$ , with the polished  $5 \times 5.5 \text{ mm}^2$  facets parallel to the  $D1$  and  $D2$  axes. The crystal was placed inside a ring-shaped rare-earth permanent magnet with a maximum magnetic field of approximately 0.8 T. The crystal and the magnet were mounted on a copper plate inside the cryostat. A closed-cycle pulse-tube cooler cryostat equipped with a Joule-Thomson stage was used for cooling. This allowed crystal temperatures as low as 1.15 K to be achieved.

For burning and interrogating SHs we used an external-cavity diode laser stabilized to a high-finesse ULE optical resonator. A description of this system, operating at 1156 nm, is given in Ref. [21]. In the present experiment, with the laser operating at 1160 nm, the linewidth was approximately 50 Hz. The radiation was frequency doubled to 580 nm, led to the cryostat using a 5-m-long polarization-maintaining optical fiber, and focused into the crystal using a fiber collimator. The beam diameter in the focus was  $300 \mu\text{m}$ . The light transmitted through the crystal was detected with a low-noise silicon

photodetector (PD2). A remotely controlled attenuator, based on a neutral density filter and a mechanical shutter were used to control the duration and laser power of the SH burning and read-out phases.

Before entering the cryostat, the laser light passed a beam splitter which deflected 30% of the radiation to a reference Si photodetector (PD1). Its signal was used for active stabilization of the laser power entering the crystal. To this end, an analog servo regulated the amplitude of the radio-frequency driver of an acousto-optic modulator (AOM). In addition, during the spectroscopy experiments, the output of PD1 was used for normalization of the value of the transmitted laser power, so as to reduce the influence of the laser power fluctuations on the measurements. The laser waves reaching the photodetectors PD1 and PD2 were modulated with chopper wheels (MC1 and MC2) at frequencies of 600 and 650 Hz, respectively. The photodetector signals were demodulated by respective lock-in amplifiers (LIA1 and LIA2). A typical lock-in integration time constant was 0.3 s. The output signals of both lock-in amplifiers were read out with a 10-bit analog-to-digital converter.

To tune the laser frequency, we used the AOM in a double-pass configuration driven by a computer-controlled DDS. It was referenced to a 10-MHz reference signal coming from an active hydrogen maser. The complete experiment including the DDS, the choppers, lock-in detectors, etc., was computer-

controlled with a LabVIEW program. The absolute frequency  $f_L$  of the wave interrogating the  $\text{Eu}^+$  ions at 580 nm is determined by the stabilized, but slowly drifting, laser frequency at 580 nm,  $f_0$ , plus the total frequency shift introduced by the AOM,  $f_L = f_0 + 2 f_{\text{AOM}}$ .

The laser frequency was measured at 1160 nm ( $f_0/2$ ) relative to the frequency of the active hydrogen maser, using a commercial erbium-doped fiber laser-based frequency comb (FC), optically stabilized to a home-built ULE-cavity-stabilized 1562-nm laser system by controlling the FC repetition rate. To this end, a fraction of the  $f_0/2$  laser radiation was led to the comb laboratory via a 150-m-long unstabilized fiber. The heterodyne beat signal of the laser with a comb mode was measured with a dead-time-free frequency counter. The laser frequency  $f_0/2$  was then evaluated in a conventional way from the beat frequency, the repetition rate, and the carrier envelope offset frequency. All respective counters were referenced to the maser. In addition, the maser's long-term frequency drift was monitored by a Global Positioning System (GPS) receiver.

### III. SPECTRAL HOLES

A basic investigation consisted of the determination of conditions under which the burning produced SHs of appreciable strength but still having a narrow linewidth. To this end, we measured the dependence of the SH linewidth and the SH contrast on the burn phase duration. We define the SH contrast as  $C_h = [S_{\text{PD2}}(\Delta = 0) - S_{\text{PD2}}(|\Delta| \gg \text{FWHM})]/S_{\text{PD2,max}}$ , where  $S_{\text{PD2}}(\Delta)$  is the laser power measured by the transmission detector PD2 for a given interrogation laser detuning from the SH line center,  $\Delta$ .  $S_{\text{PD2,max}}$  is the power detected on-resonance for a “deeply” burnt SH, the crystal then being essentially transparent. FWHM denotes the full width at half maximum.

Different sets of five SHs with a frequency spacing of 20 kHz were burned with a laser power of 1.7 nW for durations from 10 to 320 s. Spectroscopy of the holes was carried out by tuning the frequency  $f_L$  in steps of 100 Hz within a  $\pm 10$  kHz frequency range around the SH center frequencies with a dwell time of 0.7 s per frequency value. For these measurements the laser power was reduced to 0.86 nW. The transmission data taken during such scans were fitted with Lorentzians and the FWHM linewidth values were determined. The mean FWHM values of five-hole sets are presented in Fig. 2(a). The SH linewidth dependence on burn duration was found to be approximately linear, with a slope of  $s = 0.10$  kHz/min. For burn durations up to 150 s, the SH contrast [Fig. 2(b)] follows a linear dependence with a slope of 25%/min. At 320 s burn duration we observed a strong saturation effect.

We investigated the operational parameters for obtaining minimum SH linewidths. For example, we produced SHs with the same burn power level of 1.7 nW and a short burn time of 7 s. The parameters for the subsequent interrogation scan were optimized to obtain a high signal-to-noise ratio. The frequency of the interrogation wave was stepped in 100-Hz increments every 0.5 s. The SH spectra obtained are shown in Fig. 3. The mean FWHM linewidth is 0.61(7) kHz. This should be compared to the minimum possible value, the homogeneous

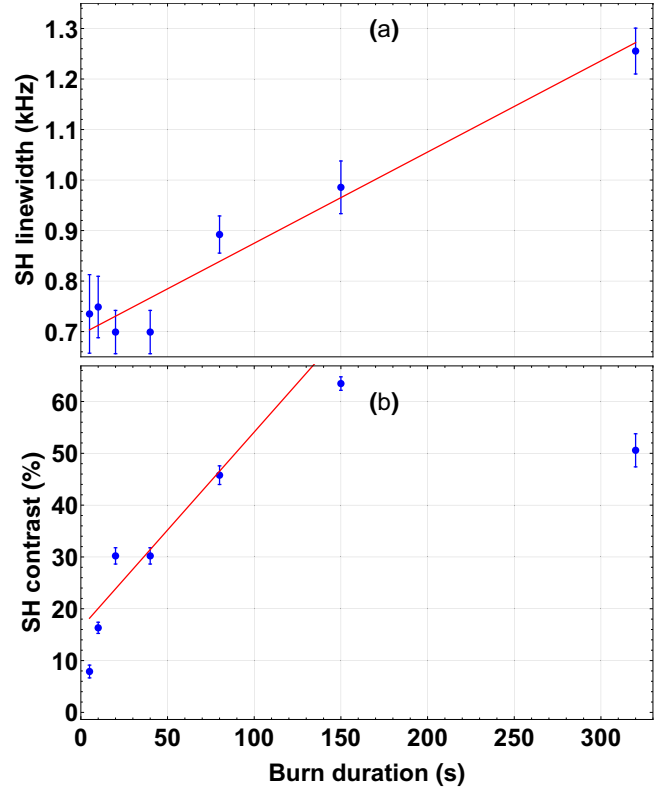


FIG. 2. (a) FWHM linewidths of spectral holes as a function of the burn time. Burn power is 1.7 nW; beam diameter is 300  $\mu\text{m}$ . (b) Contrast  $C_h$  of the SHs, for different burn times.

linewidth of the SHs,  $\Gamma_{\text{hom,min}} = 122$  Hz, derived from photon echo decay measurements [22,23]. We note that even for our comparatively low linewidth value, the signal contrast is still appreciable. For example, for the spectral hole 1 in Fig. 3, it was 15%. Further reduction of the burning laser power and of the interrogation time did not allow us to obtain narrower linewidths.

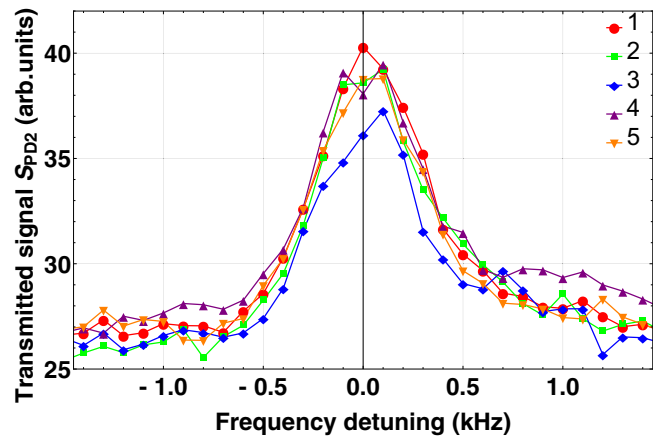


FIG. 3. Transmission signals of five different SHs exhibiting the smallest observed linewidths. The frequency scales for each hole were shifted so as to overlap the peaks. The measurement conditions are described in the text.

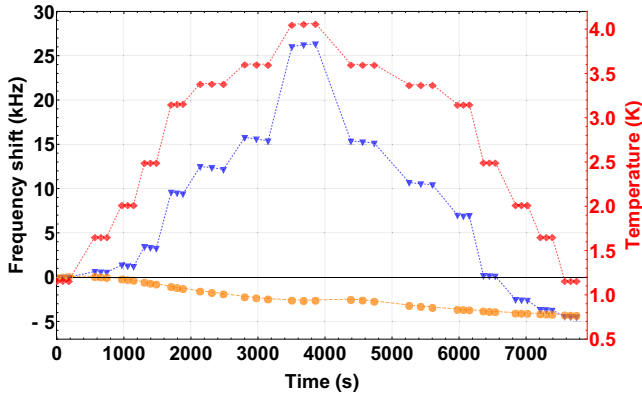


FIG. 4. Variation of the SH center frequencies as found from the AOM frequency shift  $2 \Delta f_{\text{AOM},j}(t)$  (blue triangles) as the crystal temperature (red diamonds) is increased from 1.15 to 4 K and cooled back again. The independently occurring drift of the frequency-doubled laser frequency,  $\Delta f_0(t)$ , is shown as orange circles. Each blue point corresponds to one scan over one SH.

#### IV. TEMPERATURE-INDUCED FREQUENCY SHIFTS AND THERMAL HYSTERESIS

The temperature-induced shift of the SH center frequency was measured previously by Könz *et al.* [24] in the range of 4 to 320 K for sites 1 and 2, and a discussion of the underlying physics was given. A precise measurement was performed by Chen *et al.* [19] in the range of 3 to 4 K for site 1 and by Thorpe *et al.* for sites 1 and 2 in the ranges 2.2 to 8.5 K [15] and 2.5 to 5.5 K [18]. In the present experiment we measured the site 1 shift in the range of 1.15 to 4.1 K. The determination of the shift at the lower end of this range is challenging, due to its drop-off according to an expected  $T^4$  dependence.

The frequency shift upon temperature cycling was studied by Chen *et al.* [19]. No effect was observed at the few kilohertz level. Here we set a more precise upper limit.

##### A. Procedures

After starting the laser frequency ( $f_0/2$ ) measurement, 66 SHs were burnt at 1.15 K, spaced by  $\delta f_L = 100$  kHz. The burning time was set to 2 s and the laser power to 26 nW. The hole-burning procedure had a total duration of about 8 min. During the burn phase the laser frequency exhibited a nonlinear drift. Its time dependence was therefore fitted by a nonlinear function. By this procedure we assigned a center frequency,  $f_{\text{SH},j}^{\text{burn}} = f_{\text{SH}}(t_j^{\text{burn}})$ , to every SH  $j$  created at a particular time,  $t_j^{\text{burn}}$ . The typical uncertainty was  $\sigma_{f_L, \text{burn}} = 60$  Hz.

Over the course of 1 h, the temperature was increased to 4.1 K in steps of several 0.1 K and afterwards decreased again (see Fig. 4, red diamonds). After each step, at constant temperature, three so far not interrogated SHs were scanned and the mean of their center frequencies was determined. For this SH spectroscopy, the laser power was reduced by a factor of 10 and the AOM frequency was changed in steps of 100 Hz with a dwell time of 0.7 s. The recorded data were fitted assuming a Lorentzian line shape, determining  $f_{\text{fit}}$ , and introducing an error  $\sigma_{\text{fit}}$  of about 10 Hz.

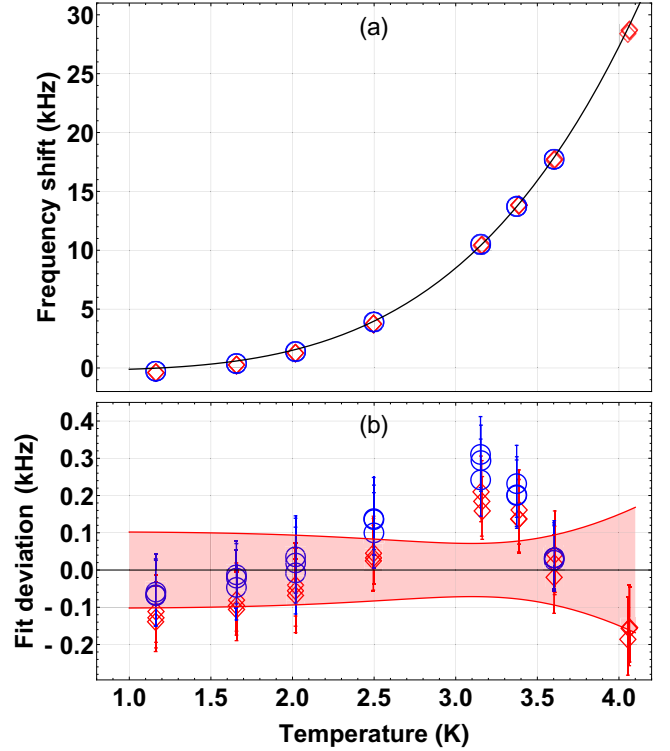


FIG. 5. Temperature dependence of the SH center frequencies for rising (red diamonds) and falling (blue circles) temperature. The black line in the upper graph is a fit to the model function  $A T^4 + B$ . Panel (b) shows the deviations from the fit and the  $\pm 1\sigma$  fit uncertainty interval.

The frequency of the laser during the spectroscopy was evaluated at the time instant when the SH center was reached, using a nonlinear fit as above. This resulted in the SH frequency  $f_{\text{SH},j}^{\text{scan}}$ . Its uncertainty arises from  $\sigma_{\text{fit}}$  and from the error of the FC measurement  $\sigma_{f_L, \text{scan}}$ . Finally, the frequency shift of an SH  $j$  is  $\Delta f_{\text{SH},j} = f_{\text{SH},j}^{\text{scan}} - f_{\text{SH},j}^{\text{burn}}$ . We assigned to it the uncertainty  $\sigma_{\text{shift}} = \sqrt{\sigma_{f_L, \text{burn}}^2 + \sigma_{f_L, \text{scan}}^2 + \sigma_{\text{fit}}^2}$ . A typical value was 90 Hz.

An overview of the recorded data is presented in Fig. 4. As a function of time it shows the temperature measured at the crystal, the drift of the frequency-doubled laser frequency  $\Delta f_0(t)$  and  $2 \Delta f_{\text{AOM},j}(t)$ , the difference of the frequency offsets produced by the AOM at the observation time  $t$  and at the burning time.

##### B. Thermal frequency shift

The frequency shift data are shown as a function of temperature in Fig. 5(a). A theoretical model of the SH shift predicts a  $T^4$  dependence, caused by a two-phonon Raman process affecting the impurity ions [9,24,25]. Our data were therefore fitted with the function  $A T^4 + B$ . This resulted in an accurate description of the data, and small residuals, see Figs. 5(a) and 5(b), with  $A = 108(0.3)$  Hz/K<sup>4</sup> and  $B = -216(37)$  Hz. Note that because of the small hysteresis (see Sec. IV C) we take into account the data for both rising and falling temperatures. In the work of Könz *et al.* [24] a value of  $A' = 166(10)$  Hz/K<sup>4</sup>



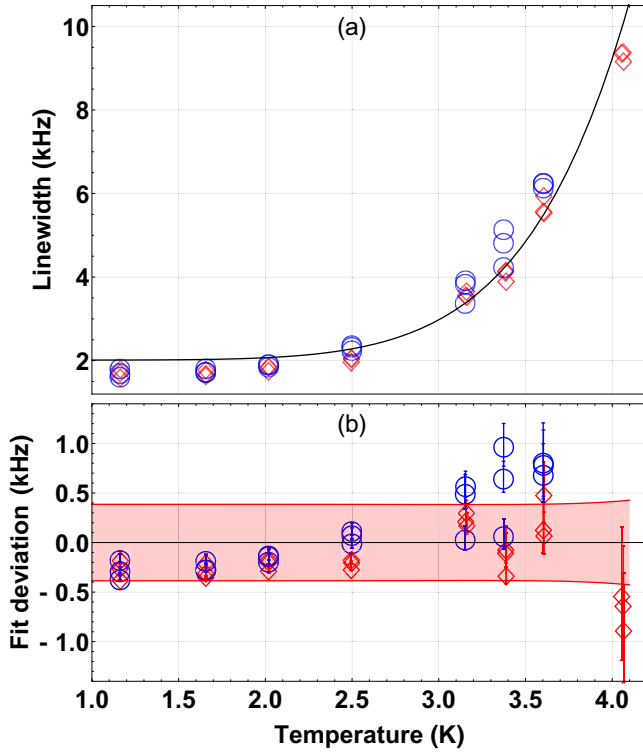


FIG. 6. Temperature dependence of the SH linewidth for rising (red diamonds) and falling (blue circles) temperature. The black line in panel (a) is a fit to the model function  $CT^7 + D$ . Panel (b) shows the deviations from the fit and the  $\pm 1\sigma$  fit uncertainty interval.

has been found for the temperature-induced shift of site 1-ions. However, only values above 70 K were considered in the determination of the coefficient.

Our coefficient  $A$  also differs from the value  $76(15) \text{ Hz/K}^4$  (for site 1) measured previously by Thorpe *et al.* [18]. As shown in that work the application of external pressure on the crystal through helium gas induces a linear frequency shift countering the effect of the temperature-induced frequency shift. This could explain the lower coefficient. Figure 6 shows the temperature dependence of the SH linewidth. The theoretical model [24,25] predicts a dependence of the type  $CT^7 + D$ . A fit of this function to our data yields  $C = 0.44(2) \text{ Hz/K}^7$ .

The value differs significantly from the value found by Könz *et al.* [24],  $7.2 \times 10^{-4} \text{ Hz/K}^7$ . However, their value was obtained from photon-echo-decay measurements. That method differs from our method: the photon echoes were measured on a timescale of microseconds, whereas our measurements were on the timescale of minutes (the typical duration of a frequency scan over a SH linewidth).

### C. Thermal hysteresis

In Fig. 4 the AOM-induced frequency shift and the independently measured laser frequency drift rejoin at the end of the temperature cycle. Correspondingly, the red and blue data points at  $T = 1.15 \text{ K}$  in Fig. 5(a,b) nearly coincide. This shows that the thermal hysteresis of the SH frequencies is very small. More precisely, the residual shift upon returning

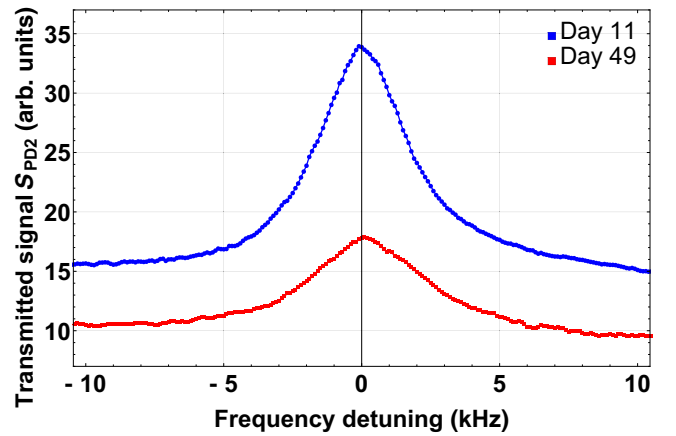


FIG. 7. Typical spectral holes observed during the long-term drift measurement. The upper blue points show a scan of a spectral hole 11 days after burning. The lower red points show another SH scanned 49 days after burning. In order to illustrate the typical deformation of the SHs, the respective frequency scales were shifted so as to center the peaks.

to the initial temperature was  $\delta f_{\text{hyst}} = 59 \text{ Hz}$ , which is within the measurement error  $\sigma_{\text{shift}}$ . Relating the sum of  $\delta f_{\text{hyst}}$  and  $\sigma_{\text{shift}}$  to the maximum frequency shift of 27 kHz at  $T = 4 \text{ K}$  allows us to state an upper limit of  $6 \times 10^{-3}$  for the fractional hysteresis.

## V. LONG-TERM FREQUENCY DRIFT MEASUREMENT

### A. Properties of long-lived spectral holes

In order to probe in a careful way the intrinsic long-term stability of the frequency of persistent SHs, we modified the experimental protocol compared to our previous work [19] in two significant aspects: (i) operation at significantly lower temperature, 1.15 K, and (ii) not performing multiple read-outs of the same SH. Our procedure consisted of initially burning a sufficiently large “reservoir” of 200 SHs with a frequency spacing of  $\delta f_L = 200 \text{ kHz}$ . The burn duration was set to 2 s with a relatively high laser power of 86 nW. The hole-burning procedure had a total duration of about 15 min. For the SH spectroscopy, the laser power was reduced by a factor of 10 and the AOM frequency was changed in steps of 100 Hz with a dwell time of 0.7 s per frequency value.

A typical line scan obtained under such conditions is shown in Fig. 7. During the scan the laser frequency was measured by the FC. The determination of the SH frequency shift  $\Delta f_{\text{SH},j}$  from  $f_{\text{SH},j}^{\text{scan}}$ ,  $f_{\text{SH},j}^{\text{burn}}$  and the measurement errors  $\sigma_{f_L, \text{burn}}$ ,  $\sigma_{f_L, \text{scan}}$ , and  $\sigma_{\text{fit}}$  were obtained in the same fashion as described in Sec. IV.

Several times per week, over a period of 49 days, a subset of new (previously not interrogated) SHs was scanned. At the same time, the laser frequency was measured with the FC. Figure 8 shows an example of the result obtained on a particular day. The long-term variations of the SHs linewidths and contrasts are presented in Fig. 9. After 49 days we observed an increase of the linewidth by about 35%. The  $1/e$  SH lifetime, extrapolated from the contrast decrease, is 50

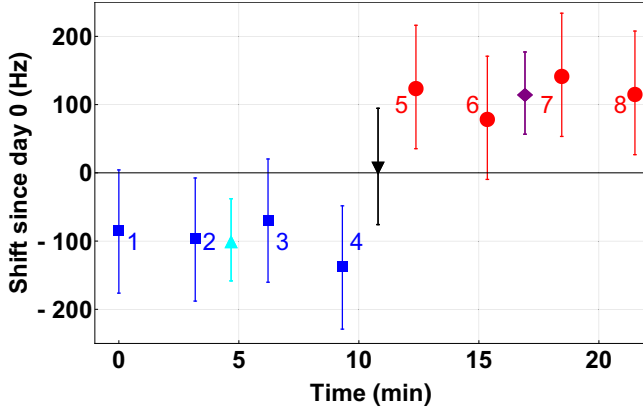


FIG. 8. Determination of the mean SH frequency  $f_{\text{shift}}(t)$  (black down-pointing triangle) on day 18 of the long-term measurement. Four SHs ( $j = 1$  to 4, blue squares) were scanned once with decreasing frequency and another set ( $j = 5$  to 8, red circles) was scanned once with increasing AOM frequency. The mean value of the “decreasing” scans  $\langle \Delta f_{\text{SH},j} \rangle_{\text{dec}}$  is shown as a cyan up-pointing triangle, and the mean value of the “increasing” scans  $\langle \Delta f_{\text{SH},j} \rangle_{\text{inc}}$  is shown as a purple diamond.

days. This value is consistent with that of Könz *et al.* [24] who measured a value  $\simeq 23$  days at 2 K for site 1.

### B. Long-term frequency drift

A systematic frequency shift occurs when determining the SH center frequency: the latter depends on the sign of the

frequency steps introduced by the AOM during the line scan. We measured this effect precisely for the abovementioned settings by burning 20 SHs within 2 min and scanning them 2 to 18 min later. One half of the SHs was scanned by increasing  $f_{\text{AOM}}$ ; the other half was scanned in reverse. We measured a difference of 298(47) Hz between the average center frequencies  $\langle \Delta f_{\text{SH},j} \rangle$  of the two subsets. Therefore, in our long-term measurements, we determined the frequency shifts as follows. At a particular (nominal) time  $t$ , we measured, within approximately half an hour, the mean SH center frequency  $\langle \Delta f_{\text{SH},j} \rangle_{\text{inc}}$  of a set of at least 4 SHs scanned with rising AOM frequency and the mean frequency  $\langle \Delta f_{\text{SH},j} \rangle_{\text{dec}}$  of another set of at least 4 SHs with falling frequency. The average frequency shift  $f_{\text{shift}}(t)$  of the SHs at time  $t$  is defined as the mean of  $\langle \Delta f_{\text{SH},j} \rangle_{\text{dec}}$  and  $\langle \Delta f_{\text{SH},j} \rangle_{\text{inc}}$ . An example of such a determination is shown in Fig. 8.

The complete measurement lasting 2 weeks is shown in Fig. 10. A linear fit of the data shows a fractional SH frequency drift of  $1.3(10) \times 10^{-19}/\text{s}$ , where the uncertainty is statistical. This is consistent with a vanishing drift rate. The statistical uncertainty originates from the three contributions already discussed in Sec. IV A, which resulted in  $\sigma_{\text{shift}} \simeq 90$  Hz for an individual measurement  $\Delta f_{\text{SH},j}$ .

A systematic effect is a frequency shift due to long-term temperature drift. The temperature increased monotonically by 15 mK during the measurement period [see Fig. 10(b)]. Taking into account the measured temperature sensitivity (see Sec. IV) the resulting total SH frequency shift is 10 Hz, which is not negligible. Therefore, the data shown in Fig. 10(a) were corrected for the respective calculated thermal shift.

A further possible systematic error is a drift of our frequency reference, the hydrogen maser. A comparison of its

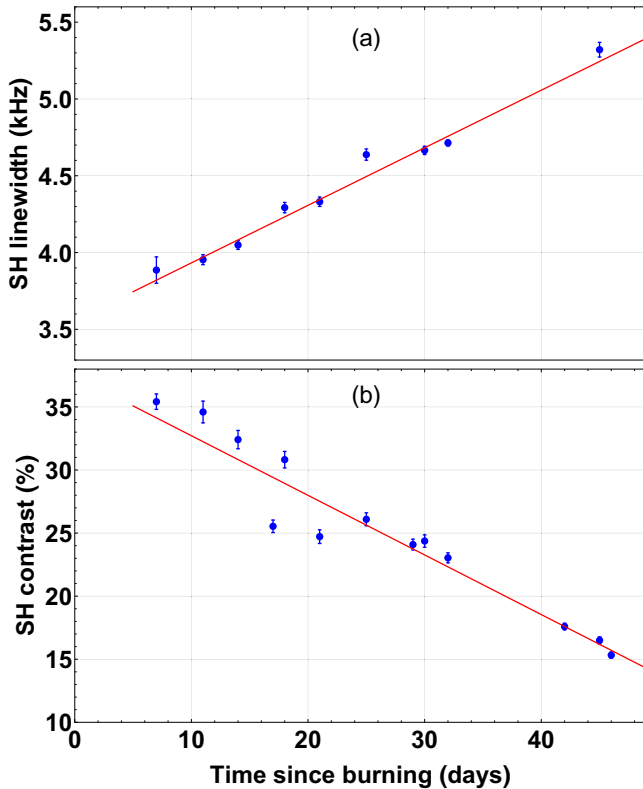


FIG. 9. Long-term variation (a) of the SH linewidth (FWHM) and (b) of the SH contrast  $C_h$ . Each SH was scanned only once.

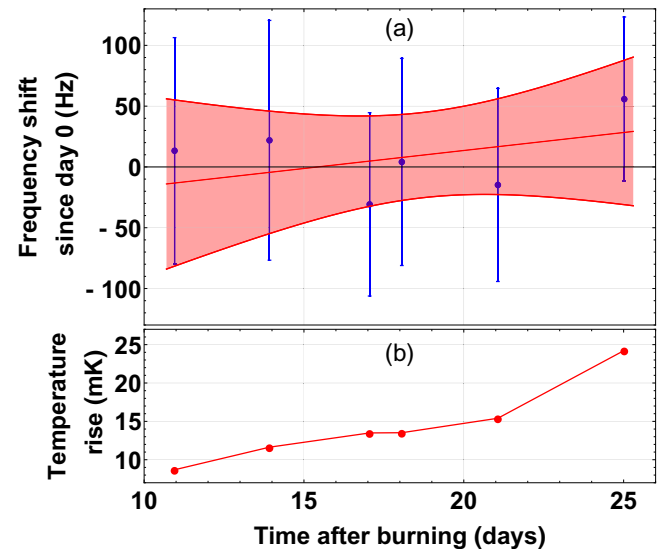


FIG. 10. (a) The change in SH frequency,  $f_{\text{shift}}(t)$ , measured over a period of 14 days. All SHs were burned at time  $t = 0$ . Red line: linear fit with slope 3(7) Hz/day, or  $1.3(10) \times 10^{-19} \text{ s}^{-1}$  fractionally. The shaded region shows the  $\pm 1\sigma$  uncertainty of the fit. (b) Temperature measured at the location of the  $\text{Eu}^{3+} : \text{Y}_2\text{SiO}_5$  crystal. A calibrated Cernox temperature sensor having a specified accuracy of 5 mK was used.

frequency with the 1 pulse per second signal received from the GPS showed that the maser frequency drift during the measurement period was on the order of  $1 \times 10^{-20}/\text{s}$  and can thus be neglected.

## VI. SUMMARY AND CONCLUSION

We measured with high frequency resolution and high accuracy the linewidth, the long-term frequency drift, and the temperature-induced frequency shift and line broadening of persistent spectral holes in  $\text{Eu}^+ : \text{Y}_2\text{SiO}_5$  at a temperature significantly lower than previously, 1.15 K. Our measurements demonstrated a significant increase of the SH lifetime in comparison to results at 3–4 K [16,19], confirming the estimations [24]. We determined the properties of spectral holes as long as 49 days after burning and found that even at that “age,” the holes still exhibited good signal-to-noise ratio and a reasonably small linewidth (5.4 kHz), if previously left undisturbed. No long-term drift of the SH center frequencies over 14 days could be observed, with a  $1\sigma$  upper limit of  $2.3 \times 10^{-19}/\text{s}$ . This is 65 times smaller than the upper limit measured in a previous experiment at 3 K,  $1.5 \times 10^{-17}/\text{s}$  [19]. For comparison, cryogenic silicon cavities with drifts as small as  $5 \times 10^{-19}/\text{s}$  to  $1.4 \times 10^{-20}/\text{s}$  have been reported [26,27]. We expect that it is feasible to reduce the uncertainty of the spectral hole drift by increasing the observation time interval, which in our case was limited because of cryostat performance. A measurement of the temperature-induced hole

line shift over the range 1.2–4.1 K accurately confirmed the predicted variation with the fourth power of the temperature. No hysteresis in the hole frequency was found within the measurement error after heating the crystal from 1.15 to 4.1 K and cooling back to 1.15 K.

The long-term properties of spectral holes in this particular system do appear to make it suitable as a long-term-stable frequency reference. In particular, it is favorable that at 1.15 K the temperature sensitivity is only  $\simeq 1 \times 10^{-12}/\text{K}$  fractionally. This is comparable to the lowest values achieved with cryogenic silicon cavities [27]. If required for achieving the most demanding performance, an active temperature stabilization of the host crystal to the microkelvin level could be implemented [19] and this could reduce the effects of temperature instability to the  $10^{-18}$  level.

The SH linewidth observed in this work is also comparable to that of silicon cavities [27]. The signal-to-noise ratio of the spectral hole signals is, of course, significantly lower than that for a cavity. It could be increased, e.g., by using longer crystals, interrogating several crystals in parallel, and increasing the europium concentration.

## ACKNOWLEDGMENTS

The authors thank D. Iwaschko for his technical assistance. R.O. and E.W. acknowledge a fellowship from the Professor-W.-Behmenburg-Schenkung. This work was performed in the framework of Project No. Schi 431/15-1 of the Deutsche Forschungsgemeinschaft.

- 
- [1] A. Derevianko and H. Katori, *Rev. Mod. Phys.* **83**, 331 (2011).
  - [2] N. Poli, C. W. Oates, P. Gill, and G. M. Tino, *Riv. Nuovo Cimento* **36**, 555 (2013).
  - [3] A. D. Ludlow, M. M. Boyd, J. Ye, E. Peik, and P. O. Schmidt, *Rev. Mod. Phys.* **87**, 637 (2015).
  - [4] F.-L. Hong, *Meas. Sci. Technol.* **28**, 012002 (2017).
  - [5] T. Kessler, C. Hagemann, C. Grebing, T. Legero, U. Sterr, F. Riehle, M. J. Martin, L. Chen, and J. Ye, *Nat. Photonics* **6**, 687 (2012).
  - [6] S. Häfner, S. Falke, C. Grebing, S. Vogt, T. Legero, M. Merimaa, C. Lisdat, and U. Sterr, *Opt. Lett.* **40**, 2112 (2015).
  - [7] D. G. Matei, T. Legero, S. Häfner, C. Grebing, R. Weyrich, W. Zhang, L. Sonderhouse, J. M. Robinson, J. Ye, F. Riehle, and U. Sterr, *Phys. Rev. Lett.* **118**, 263202 (2017).
  - [8] D. Meiser, J. Ye, D. R. Carlson, and M. J. Holland, *Phys. Rev. Lett.* **102**, 163601 (2009).
  - [9] R. M. Macfarlane and R. M. Shelby, in *Spectroscopy of Crystals Containing Rare Earth Ions*, Vol. 21 (North-Holland, Amsterdam, 1987), Chap. 3.
  - [10] M. J. Sellars, R. S. Meltzer, P. T. H. Fisk, and N. B. Manson, *J. Opt. Soc. Am. B* **11**, 1468 (1994).
  - [11] P. B. Sellin, N. M. Strickland, J. L. Carlsten, and R. L. Cone, *Opt. Lett.* **24**, 1038 (1999).
  - [12] P. B. Sellin, N. M. Strickland, T. Böttger, J. L. Carlsten, and R. L. Cone, *Phys. Rev. B* **63**, 155111 (2001).
  - [13] G. J. Pryde, T. Böttger, R. L. Cone, and R. C. C. Ward, *J. Lumin.* **98**, 309 (2002).
  - [14] B. Julsgaard, A. Walther, S. Kröll, and L. Rippe, *Opt. Express* **15**, 11444 (2007).
  - [15] M. Thorpe, L. Rippe, T. Fortier, M. Kirchner, and T. Rosenband, *Nat. Photonics* **5**, 688 (2011).
  - [16] S. Cook, T. Rosenband, and D. R. Leibbrandt, *Phys. Rev. Lett.* **114**, 253902 (2015).
  - [17] O. Gobron, K. Jung, N. Galland, K. Predehl, R. L. Targat, A. Ferrier, P. Goldner, S. Seidelin, and Y. L. Coq, *Opt. Express* **25**, 15539 (2017).
  - [18] M. J. Thorpe, D. R. Leibbrandt, and T. Rosenband, *New J. Phys.* **15**, 033006 (2013).
  - [19] Q.-F. Chen, A. Troshyn, I. Ernsting, S. Kayser, S. Vasilyev, A. Nevsky, and S. Schiller, *Phys. Rev. Lett.* **107**, 223202 (2011).
  - [20] D. R. Leibbrandt, M. J. Thorpe, C.-W. Chou, T. M. Fortier, S. A. Diddams, and T. Rosenband, *Phys. Rev. Lett.* **111**, 237402 (2013).
  - [21] S. Vogt, C. Lisdat, T. Legero, U. Sterr, I. Ernsting, A. Nevsky, and S. Schiller, *Appl. Phys. B* **104**, 741 (2011).
  - [22] R. Yano, M. Mitsunaga, and N. Uesugi, *Opt. Lett.* **16**, 1884 (1991).
  - [23] R. W. Equall, Y. Sun, R. L. Cone, and R. M. Macfarlane, *Phys. Rev. Lett.* **72**, 2179 (1994).

- [24] F. Könz, Y. Sun, C. W. Thiel, R. L. Cone, R. W. Equall, R. L. Hutcheson, and R. M. Macfarlane, [Phys. Rev. B](#) **68**, 085109 (2003).
- [25] D. E. McCumber and M. D. Sturge, [J. Appl. Phys.](#) **34**, 1682 (1963).
- [26] C. Hagemann, C. Grebing, C. Lisdat, S. Falke, T. Legero, U. Sterr, F. Riehle, M. J. Martin, and J. Ye, [Opt. Lett.](#) **39**, 5102 (2014).
- [27] E. Wiens, A. Yu. Nevsky, and S. Schiller, [Phys. Rev. Lett.](#) **117**, 271102 (2016).



## 6.9 Article: High-resolution ro-vibrational spectroscopy of $\text{HD}^+$

The material presented in this chapter has been published as:

I. V. Kortunov, S. Alighanbari, M. G. Hansen, G. S. Giri, V. I. Korobov, and S. Schiller, “Proton–electron mass ratio by high-resolution optical spectroscopy of ion ensembles in the resolved-carrier regime,” *Nature Physics*, 2021. DOI: 10.1038/s41567-020-01150-7. arXiv: 2103.11741 [quant-ph]

### 6.9.1 Contributions of the various authors

Together with Ivan Kortunov, I set up and characterized the spectroscopic sources, as described in section 3.3.2 on page 31. I also contributed parts of the control software used for the frequency metrology of these lasers. Gouri Giri and Soroosh Alighanbari operated the ion trap and Ivan Kortunov operated the lasers during the measurements. The theoretical calculations were performed by Vladimir Korobov, Ivan Kortunov and Stephan Schiller. Stephan Schiller conceived the study, wrote the manuscript and supervised the work. All authors mentioned above contributed to the manuscript.

### 6.9.2 Copyright

Unfortunately, due to copyright restrictions, the final, peer-reviewed version of the article can not be reproduced in this thesis. The interested reader is advised to obtain the final version from the journal or to obtain the pre-print version from [arxiv.org](https://arxiv.org), as linked to in the above citation.

## 7 Outlook

In rotational spectroscopy, better resolution has already been obtained by my colleagues using the same source that I characterized, leading to even better agreements between theory and experiments [10]. However, the resolution set by the linewidth of the THz source according to equation 13 is still not fully exploited, thus an improvement of at least one order of magnitude in terms of resolution should be possible. In order to lower the linewidths of the transitions even further, the intensity of the spectroscopy radiation has to be lowered further. This may result in a poor signal-to-noise ratio, requiring even longer measurement cycles. An upcoming solution to this problem is hyperfine state selective optical state preparation using a second THz source, experiments on which are soon to begin.

Spectroscopy on  $\text{HD}^+$  will be complemented by spectroscopy on  $\text{H}_2^+$ . This will allow the determination of more physical constants by combining the results of both species, allowing some constants to cancel out. A laser source for these measurements is currently in the process of being absolutely frequency stabilized.

Spectroscopy using the lasers set up for the new difference frequency generation source will continue in the new ion trap, which is currently under development. In this trap, the Lamb-Dicke regime should also be reachable for overtone-transitions near  $1\text{ }\mu\text{m}$ , allowing a five-fold improvement in fractional resolution even without improvements on the linewidths of the lasers.

The versatility of the difference-frequency generation sources may be increased by GaAs or GaSb waveguides [115, 116], providing a higher conversion efficiency for mid-IR generation than the currently employed PPLN modules.

With increased spectroscopic precision being reached, tests for the constancy of  $m_e/m_p$  may become feasible soon, possibly even optical clocks based on  $\text{HD}^+$  [117, 118].

Limitations on the achievable linewidth and frequency accuracy of the spectroscopy lasers are also currently set by the remaining phase noise of the carrier-envelope frequency stabilization of the frequency comb. A next-generation frequency comb, which I participated in selected and specifying, has meanwhile arrived. It provides a much cleaner comb spectrum both for measurements as well as linewidth-narrowing of spectroscopy lasers [119–121]. First promising spectroscopic results have been obtained, and the comb alone has allowed to improve the observed linewidth of the transition by a factor of two.

After a promising characterization of the NEXCERA material, a larger cavity was ordered and is used to construct a new clock laser for the SOC2 Strontium based optical clock [122]. The clock laser is being characterized, especially in terms of vibration sensitivity of the cavity, using the new frequency comb. Three-Cornered-Hat measurements [123] against other newly-developed cavities are soon to start.

My colleagues have advanced the spectral-hole burning system using a new locking technique, which allows them to stabilize a laser to spectral holes for more than two hours. A publication about this new technique has been submitted by them.

## A Appendix

### A.1 Tabular values of figures

Year	Publication	System	Relative uncertainty
1969	Jefferts1969 [124]	H <sub>2</sub> <sup>+</sup>	$1.2 \times 10^{-6}$
1976	Wing1976 [125]	HD <sup>+</sup>	$1.0 \times 10^{-6}$
1977	Spezeski1977 [126]	HD <sup>+</sup>	$3.8 \times 10^{-7}$
1992	Balakrishnan1992 [127]	H <sub>2</sub> <sup>+</sup>	$3.7 \times 10^{-6}$
1993	Carrington1993 [128]	HD <sup>+</sup>	$3.3 \times 10^{-6}$
2004	Zhang2004 [129]	H <sub>2</sub> <sup>+</sup>	$6.5 \times 10^{-7}$
2007	Koelemeij2007 [62]	HD <sup>+</sup>	$2.6 \times 10^{-9}$
2012	Bressel2012 [61]	HD <sup>+</sup>	$1.1 \times 10^{-9}$
2016	Biesheuvel2016 [130]	HD <sup>+</sup>	$1.1 \times 10^{-9}$
2018	Alighanbari2018 [77]	HD <sup>+</sup>	$3.8 \times 10^{-10}$
2020	Alighanbari2020 [10]	HD <sup>+</sup>	$1.3 \times 10^{-11}$
2020	Patra2020 [12]	HD <sup>+</sup>	$2.9 \times 10^{-12}$
2021	Kortunov2021 [109]	HD <sup>+</sup>	$3.3 \times 10^{-12}$

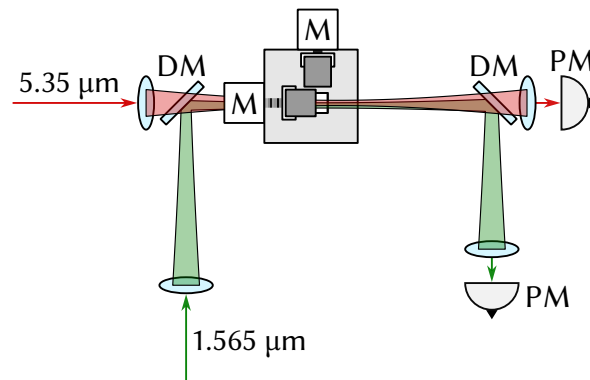
**Table A.1:** Tabular listing of measurement results shown in figure 1.1. List of references partially obtained from [131, figure 3, 132, figure 1.39].

Year	Publication	$m_p$	$m_e$	$m_p/m_e$
1969	CODATA1969 [133]	$8.0 \times 10^{-8}$	$6.2 \times 10^{-6}$	$6.2 \times 10^{-6}$
1973	CODATA1973 [13]	$1.1 \times 10^{-8}$	$3.8 \times 10^{-7}$	$3.8 \times 10^{-7}$
1978	Gaertner1978 [134]			$2.9 \times 10^{-6}$
1980	Graeff1980 [135]			$6.0 \times 10^{-7}$
1981	VanDyck1981 [136]			$1.4 \times 10^{-7}$
1983	Wineland1983 [137]			$3.4 \times 10^{-7}$
1985	VanDyck1985 [138]			$4.1 \times 10^{-8}$
1986	CODATA1986 [14]	$1.2 \times 10^{-8}$	$2.3 \times 10^{-8}$	$2.0 \times 10^{-8}$
1990	Gabrielse1990 [139]			$4.8 \times 10^{-8}$
1993	Audi1993 [140]	$6.0 \times 10^{-10}$		
1995	Farnham1995 [21]		$2.2 \times 10^{-9}$	
1998	CODATA1998 [15]	$1.3 \times 10^{-10}$	$2.1 \times 10^{-9}$	$2.1 \times 10^{-9}$
2001	Beier2001 [141]		$7.3 \times 10^{-10}$	
2002	CODATA2002 [16]	$1.3 \times 10^{-10}$	$4.4 \times 10^{-10}$	$4.6 \times 10^{-10}$
2004	Verdu2004 [142]		$7.3 \times 10^{-10}$	
2006	Hori2006 [143]			$1.3 \times 10^{-9}$
2006	CODATA2006 [144]	$1.0 \times 10^{-10}$	$4.2 \times 10^{-10}$	$4.3 \times 10^{-10}$
2010	CODATA2010 [18]	$8.9 \times 10^{-11}$	$4.0 \times 10^{-10}$	$4.1 \times 10^{-10}$
2011	Hori2011 [20]			$1.3 \times 10^{-9}$
2014	Sturm2014 [11]		$3.0 \times 10^{-11}$	
2014	CODATA2014 [1]	$9.0 \times 10^{-11}$	$2.9 \times 10^{-11}$	$9.5 \times 10^{-11}$
2016	Biesheuvel2016 [130]			$2.9 \times 10^{-9}$
2018	CODATA2018 [2]	$5.3 \times 10^{-11}$	$2.9 \times 10^{-11}$	$6.0 \times 10^{-11}$
2018	Alighanbari2018 [77]	$1.3 \times 10^{-9}$		
2019	Heiße2019 [112]	$3.3 \times 10^{-11}$		
2020	Alighanbari2020 [10]			$2.0 \times 10^{-11}$
2020	Patra2020 [12]			$2.1 \times 10^{-11}$
2021	Kortunov2021 [109]			$3.5 \times 10^{-11}$

**Table A.2:** Tabular listing of the data shown in figure 1.2. List of references extended from [145, page 16, fig. 1.6], [130, page 5, figure 5], [12]. Note that some of the references [11, 21, 112, 141] also state improved uncertainties for the ratios  $m_p/m_e$ , but rely on other published values for one of the two constants. Those have been omitted for clarity of the directly determined constants.

## A.2 Beam analyzer for beam overlap for SFG

For successful sum-frequency generation in a non-linear optical crystal, good beam overlap is crucial. Not only do the beams have to be collinear, but also their focus points should overlap in order to obtain the highest intensities for the non-linear process. At the time when the sum-frequency system with the quantum-cascade laser was initially set up, suitable beam analysis cameras covering the mid-IR were very expensive. Also, due to the high intensities in the focus points, there was the risk of damaging them.

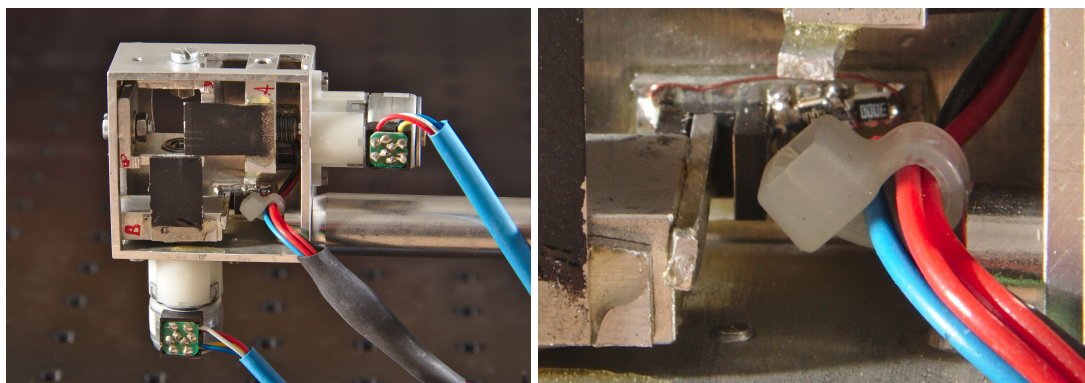


**Figure A.1:** Beam analysis for SFG-setup.

An alternative to beam-analysis with a camera is the knife-edge method. Since for a good overlap analysis the measurement process has to be performed many times, an beam analyzer based on automatic movement of the knife edges was conceived. The beam analysis setup is shown in figure A.1. The radiation of the QCL and the fiber laser is individually focused and then overlapped using a microic mirror. Behind the space for the crystal, the beams are again split using a microic mirror and are each sent onto a suitable power detector head. In order to reduce the amount of 1.5  $\mu\text{m}$  light on the QCL detector, two dichroic mirrors, which reflect the 1.5  $\mu\text{m}$  radiation are used in series. The beam analyzer is then placed between the two mirrors and measurements are performed along the beam axes. Since the two beams are detected by individual detectors, their spatial distribution and overlap can be determined in a single scan of the beam analyzer. The QCL is run at its nominal power, while the fiber laser is running at reduced power. Otherwise, it would destroy the blades. Care must be taken to run the system slow enough such that the thermal power meter used to detect the QCL power can accurately track the power changes. Here, a delay between movement of the blade and the measurement readout of 6 s was used.

The beam analyzer itself is shown in the right-hand side of figure A.2. The blades are each glued onto a block with an M6 thread. Two 1000 steps/revolution step motors (SPG1518M0504-102, Nanotec) each turn an M6 rod. The blocks with the blades are mounted such that when the rods turn, they are moved along the rods in axial direction. The motors are controlled via a motor driver (A4983, Allegro MicroSystems). The computer interface is realized using a microcontroller (Atmega8, Atmel) with a separate USB-to-serial converter.

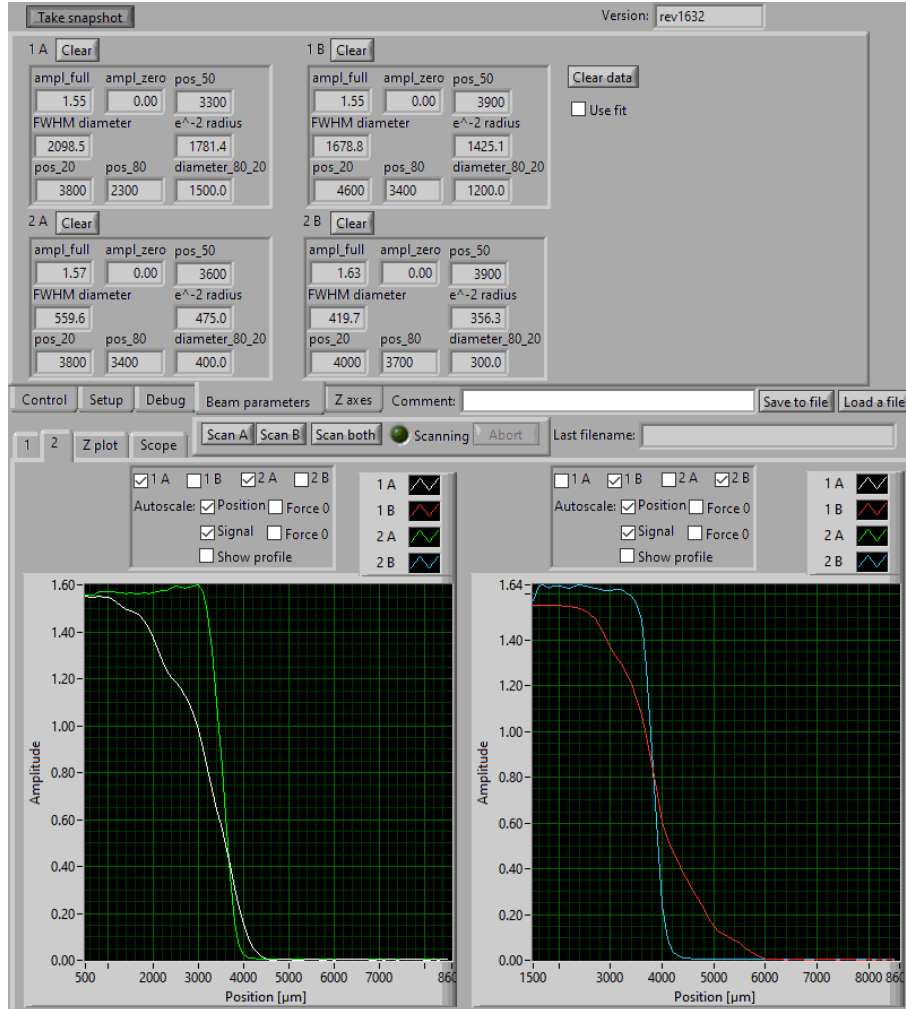
In order to help homing the blades, a light barrier detects when a rod glued onto the blade holders blocks it. During homing, the blades are moved in the direction of the light barrier until it detects the rod. Since the stepper motors resolution is based on the usage of gears, care has to be taken to reduce their hysteresis. To this end, at the beginning of each measurement the blade blocks are moved a good amount further beyond the point where they block the light barrier and then moved back until the light barrier is no longer blocked, such that the gears are “under tension” in the right movement direction.



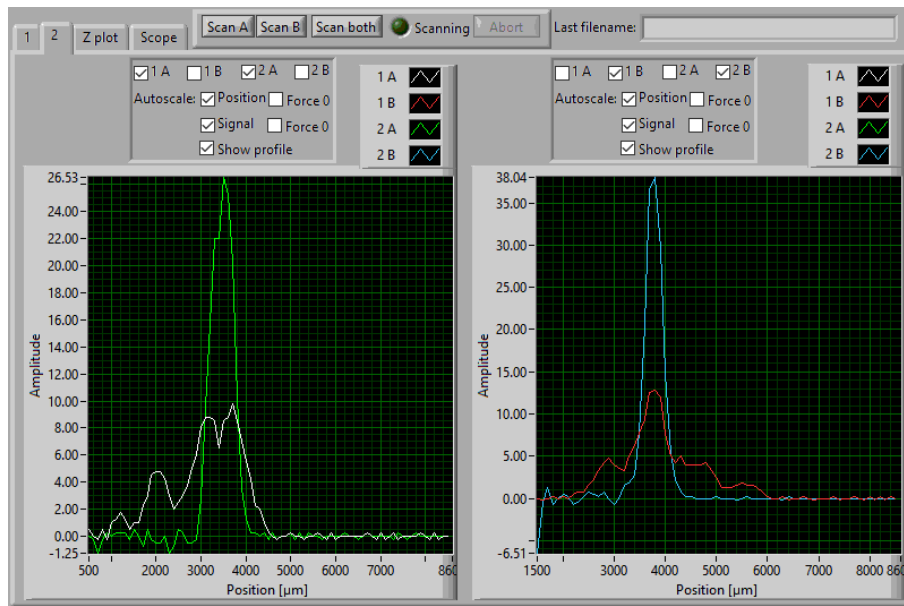
**Figure A.2:** Left: Photo of the beam analyzer. The blades are coated in black. “Scratches” from high-intensity laser beams can be seen on the blades. The blade moving in horizontal direction is labeled A, while the blade moving in the vertical direction is labeled B. Blade B is currently in the home position. Blade A has been moved into the beam. Right: Detailed view of the homing mechanism: A rod extends down into a light barrier.

The control software shown in figure A.3. It allows configuration of the scan parameters such as delay before measurement readout at each step, step size, and measurement range for each axes. Since a high-resolution scan can take a long time, the software is configurable with separate measurement settings. This allows a quick search for the beam with fast stepping, and then to only measure the interesting part at high resolution. The selection of the region of interest is manual.

The plots at the bottom show the cuts for both axes for both recorded beams. They can either show the raw obtained power change during the cut, like in figure A.3, or the calculated beam profile, as shown in figure A.4. The beam profile is calculated by taking the derivative of the cut.




**Figure A.3:** Control software for the beam analyzer. Channel 1 is the QCL, channel 2 is the 1.5  $\mu\text{m}$  pump laser. Left plot: cut in direction A (horizontal), right plot: cut in direction B (vertical). On the top left, the extracted beam parameters for the individual cuts are shown. All values for positions and widths are in  $\mu\text{m}$ . The measurement was taken while the overlap of the two beams was prepared for sum-frequency generation. The beam analyzer was a few centimeters away from the focus point of the beams. After the beam overlap was established using the beam analyzer, sum-frequency generation was quickly obtained after the crystal was placed in the beams.










**Figure A.4:** Graphs in the control software showing the calculated beam profile from the raw data shown in figure A.3. Left plot: cut in direction A (horizontal), right plot: cut in direction B (vertical). Negative values on the amplitude scale are due to noise. The fiber laser on channel 2 shows a nice profile. The QCL on channel 1, on the other hand, shows a three-lobe structure, which was observed for this laser already on an indicator card. The plots indicate that the fiber laser is overlapped with the regions where the QCL beam has highest intensity.




# Acknowledgements






I thank Prof. Stephan Schiller  for giving me the opportunity to work in his institute, on a wide range of interesting topics, in an independent manner. I value his persistence and creativity in scientific discussions.

I thank Prof. Dr. Axel Görlitz  for taking the time to be the second reviewer of my thesis.

I am grateful to Vladimir Korobov  and Dimitar Bakalov  for their lectures about the theoretical aspects of our work. I thank Ken Brown  for helpful discussions, general geek fun and the lectures he gave while he was in Düsseldorf. The QCL spectroscopic source only became possible because Arnaud Grisard, Eric Lallier and Bruno Gérard provided us with the GaAs crystals used for connecting the QCL to the frequency comb. I would like to thank Bernhard Roth , Tobias Schneider and Sergey Vasilyev  for helpful discussions during the initial phase of the project. I also thank Patrick Dupré  for helpful discussions during his stay in Düsseldorf.

For help with the organization of my first lecture and generally helpful discussions, I would like to thank Prof. Schumacher and Götz Lehmann .

I would like to thank my former colleagues Qun-Feng Chen, Jianwei Shen, Ulf Bressel and Evangelos Magoulakis.

I thank Soroosh Alighanbari  for his persistence in working through the hard times when things did not work out as planned, until we finally reached the point where things started working as they should. I thank Ulrich Rosowski for many creative discussions and tossing around ideas, and good friendship. I thank them both and as well as my colleagues Christian Wellers , Eugen Wiens , Alexander Nevsky, Chang Jian Kwong , Beate Rödding, Gouri S. Giri , Magnus R. Schenkel, Ivan V. Kortunov, René Oswald, Rita Gusek, Arne Kallweit, Timon Kunz and Victor A. Vogt for making the institute a fun place to work in. I would like to thank Oliver Wyczisk and Peter Dutkiewicz for their consultations on mechanical and electronic problems.


A special thank you goes out to my wife and two daughters, for their patience while I was writing my thesis. I appreciate the early interest in science which my daughters are showing at their young age. I would also like to thank my parents for their continued support throughout my life, and for giving me the opportunity to learn a lot while I was young.


This research has made use of NASA's Astrophysics Data System. Data evaluation and visualization was done partially using Jupyter, which is based on IPython [146]. Useful and quick estimations of non-linear conversion efficiencies were performed using the SNLO nonlinear optics code available from A. V. Smith, AS-Photonics, Albuquerque, NM. This research made use of Astropy, a community-developed core Python package for Astronomy [147, 148].


## Publication list


1. S. Vasilyev, A. Nevsky, I. Ernsting, M. Hansen, J. Shen, and S. Schiller, “Compact all-solid-state continuous-wave single-frequency UV source with frequency stabilization for laser cooling of  $\text{Be}^+$  ions,” *Applied Physics B*, volume 103, number 1, pages 27–33, 2011, ISSN: 1432-0649. DOI: 10.1007/s00340-011-4435-1
2. U. Bressel, A. Borodin, J. Shen, M. Hansen, I. Ernsting, and S. Schiller, “Manipulation of Individual Hyperfine States in Cold Trapped Molecular Ions and Application to  $\text{HD}^+$  Frequency Metrology,” *Physical Review Letters*, volume 108, page 183 003, issue 18, 2012. DOI: 10.1103/PhysRevLett.108.183003. arXiv: 1203.2153 [physics.atom-ph]
3. J. Shen, A. Borodin, M. Hansen, and S. Schiller, “Observation of a rotational transition of trapped and sympathetically cooled molecular ions,” *Physical Review A*, volume 85, page 032 519, issue 3, 2012. DOI: 10.1103/PhysRevA.85.032519. arXiv: 1202.5672 [quant-ph]
4. M. G. Hansen, I. Ernsting, S. V. Vasilyev, A. Grisard, E. Lallier, B. Gérard, and S. Schiller, “Robust, frequency-stable and accurate mid-IR laser spectrometer based on frequency comb metrology of quantum cascade lasers up-converted in orientation-patterned GaAs,” *Optics Express*, volume 21, number 22, pages 27 043–27 056, 2013. DOI: 10.1364/OE.21.027043. arXiv: 1308.6430 [physics.optics]
5. M. G. Hansen, E. Magoulakis, Q.-F. Chen, I. Ernsting, and S. Schiller, “Quantum cascade laser-based mid-IR frequency metrology system with ultra-narrow linewidth and  $1 \times 10^{-13}$ -level frequency instability,” *Optics Letters*, volume 40, number 10, pages 2289–2292, 2015. DOI: 10.1364/OL.40.002289. arXiv: 1504.06216 [physics.optics]
6. S. Alighanbari, M. G. Hansen, V. I. Korobov, and S. Schiller, “Rotational spectroscopy of cold and trapped molecular ions in the Lamb-Dicke regime,” *Nature Physics*, volume 14, pages 555–559, 2018. DOI: 10.1038/s41567-018-0074-3. arXiv: 1802.03208 [quant-ph]
7. C. J. Kwong, M. G. Hansen, J. Sugawara, and S. Schiller, “Characterization of the long-term dimensional stability of a NEXCERA block using the optical resonator technique,” *Measurement Science and Technology*, volume 29, number 7, page 075 011, 2018. DOI: 10.1088/1361-6501/aac3b0. arXiv: 1805.08073 [physics.ins-det]
8. R. Oswald, M. G. Hansen, E. Wiens, A. Yu. Nevsky, and S. Schiller, “Characteristics of long-lived persistent spectral holes in  $\text{Eu}^{3+}:\text{Y}_2\text{SiO}_5$  at 1.2 K,” *Physical Review A*, volume 98, page 062 516, issue 6, 2018. DOI: 10.1103/PhysRevA.98.062516. arXiv: 1811.08346 [physics.atom-ph]
9. I. V. Kortunov, S. Alighanbari, M. G. Hansen, G. S. Giri, V. I. Korobov, and S. Schiller, “Proton–electron mass ratio by high-resolution optical spectroscopy of ion ensembles in the resolved-carrier regime,” *Nature Physics*, 2021. DOI: 10.1038/s41567-020-01150-7. arXiv: 2103.11741 [quant-ph]

## List of ORCIDs


Soroosh Alighanbari  <https://orcid.org/0000-0003-0111-9794>


Dimitar Bakalov  <https://orcid.org/0000-0001-9320-9185>


Ken Brown  <https://orcid.org/0000-0001-7716-1425>


Patrick Dupré  <https://orcid.org/0000-0003-4854-0623>


Gouri S. Giri  <https://orcid.org/0000-0002-6713-4412>


Prof. Dr. Axel Görlitz  <http://orcid.org/0000-0003-2892-3571>


Michael G. Hansen  <https://orcid.org/0000-0001-5180-2511>


Vladimir Korobov  <https://orcid.org/0000-0003-3724-0270>


Chang Jian Kwong  <https://orcid.org/0000-0001-5328-5853>


Götz Lehmann  <https://orcid.org/0000-0002-2502-6210>

Bernhard Roth  <http://orcid.org/0000-0001-9389-7125>

Prof. Stephan Schiller  <https://orcid.org/0000-0002-0797-8648>

Sergey Vasilyev  <https://orcid.org/0000-0002-2520-3547>

Christian Wellers  <https://orcid.org/0000-0001-6084-6495>

Eugen Wiens  <https://orcid.org/0000-0002-0013-1727>

## Bibliography

- [1] P. J. Mohr, D. B. Newell, and B. N. Taylor, “CODATA Recommended Values of the Fundamental Physical Constants: 2014,” *Journal of Physical and Chemical Reference Data*, volume 45, number 4, 043102, page 043 102, Dec. 2016. DOI: 10.1063/1.4954402 (cited on pages 6, 11, 46, 88).
- [2] P. J. Mohr, D. B. Newell, B. N. Taylor, and E. Tiesinga. (2019). “The 2018 CODATA Recommended Values of the Fundamental Physical Constants (Web version 8.0).” Database developed by J. Baker, M. Douma, and S. Kotochigova. National Institute of Standards and Technology, Gaithersburg, MD 20899. Accessed: 2021-03-09, [Online]. Available: <http://physics.nist.gov/constants> (cited on pages 7, 11, 48, 88).
- [3] V. I. Korobov, “Coulomb three-body bound-state problem: Variational calculations of nonrelativistic energies,” *Physical Review A*, volume 61, number 6, 064503, page 064 503, 2000. DOI: 10.1103/PhysRevA.61.064503 (cited on page 9).
- [4] V. I. Korobov, “Leading-order relativistic and radiative corrections to the rovibrational spectrum of  $\text{H}_2^+$  and  $\text{HD}^+$  molecular ions,” *Physical Review A*, volume 74, page 052 506, issue 5, 2006. DOI: 10.1103/PhysRevA.74.052506 (cited on pages 9, 10, 47).
- [5] —, “Relativistic corrections of  $m\alpha^6$  order to the rovibrational spectrum of  $\text{H}_2^+$  and  $\text{HD}^+$  molecular ions,” *Physical Review A*, volume 77, page 022 509, issue 2, 2008. DOI: 10.1103/PhysRevA.77.022509 (cited on page 10).
- [6] V. I. Korobov, L. Hilico, and J. P. Karr, “Theoretical transition frequencies beyond 0.1 ppb accuracy in  $\text{H}_2^+$ ,  $\text{HD}^+$ , and antiprotonic helium,” *Physical Review A*, volume 89, page 032 511, 2014. DOI: 10.1103/PhysRevA.89.032511 (cited on page 10).
- [7] E. H. Wichmann and N. M. Kroll, “Vacuum Polarization in a Strong Coulomb Field,” *Physical Review*, volume 101, number 2, pages 843–859, Jan. 1956. DOI: 10.1103/PhysRev.101.843 (cited on page 10).
- [8] V. I. Korobov, L. Hilico, and J. P. Karr, “Fundamental Transitions and Ionization Energies of the Hydrogen Molecular Ions with Few ppt Uncertainty,” *Physical Review Letters*, volume 118, number 23, 233001, page 233 001, Jun. 2017. DOI: 10.1103/PhysRevLett.118.233001. arXiv: 1703.07972 [physics.atom-ph] (cited on page 10).
- [9] V. I. Korobov, L. Hilico, and J.-P. Karr, “ $m\alpha^7$ -Order Corrections in the Hydrogen Molecular Ions and Antiprotonic Helium,” *Physical Review Letters*, volume 112, page 103 003, issue 10, 2014. DOI: 10.1103/PhysRevLett.112.103003 (cited on page 10).
- [10] S. Alighanbari, G. S. Giri, F. L. Constantin, V. I. Korobov, and S. Schiller, “Precise test of quantum electrodynamics and determination of fundamental constants with  $\text{HD}^+$  ions,” *Nature*, volume 581, number 7807, pages 152–158, May 2020. DOI: 10.1038/s41586-020-2261-5 (cited on pages 10, 13, 20, 49, 86–88).
- [11] S. Sturm, F. Köhler, J. Zatorski, A. Wagner, Z. Harman, G. Werth, W. Quint, C. H. Keitel, and K. Blaum, “High-precision measurement of the atomic mass of the electron,” *Nature*, volume 506, pages 467–470, 2014. DOI: 10.1038/nature13026 (cited on pages 10, 49, 88).
- [12] S. Patra, M. Germann, J.-P. Karr, M. Haidar, L. Hilico, V. I. Korobov, F. M. J. Cozijn, K. S. E. Eikema, W. Ubachs, and J. C. J. Koelemeij, “Proton-electron mass ratio from laser spectroscopy of  $\text{HD}^+$  at the part-per-trillion level,” *Science*, volume 369, number 6508, pages 1238–1241, 2020, ISSN: 0036-8075. DOI: 10.1126/science.aba0453 (cited on pages 10, 49, 87, 88).

- [13] E. R. Cohen and B. N. Taylor, “The 1973 Least-Squares Adjustment of the Fundamental Constants,” *Journal of Physical and Chemical Reference Data*, volume 2, number 4, pages 663–734, Oct. 1973. DOI: 10.1063/1.3253130 (cited on pages 11, 88).
- [14] E. R. Cohen and B. N. Taylor, “The 1986 CODATA Recommended Values of the Fundamental Physical Constants,” *Journal of Physical and Chemical Reference Data*, volume 17, number 4, pages 1795–1803, Oct. 1988. DOI: 10.1063/1.555817 (cited on pages 11, 88).
- [15] P. J. Mohr and B. N. Taylor, “CODATA Recommended Values of the Fundamental Physical Constants: 1998,” *Journal of Physical and Chemical Reference Data*, volume 28, number 6, pages 1713–1852, Nov. 1999. DOI: 10.1063/1.556049 (cited on pages 11, 88).
- [16] —, “CODATA recommended values of the fundamental physical constants: 2002,” *Reviews of Modern Physics*, volume 77, number 1, pages 1–107, Jan. 2005. DOI: 10.1103/RevModPhys.77.1 (cited on pages 11, 88).
- [17] P. J. Mohr, B. N. Taylor, and D. B. Newell, “CODATA recommended values of the fundamental physical constants: 2006,” *Journal of Physical and Chemical Reference Data*, volume 37, number 3, pages 1187–1284, Sep. 2008. DOI: 10.1063/1.2844785 (cited on page 11).
- [18] —, “CODATA Recommended Values of the Fundamental Physical Constants: 2010a,” *Journal of Physical and Chemical Reference Data*, volume 41, number 4, pages 043 109–043 109, Dec. 2012. DOI: 10.1063/1.4724320 (cited on pages 11, 88).
- [19] P. J. Mohr, D. B. Newell, B. N. Taylor, and E. Tiesinga, “Data and analysis for the CODATA 2017 special fundamental constants adjustment,” *Metrologia*, volume 55, number 1, pages 125–146, 2018. DOI: 10.1088/1681-7575/aa99bc (cited on page 11).
- [20] M. Hori, A. Sôtér, D. Barna, A. Dax, R. Hayano, S. Friedreich, B. Juhász, T. Pask, E. Widmann, D. Horváth, L. Venturelli, and N. Zurlo, “Two-photon laser spectroscopy of antiprotonic helium and the antiproton-to-electron mass ratio,” *Nature*, volume 475, pages 484–488, 2011. DOI: 10.1038/nature10260 (cited on pages 11, 13, 88).
- [21] D. L. Farnham, R. S. Van Dyck, and P. B. Schwinberg, “Determination of the Electron’s Atomic Mass and the Proton/Electron Mass Ratio via Penning Trap Mass Spectroscopy,” *Physical Review Letters*, volume 75, pages 3598–3601, issue 20, 1995. DOI: 10.1103/PhysRevLett.75.3598 (cited on pages 11, 88).
- [22] E. Reinhold, R. Buning, U. Hollenstein, A. Ivanchik, P. Petitjean, and W. Ubachs, “Indication of a Cosmological Variation of the Proton-Electron Mass Ratio Based on Laboratory Measurement and Reanalysis of H<sub>2</sub> Spectra,” *Physical Review Letters*, volume 96, number 15, 151101, page 151 101, Apr. 2006. DOI: 10.1103/PhysRevLett.96.151101 (cited on page 11).
- [23] Y. V. Stadnik and V. V. Flambaum, “Can Dark Matter Induce Cosmological Evolution of the Fundamental Constants of Nature?” *Physical Review Letters*, volume 115, number 20, 201301, page 201 301, Nov. 2015. DOI: 10.1103/PhysRevLett.115.201301. arXiv: 1503.08540 [astro-ph.CO] (cited on pages 11, 12).
- [24] H. Grote and Y. V. Stadnik, “Novel signatures of dark matter in laser-interferometric gravitational-wave detectors,” *Physical Review Research*, volume 1, number 3, 033187, page 033 187, Dec. 2019. DOI: 10.1103/PhysRevResearch.1.033187. arXiv: 1906.06193 [astro-ph.IM] (cited on pages 11, 12).

- [25] D. Bakalov, V. Korobov, and S. Schiller, “Magnetic field effects in the transitions of the  $\text{HD}^+$  molecular ion and precision spectroscopy,” *Journal of Physics B: Atomic, Molecular and Optical Physics*, volume 44, page 025 003, 2011, Corrigendum: *Journal of Physics B: Atomic, Molecular and Optical Physics*. **45**, 049501 (2012), doi:10.1088/0953-4075/45/4/049501. DOI: 10.1088/0953-4075/44/2/025003 (cited on pages 11, 17).
- [26] W. Ubachs, J. Bagdonaite, E. J. Salumbides, M. T. Murphy, and L. Kaper, “Colloquium: Search for a drifting proton-electron mass ratio from  $\text{H}_2$ ,” *Reviews of Modern Physics*, volume 88, number 2, 021003, page 021 003, Apr. 2016. DOI: 10.1103/RevModPhys.88.021003. arXiv: 1511.04476 [astro-ph.GA] (cited on page 12).
- [27] R. Quast, D. Reimers, and S. A. Levshakov, “Probing the variability of the fine-structure constant with the VLT/UVES,” *Astronomy and Astrophysics*, volume 415, pages L7–L11, Feb. 2004. DOI: 10.1051/0004-6361:20040013. arXiv: astro-ph/0311280 [astro-ph] (cited on page 12).
- [28] J. Bagdonaite, P. Jansen, C. Henkel, H. L. Bethlem, K. M. Menten, and W. Ubachs, “A Stringent Limit on a Drifting Proton-to-Electron Mass Ratio from Alcohol in the Early Universe,” *Science*, volume 339, number 6115, page 46, Jan. 2013. DOI: 10.1126/science.1224898 (cited on page 12).
- [29] A. Y. Potekhin, A. V. Ivanchik, D. A. Varshalovich, K. M. Lanzetta, J. A. Baldwin, G. M. Williger, and R. F. Carswell, “Testing Cosmological Variability of the Proton-to-Electron Mass Ratio Using the Spectrum of PKS 0528-250,” *The Astrophysical Journal*, volume 505, number 2, pages 523–528, Oct. 1998. DOI: 10.1086/306211. arXiv: astro-ph/9804116 [astro-ph] (cited on page 12).
- [30] V. V. Flambaum, D. B. Leinweber, A. W. Thomas, and R. D. Young, “Limits on variations of the quark masses, QCD scale, and fine structure constant,” *Physical Review D*, volume 69, number 11, 115006, page 115 006, Jun. 2004. DOI: 10.1103/PhysRevD.69.115006. arXiv: hep-ph/0402098 [hep-ph] (cited on page 12).
- [31] A. Ivanchik, P. Petitjean, D. Varshalovich, B. Aracil, R. Srianand, H. Chand, C. Ledoux, and P. Boissé, “A new constraint on the time dependence of the proton-to-electron mass ratio. Analysis of the Q 0347-383 and Q 0405-443 spectra,” *Astronomy and Astrophysics*, volume 440, number 1, pages 45–52, Sep. 2005. DOI: 10.1051/0004-6361:20052648. arXiv: astro-ph/0507174 [astro-ph] (cited on page 12).
- [32] X. Calmet and H. Fritzsch, “A time variation of proton-electron mass ratio and grand unification,” *EPL (Europhysics Letters)*, volume 76, number 6, pages 1064–1067, Dec. 2006. DOI: 10.1209/epl/i2006-10393-0. arXiv: astro-ph/0605232 [astro-ph] (cited on page 12).
- [33] V. V. Flambaum, “Variation of the Fundamental Constants: Theory and Observations,” in *The Proceedings of the Festschrift in Honor of Bruce H J Mckellar and Girish C Joshi*, Oct. 2007, pages 55–68. DOI: 10.1142/9789812770301\_0006 (cited on page 12).
- [34] V. V. Flambaum and M. G. Kozlov, “Limit on the Cosmological Variation of  $m_p/m_e$  from the Inversion Spectrum of Ammonia,” *Physical Review Letters*, volume 98, number 24, 240801, page 240 801, Jun. 2007. DOI: 10.1103/PhysRevLett.98.240801. arXiv: 0704.2301 [astro-ph] (cited on page 12).
- [35] M. T. Murphy, V. V. Flambaum, S. Muller, and C. Henkel, “Strong Limit on a Variable Proton-to-Electron Mass Ratio from Molecules in the Distant Universe,” *Science*, volume 320, number 5883, page 1611, Jun. 2008. DOI: 10.1126/science.1156352. arXiv: 0806.3081 [astro-ph] (cited on page 12).

- [36] C. Henkel, K. M. Menten, M. T. Murphy, N. Jethava, V. V. Flambaum, J. A. Braatz, S. Muller, J. Ott, and R. Q. Mao, “The density, the cosmic microwave background, and the proton-to-electron mass ratio in a cloud at redshift 0.9,” *Astronomy and Astrophysics*, volume 500, number 2, pages 725–734, Jun. 2009. DOI: 10.1051/0004-6361/200811475. arXiv: 0904.3081 [astro-ph.CO] (cited on page 12).
- [37] A. L. Malec, R. Buning, M. T. Murphy, N. Milutinovic, S. L. Ellison, J. X. Prochaska, L. Kaper, J. Tumlinson, R. F. Carswell, and W. Ubachs, “Keck telescope constraint on cosmological variation of the proton-to-electron mass ratio,” *Monthly Notices of the Royal Astronomical Society*, volume 403, number 3, pages 1541–1555, Apr. 2010. DOI: 10.1111/j.1365-2966.2009.16227.x. arXiv: 1001.4078 [astro-ph.CO] (cited on page 12).
- [38] N. Kanekar, “Constraining Changes in the Proton-Electron Mass Ratio with Inversion and Rotational Lines,” *The Astrophysical Journal*, volume 728, number 1, L12, page L12, Feb. 2011. DOI: 10.1088/2041-8205/728/1/L12. arXiv: 1101.4029 [astro-ph.CO] (cited on page 12).
- [39] S. Muller, A. Beelen, M. Guélin, S. Aalto, J. H. Black, F. Combes, S. J. Curran, P. Theule, and S. N. Longmore, “Molecules at  $z = 0.89$ . A 4-mm-rest-frame absorption-line survey toward PKS 1830-211,” *Astronomy and Astrophysics*, volume 535, A103, A103, Nov. 2011. DOI: 10.1051/0004-6361/201117096. arXiv: 1104.3361 [astro-ph.CO] (cited on page 12).
- [40] J. A. King, M. T. Murphy, W. Ubachs, and J. K. Webb, “New constraint on cosmological variation of the proton-to-electron mass ratio from Q0528-250,” *Monthly Notices of the Royal Astronomical Society*, volume 417, number 4, pages 3010–3024, Nov. 2011. DOI: 10.1111/j.1365-2966.2011.19460.x. arXiv: 1106.5786 [astro-ph.CO] (cited on page 12).
- [41] J. Bagdonaite, M. T. Murphy, L. Kaper, and W. Ubachs, “Constraint on a variation of the proton-to-electron mass ratio from  $H_2$  absorption towards quasar Q2348-011,” *Monthly Notices of the Royal Astronomical Society*, volume 421, number 1, pages 419–425, Mar. 2012. DOI: 10.1111/j.1365-2966.2011.20319.x. arXiv: 1112.0428 [astro-ph.CO] (cited on page 12).
- [42] H. Rahmani, R. Srianand, N. Gupta, P. Petitjean, P. Noterdaeme, and D. A. Vásquez, “Constraining the variation of fundamental constants at  $z \sim 1.3$  using 21-cm absorbers,” *Monthly Notices of the Royal Astronomical Society*, volume 425, number 1, pages 556–576, Sep. 2012. DOI: 10.1111/j.1365-2966.2012.21503.x. arXiv: 1206.2653 [astro-ph.CO] (cited on page 12).
- [43] J. Bagdonaite, M. Daprà, P. Jansen, H. L. Bethlem, W. Ubachs, S. Muller, C. Henkel, and K. M. Menten, “Robust Constraint on a Drifting Proton-to-Electron Mass Ratio at  $z=0.89$  from Methanol Observation at Three Radio Telescopes,” *Physical Review Letters*, volume 111, number 23, 231101, page 231 101, Dec. 2013. DOI: 10.1103/PhysRevLett.111.231101. arXiv: 1311.3438 [astro-ph.CO] (cited on page 12).
- [44] H. Rahmani, M. Wendt, R. Srianand, P. Noterdaeme, P. Petitjean, P. Molaro, J. B. Whitmore, M. T. Murphy, M. Centurion, H. Fathivavsari, S. D’Odorico, T. M. Evans, S. A. Levshakov, S. Lopez, C. J. A. P. Martins, D. Reimers, and G. Vladilo, “The UVES large program for testing fundamental physics - II. Constraints on a change in  $\mu$  towards quasar HE 0027-1836,” *Monthly Notices of the Royal Astronomical Society*, volume 435, number 1, pages 861–878, Oct. 2013. DOI: 10.1093/mnras/stt1356. arXiv: 1307.5864 [astro-ph.CO] (cited on page 12).
- [45] J. Bagdonaite, W. Ubachs, M. T. Murphy, and J. B. Whitmore, “Analysis of Molecular Hydrogen Absorption toward QSO B0642-5038 for a Varying Proton-to-electron Mass Ratio,” *The Astrophysical Journal*, volume 782, number 1, 10, page 10, Feb. 2014. DOI: 10.1088/0004-637X/782/1/10. arXiv: 1308.1330 [astro-ph.CO] (cited on page 12).

- [46] D. Albornoz Vásquez, H. Rahmani, P. Noterdaeme, P. Petitjean, R. Srianand, and C. Ledoux, “Molecular hydrogen in the  $z_{abs} = 2.66$  damped Lyman- $\alpha$  absorber towards Q J 0643-5041. Physical conditions and limits on the cosmological variation of the proton-to-electron mass ratio,” *Astronomy and Astrophysics*, volume 562, A88, A88, Feb. 2014. DOI: 10.1051/0004-6361/201322544. arXiv: 1310.8569 [astro-ph.CO] (cited on page 12).
- [47] J. Bagdonaite, W. Ubachs, M. T. Murphy, and J. B. Whitmore, “Constraint on a Varying Proton-Electron Mass Ratio 1.5 Billion Years after the Big Bang,” *Physical Review Letters*, volume 114, number 7, 071301, page 071 301, Feb. 2015. DOI: 10.1103/PhysRevLett.114.071301. arXiv: 1501.05533 [astro-ph.CO] (cited on page 12).
- [48] M. Daprà, J. Bagdonaite, M. T. Murphy, and W. Ubachs, “Constraint on a varying proton-to-electron mass ratio from molecular hydrogen absorption towards quasar SDSS J123714.60+064759.5,” *Monthly Notices of the Royal Astronomical Society*, volume 454, number 1, pages 489–506, Nov. 2015. DOI: 10 . 1093 / mnras / stv1998. arXiv: 1508 . 07419 [astro-ph.CO] (cited on page 12).
- [49] M. Daprà, M. L. Niu, E. J. Salumbides, M. T. Murphy, and W. Ubachs, “Constraint on a Cosmological Variation in the Proton-to-electron Mass Ratio from Electronic CO Absorption,” *The Astrophysical Journal*, volume 826, number 2, 192, page 192, Aug. 2016. DOI: 10.3847/0004-637X/826/2/192. arXiv: 1605.09742 [astro-ph.CO] (cited on page 12).
- [50] C. J. A. P. Martins and M. Vila Miñana, “Consistency of local and astrophysical tests of the stability of fundamental constants,” *Physics of the Dark Universe*, volume 25, 100301, page 100 301, Sep. 2019. DOI: 10 . 1016 / j . dark . 2019 . 100301. arXiv: 1904 . 07896 [astro-ph.CO] (cited on page 12).
- [51] N. Huntemann, B. Lipphardt, C. Tamm, V. Gerginov, S. Weyers, and E. Peik, “Improved Limit on a Temporal Variation of  $m_p/m_e$  from Comparisons of  $\text{Yb}^+$  and Cs Atomic Clocks,” *Physical Review Letters*, volume 113, number 21, 210802, page 210 802, Nov. 2014. DOI: 10.1103/PhysRevLett.113.210802. arXiv: 1407.4408 [physics.atom-ph] (cited on page 12).
- [52] R. M. Godun, P. B. R. Nisbet-Jones, J. M. Jones, S. A. King, L. A. M. Johnson, H. S. Margolis, K. Szymaniec, S. N. Lea, K. Bongs, and P. Gill, “Frequency Ratio of Two Optical Clock Transitions in  $\text{Yb}^+$  171 and Constraints on the Time Variation of Fundamental Constants,” *Physical Review Letters*, volume 113, number 21, 210801, page 210 801, Nov. 2014. DOI: 10.1103/PhysRevLett.113.210801. arXiv: 1407.0164 [physics.atom-ph] (cited on page 12).
- [53] O. Aharony, S. S. Gubser, J. Maldacena, H. Ooguri, and Y. Oz, “Large N field theories, string theory and gravity,” *Physics Reports*, volume 323, number 3, pages 183 –386, 2000, ISSN: 0370-1573. DOI: 10.1016/S0370-1573(99)00083-6 (cited on page 12).
- [54] N. Arkani-Hamed, S. Dimopoulos, and G. Dvali, “The hierarchy problem and new dimensions at a millimeter,” *Physics Letters B*, volume 429, number 3-4, pages 263–272, 1998. DOI: 10.1016/S0370-2693(98)00466-3. arXiv: hep-ph/9803315 [hep-ph] (cited on pages 12, 13).
- [55] I. Antoniadis, S. Baessler, M. Büchner, V. Fedorov, S. Hoedl, A. Lambrecht, V. Nesvizhevsky, G. Pignol, K. Protasov, S. Reynaud, and Y. Sobolev, “Short-range fundamental forces,” *Comptes Rendus Physique*, volume 12, number 8, pages 755 –778, 2011, Ultra cold neutron quantum states, ISSN: 1631-0705. DOI: 10.1016/j.crhy.2011.05.004 (cited on page 12).



- [56] E. J. Salumbides, J. C. J. Koelemeij, J. Komasa, K. Pachucki, K. S. E. Eikema, and W. Ubachs, “Bounds on fifth forces from precision measurements on molecules,” *Physical Review D*, volume 87, page 112 008, issue 11, 2013. DOI: 10.1103/PhysRevD.87.112008 (cited on pages 12, 13, 48).
- [57] S. G. Karshenboim, “Constraints on a long-range spin-independent interaction from precision atomic physics,” *Physical Review D*, volume 82, page 073 003, issue 7, 2010. DOI: 10.1103/PhysRevD.82.073003 (cited on page 13).
- [58] S. K. Lamoreaux, “The Casimir Force and Related Effects: The Status of the Finite Temperature Correction and Limits on New Long-Range Forces,” *Annual Review of Nuclear and Particle Science*, volume 62, number 1, pages 37–56, 2012. DOI: 10.1146/annurev-nucl-102711-095013 (cited on page 13).
- [59] E. Adelberger, J. Gundlach, B. Heckel, S. Hoedl, and S. Schlamminger, “Torsion balance experiments: A low-energy frontier of particle physics,” *Progress in Particle and Nuclear Physics*, volume 62, number 1, pages 102–134, 2009, ISSN: 0146-6410. DOI: 10.1016/j.pnpnp.2008.08.002 (cited on page 13).
- [60] E. J. Salumbides, W. Ubachs, and V. I. Korobov, “Bounds on fifth forces at the sub-Å length scale,” *Journal of Molecular Spectroscopy*, volume 300, pages 65–69, Jun. 2014. DOI: 10.1016/j.jms.2014.04.003. arXiv: 1308.1711 [hep-ph] (cited on page 13).
- [61] U. Bressel, A. Borodin, J. Shen, M. Hansen, I. Ernsting, and S. Schiller, “Manipulation of Individual Hyperfine States in Cold Trapped Molecular Ions and Application to HD<sup>+</sup> Frequency Metrology,” *Physical Review Letters*, volume 108, page 183 003, issue 18, 2012. DOI: 10.1103/PhysRevLett.108.183003. arXiv: 1203.2153 [physics.atom-ph] (cited on pages 13, 60, 87, 94).
- [62] J. C. J. Koelemeij, B. Roth, A. Wicht, I. Ernsting, and S. Schiller, “Vibrational Spectroscopy of HD<sup>+</sup> with 2-ppb Accuracy,” *Physical Review Letters*, volume 98, page 173 002, issue 17, 2007. DOI: 10.1103/PhysRevLett.98.173002 (cited on pages 13, 87).
- [63] E. J. Salumbides, A. N. Schellekens, B. Gato-Rivera, and W. Ubachs, “Constraints on extra dimensions from precision molecular spectroscopy,” *New Journal of Physics*, volume 17, number 033015, 2015. DOI: 10.1088/1367-2630/17/3/033015 (cited on page 13).
- [64] L. Randall and R. Sundrum, “An Alternative to Compactification,” *Physical Review Letters*, volume 83, number 23, pages 4690–4693, 1999. DOI: 10.1103/PhysRevLett.83.4690. arXiv: hep-th/9906064 [hep-th] (cited on page 13).
- [65] —, “Large Mass Hierarchy from a Small Extra Dimension,” *Physical Review Letters*, volume 83, number 17, pages 3370–3373, 1999. DOI: 10.1103/PhysRevLett.83.3370. arXiv: hep-ph/9905221 [hep-ph] (cited on page 13).
- [66] H. Schnitzler, “Development of an Experiment for Trapping, Cooling, and Spectroscopy of Molecular Hydrogen Ions,” Ph.D. dissertation, Universität Konstanz, 2001 (cited on page 14).
- [67] R. H. Dicke, “The Effect of Collisions upon the Doppler Width of Spectral Lines,” *Physical Review*, volume 89, number 2, pages 472–473, 1953. DOI: 10.1103/physrev.89.472 (cited on pages 14, 17).
- [68] S. R. Jefferts, C. Monroe, E. W. Bell, and D. J. Wineland, “Coaxial-resonator-driven rf (Paul) trap for strong confinement,” *Physical Review A*, volume 51, number 4, pages 3112–3116, Apr. 1995. DOI: 10.1103/PhysRevA.51.3112 (cited on page 14).

- [69] F. Diedrich, J. C. Bergquist, W. M. Itano, and D. J. Wineland, “Laser cooling to the zero-point energy of motion,” *Physical Review Letters*, volume 62, number 4, pages 403–406, Jan. 1989. DOI: 10.1103/PhysRevLett.62.403 (cited on pages 14, 40).
- [70] D. Wineland and H. Dehmelt, “Proposed  $10^{14} \delta\nu/\nu$  laser fluorescence spectroscopy on  $\text{Ti}^+$  mono-ion oscillator III (sideband cooling),” *Bulletin of the American Physical Society*, volume 20, number 637, 1975 (cited on pages 14, 40).
- [71] J. C. J. Koelemeij, B. Roth, and S. Schiller, “Blackbody thermometry with cold molecular ions and application to ion-based frequency standards,” *Physical Review A*, volume 76, page 023 413, issue 2, 2007. DOI: 10.1103/PhysRevA.76.023413 (cited on page 14).
- [72] T. Schneider, B. Roth, H. Duncker, I. Ernsting, and S. Schiller, “All-optical preparation of molecular ions in the rovibrational ground state,” *Nature Physics*, volume 6, number 4, pages 275–278, Apr. 2010. DOI: 10.1038/nphys1605 (cited on pages 14, 43, 46).
- [73] D. Bakalov, V. I. Korobov, and S. Schiller, “High-precision calculation of the hyperfine structure of the  $\text{HD}^+$  ion,” *Physical Review Letters*, volume 97, page 243 001, 2006. DOI: 10.1103/PhysRevLett.97.243001 (cited on pages 15–17, 47).
- [74] B. D. Esry and H. R. Sadeghpour, “Adiabatic formulation of heteronuclear hydrogen molecular ion,” *Physical Review A*, volume 60, number 5, pages 3604–3617, Nov. 1999. DOI: 10.1103/PhysRevA.60.3604 (cited on page 15).
- [75] R. E. Moss, “Calculations for vibration-rotation levels of  $\text{HD}^+$ , in particular for high  $N$ ,” *Molecular Physics*, volume 78, number 2, pages 371–405, Jan. 1993. DOI: 10.1080/00268979300100291 (cited on pages 15, 16, 44).
- [76] S. Schiller, B. Roth, F. Lewen, O. Ricken, and M. C. Wiedner, “Ultra-narrow-linewidth continuous-wave THz sources based on multiplier chains,” *Applied Physics B: Lasers and Optics*, volume 95, number 1, pages 55–61, Apr. 2009. DOI: 10.1007/s00340-008-3279-9 (cited on page 17).
- [77] S. Alighanbari, M. G. Hansen, V. I. Korobov, and S. Schiller, “Rotational spectroscopy of cold and trapped molecular ions in the Lamb-Dicke regime,” *Nature Physics*, volume 14, pages 555–559, 2018. DOI: 10.1038/s41567-018-0074-3. arXiv: 1802.03208 [quant-ph] (cited on pages 20, 29, 46, 68, 87, 88, 94).
- [78] S. Borri, G. Insero, G. Santambrogio, D. Mazzotti, F. Cappelli, I. Galli, G. Galzerano, M. Marangoni, P. Laporta, V. Di Sarno, L. Santamaria, P. Maddaloni, and P. De Natale, “High-precision molecular spectroscopy in the mid-infrared using quantum cascade lasers,” *Applied Physics B: Lasers and Optics*, volume 125, number 1, 18, page 18, Jan. 2019. DOI: 10.1007/s00340-018-7119-2 (cited on page 22).
- [79] M. G. Hansen, I. Ernsting, S. V. Vasilyev, A. Grisard, E. Lallier, B. Gérard, and S. Schiller, “Robust, frequency-stable and accurate mid-IR laser spectrometer based on frequency comb metrology of quantum cascade lasers up-converted in orientation-patterned GaAs,” *Optics Express*, volume 21, number 22, pages 27 043–27 056, 2013. DOI: 10.1364/OE.21.027043. arXiv: 1308.6430 [physics.optics] (cited on pages 22, 66, 94).
- [80] M. G. Hansen, E. Magoulakis, Q.-F. Chen, I. Ernsting, and S. Schiller, “Quantum cascade laser-based mid-IR frequency metrology system with ultra-narrow linewidth and  $1 \times 10^{-13}$ -level frequency instability,” *Optics Letters*, volume 40, number 10, pages 2289–2292, 2015. DOI: 10.1364/OL.40.002289. arXiv: 1504.06216 [physics.optics] (cited on pages 22, 67, 94).

- [81] A. Grisard, E. Lallier, and B. Gérard, “Quasi-phase-matched gallium arsenide for versatile mid-infrared frequency conversion,” *Optical Materials Express*, volume 2, number 8, pages 1020–1025, 2012. DOI: 10.1364/OME.2.001020 (cited on page 22).
- [82] A. Grisard, F. Guty, E. Lallier, B. Gérard, and J. Jimenez, “Fabrication and applications of orientation-patterned gallium arsenide for mid-infrared generation,” *physica status solidi (c)*, volume 9, number 7, pages 1651–1654, 2012, ISSN: 1610-1642. DOI: 10.1002/pssc.201200024 (cited on page 22).
- [83] U. Bressel, I. Ernsting, and S. Schiller, “5  $\mu\text{m}$  laser source for frequency metrology based on difference frequency generation,” *Optics Letters*, volume 37, number 5, pages 918–920, 2012. DOI: 10.1364/OL.37.000918 (cited on page 30).
- [84] Q.-F. Chen, A. Nevsky, M. Cardace, S. Schiller, T. Legero, S. Häfner, A. Uhde, and U. Sterr, “A compact, robust, and transportable ultra-stable laser with a fractional frequency instability of  $1 \times 10^{-15}$ ,” *Review of Scientific Instruments*, volume 85, 113107, page 113 107, 2014. DOI: 10.1063/1.4898334 (cited on page 35).
- [85] E. Wiens, A. Yu. Nevsky, and S. Schiller, “Resonator with Ultrahigh Length Stability as a Probe for Equivalence-Principle-Violating Physics,” *Physical Review Letters*, volume 117, number 27, 271102, page 271 102, Dec. 2016. DOI: 10.1103/PhysRevLett.117.271102. arXiv: 1612.01467 [gr-qc] (cited on page 35).
- [86] Corning, Inc. (2016). “ULE Manufacturer’s Specification.” Accessed: 2020-08-23, [Online]. Available: <https://www.corning.com/media/worldwide/csm/documents/7972%20ULE%20Product%20Information%20Jan%202016.pdf> (cited on page 35).
- [87] Schott AG. (2011). “Manufacturer’s Specification.” Accessed: 2020-08-23, [Online]. Available: [http://www.schott.com/d/advanced\\_optics/f7ae3c11-0226-4808-90c7-59d6c8816daf/1.0/schott\\_zerodur\\_katalog\\_july\\_2011\\_en.pdf](http://www.schott.com/d/advanced_optics/f7ae3c11-0226-4808-90c7-59d6c8816daf/1.0/schott_zerodur_katalog_july_2011_en.pdf) (cited on page 35).
- [88] Krosaki Harima Corporation. (2017). “NEXCERA specifications.” Accessed: 2020-08-23, [Online]. Available: <https://krosaki-fc.com/en/ceramics/nexcera.html> (cited on page 35).
- [89] A. Takahashi, “Long-term dimensional stability of a line scale made of low thermal expansion ceramic NEXCERA,” *Measurement Science and Technology*, volume 23, number 3, 035001, page 035 001, Mar. 2012. DOI: 10.1088/0957-0233/23/3/035001 (cited on pages 35, 36).
- [90] K. Hosaka, H. Inaba, D. Akamatsu, M. Yasuda, J. Sugawara, A. Onae, and F.-L. Hong, “A Fabry-Pérot Etalon with an Ultralow Expansion Ceramic Spacer,” *Japanese Journal of Applied Physics*, volume 52, number 3R, 032402, page 032 402, Mar. 2013. DOI: 10.7567/JJAP.52.032402 (cited on page 36).
- [91] I. Ito, A. Silva, T. Nakamura, and Y. Kobayashi, “Stable CW laser based on low thermal expansion ceramic cavity with 49 mHz/s frequency drift,” *Optics Express*, volume 25, number 21, page 26 020, Oct. 2017. DOI: 10.1364/OE.25.026020 (cited on page 36).
- [92] J. Alnis, A. Matveev, N. Kolachevsky, T. Udem, and T. W. Hänsch, “Subhertz linewidth diode lasers by stabilization to vibrationally and thermally compensated ultralow-expansion glass Fabry-Pérot cavities,” *Physical Review A*, volume 77, number 5, 053809, page 053 809, May 2008. DOI: 10.1103/PhysRevA.77.053809. arXiv: 0801.4199 [physics.optics] (cited on page 36).
- [93] J. Keller, S. Ignatovich, S. A. Webster, and T. E. Mehlstäubler, “Simple vibration-insensitive cavity for laser stabilization at the  $10^{-16}$  level,” *Applied Physics B: Lasers and Optics*, volume 116, number 1, pages 203–210, Jul. 2014. DOI: 10.1007/s00340-013-5676-y. arXiv: 1307.3917 [physics.optics] (cited on page 36).

- [94] S. Häfner, S. Falke, C. Grebing, S. Vogt, T. Legero, M. Merimaa, C. Lisdat, and U. Sterr, “ $8 \times 10^{-17}$  fractional laser frequency instability with a long room-temperature cavity,” *Optics Letters*, volume 40, number 9, page 2112, May 2015. DOI: 10.1364/OL.40.002112. arXiv: 1502.02608 [physics.optics] (cited on page 36).
- [95] J. Keupp, A. Douillet, T. E. Mehlstäubler, N. Rehbein, E. M. Rasel, and W. Ertmer, “A high-resolution Ramsey-Bordé spectrometer for optical clocks based on cold Mg atoms,” *European Physical Journal D*, volume 36, number 3, pages 289–294, Dec. 2005. DOI: 10.1140/epjd/e2005-00302-7 (cited on page 36).
- [96] C. J. Kwong, M. G. Hansen, J. Sugawara, and S. Schiller, “Characterization of the long-term dimensional stability of a NEXCERA block using the optical resonator technique,” *Measurement Science and Technology*, volume 29, number 7, page 075 011, 2018. DOI: 10.1088/1361-6501/aac3b0. arXiv: 1805.08073 [physics.ins-det] (cited on pages 36, 69, 94).
- [97] F. Könz, Y. Sun, C. W. Thiel, R. L. Cone, R. W. Equall, R. L. Hutcheson, and R. M. Macfarlane, “Temperature and concentration dependence of optical dephasing, spectral-hole lifetime, and anisotropic absorption in  $\text{Eu}^{3+}:\text{Y}_2\text{SiO}_5$ ,” *Physical Review B*, volume 68, number 8, 085109, page 085 109, Aug. 2003. DOI: 10.1103/PhysRevB.68.085109 (cited on page 37).
- [98] E. Wiens, C. J. Kwong, T. Müller, and S. Schiller, “A simplified cryogenic optical resonator apparatus providing ultra-low frequency drift,” *Review of Scientific Instruments*, volume 91, number 4, 045112, page 045 112, Apr. 2020. DOI: 10.1063/1.5140321. arXiv: 2004.01552 [physics.ins-det] (cited on page 37).
- [99] S. Vasilyev, A. Nevsky, I. Ernsting, M. Hansen, J. Shen, and S. Schiller, “Compact all-solid-state continuous-wave single-frequency UV source with frequency stabilization for laser cooling of  $\text{Be}^+$  ions,” *Applied Physics B*, volume 103, number 1, pages 27–33, 2011, ISSN: 1432-0649. DOI: 10.1007/s00340-011-4435-1 (cited on pages 37, 51, 94).
- [100] J. Scheuer, “Computergesteuerte Reinigung eines gespeicherten Beryllium-Ionenclusters,” Bachelor’s thesis, Heinrich-Heine-Universität Düsseldorf, 2017 (cited on pages 38, 68).
- [101] C. Wellers, “Entwicklung einer Einzelionenfallenapparatur,” M.S. thesis, Heinrich-Heine-Universität Düsseldorf, 2014 (cited on pages 39, 40).
- [102] A. Nevsky, S. Alighanbari, Q. F. Chen, I. Ernsting, S. Vasilyev, S. Schiller, G. Barwood, P. Gill, N. Poli, and G. M. Tino, “Robust frequency stabilization of multiple spectroscopy lasers with large and tunable offset frequencies,” *Optics Letters*, volume 38, number 22, page 4903, Nov. 2013. DOI: 10.1364/OL.38.004903. arXiv: 1309.3879 [physics.optics] (cited on pages 42, 44).
- [103] R. Drever, J. Hall, F. Kowalski, J. Hough, G. Ford, A. Munley, and H. Ward, “Laser phase and frequency stabilization using an optical resonator,” English, *Applied Physics B*, volume 31, number 2, pages 97–105, 1983, ISSN: 0946-2171. DOI: 10.1007/BF00702605 (cited on page 42).
- [104] S. Alighanbari, “Development of laser frequency stabilization systems for high-resolution spectroscopy,” M.S. thesis, Heinrich-Heine-Universität Düsseldorf, 2013 (cited on pages 43, 68).
- [105] B. Meyer, S. Saupe, M. H. Wappelhorst, T. George, F. Kühnemann, M. Schneider, M. Havenith, W. Urban, and J. Legrand, “CO-laser side-band spectrometer: Sub-Doppler heterodyne frequency measurements around  $5 \mu\text{m}$ ,” *Applied Physics B: Lasers and Optics*, volume 61, number 2, pages 169–173, Aug. 1995. DOI: 10.1007/BF01090939 (cited on page 44).
- [106] G & A Technical Software, Inc. (2011). “Spectral Calculator.” Accessed: 2011-05-31, [Online]. Available: <http://www.spectralcalc.com> (cited on page 44).

- [107] J. Shen, A. Borodin, M. Hansen, and S. Schiller, “Observation of a rotational transition of trapped and sympathetically cooled molecular ions,” *Physical Review A*, volume 85, page 032 519, issue 3, 2012. DOI: 10 . 1103 / PhysRevA . 85 . 032519. arXiv: 1202 . 5672 [quant-ph] (cited on pages 46, 52, 94).
- [108] J. Shen, A. Borodin, and S. Schiller, “A simple method for characterization of the magnetic field in an ion trap using  $\text{Be}^+$  ions,” *The European Physical Journal D*, volume 68, number 12, 2014. DOI: 10.1140/epjd/e2014-50360-7 (cited on page 46).
- [109] I. V. Kortunov, S. Alighanbari, M. G. Hansen, G. S. Giri, V. I. Korobov, and S. Schiller, “Proton–electron mass ratio by high-resolution optical spectroscopy of ion ensembles in the resolved-carrier regime,” *Nature Physics*, 2021. DOI: 10.1038/s41567-020-01150-7. arXiv: 2103.11741 [quant-ph] (cited on pages 48, 49, 85, 87, 88, 94).
- [110] D. J. Fink and E. G. Myers, “Deuteron-to-Proton Mass Ratio from the Cyclotron Frequency Ratio of  $\text{H}_2^+$  to  $\text{D}^+$  with  $\text{H}_2^+$  in a Resolved Vibrational State,” *Physical Review Letters*, volume 124, number 1, 013001, page 013 001, 2020. DOI: 10.1103/PhysRevLett.124.013001 (cited on pages 48, 49).
- [111] F. Köhler, S. Sturm, A. Kracke, G. Werth, W. Quint, and K. Blaum, “The electron mass from g-factor measurements on hydrogen-like carbon  $^{12}\text{C}^{5+}$ ,” *Journal of Physics B Atomic Molecular Physics*, volume 48, number 14, 144032, page 144 032, Jul. 2015. DOI: 10.1088/0953-4075/48/14/144032. arXiv: 1604.04380 [physics.atom-ph] (cited on page 49).
- [112] F. Heiße, S. Rau, F. Köhler-Langes, W. Quint, G. Werth, S. Sturm, and K. Blaum, “High-precision mass spectrometer for light ions,” *Physical Review A*, volume 100, number 2, 022518, page 022 518, Aug. 2019. DOI: 10.1103/PhysRevA.100.022518. arXiv: 2002.11389 [physics.atom-ph] (cited on pages 49, 88).
- [113] S. Rau, F. Heiße, F. Köhler-Langes, S. Sasidharan, R. Haas, D. Renisch, C. E. Düllmann, W. Quint, S. Sturm, and K. Blaum, “Penning trap mass measurements of the deuteron and the  $\text{HD}^+$  molecular ion,” *Nature*, volume 585, number 7823, pages 43–47, Sep. 2020. DOI: 10.1038/s41586-020-2628-7 (cited on page 49).
- [114] R. Oswald, M. G. Hansen, E. Wiens, A. Yu. Nevsky, and S. Schiller, “Characteristics of long-lived persistent spectral holes in  $\text{Eu}^{3+}:\text{Y}_2\text{SiO}_5$  at 1.2 K,” *Physical Review A*, volume 98, page 062 516, issue 6, 2018. DOI: 10 . 1103 / PhysRevA . 98 . 062516. arXiv: 1811 . 08346 [physics.atom-ph] (cited on pages 76, 94).
- [115] K. A. Fedorova, A. D. McRobbie, G. S. Sokolovskii, P. G. Schunemann, and E. U. Rafailov, “Second harmonic generation in a low-loss orientation-patterned GaAs waveguide,” *Optics Express*, volume 21, number 14, page 16 424, Jul. 2013. DOI: 10.1364/OE.21.016424 (cited on page 86).
- [116] S. Roux, L. Cerutti, E. Tournie, B. Gérard, G. Patriarche, A. Grisard, and E. Lallier, “Low-loss orientation-patterned GaSb waveguides for mid-infrared parametric conversion,” *Optical Materials Express*, volume 7, number 8, page 3011, Aug. 2017. DOI: 10.1364/OME.7.003011 (cited on page 86).
- [117] F. L. Constantin, “A dual-frequency two-photon molecular clock with cold trapped  $\text{HD}^+$  ions,” in *Proc. SPIE*, series Society of Photo-Optical Instrumentation Engineers (SPIE) Conference Series, volume 10674, 2018, page 1 067 403. DOI: 10.1117/12.2306944 (cited on page 86).
- [118] J. P. Karr, “ $\text{H}_2^+$  and  $\text{HD}$ : Candidates for a molecular clock,” *Journal of Molecular Spectroscopy*, volume 300, pages 37–43, 2014. DOI: 10.1016/j.jms.2014.03.016. arXiv: 1403.6925 [physics.atom-ph] (cited on page 86).

- [119] T. Puppe, A. Sell, R. Kliese, N. Hoghooghi, A. Zach, and W. Kaenders, “Characterization of a DFG comb showing quadratic scaling of the phase noise with frequency,” *Optics Letters*, volume 41, number 8, page 1877, Apr. 2016. DOI: 10.1364/OL.41.001877 (cited on page 86).
- [120] E. Benkler, B. Lipphardt, T. Puppe, R. Wilk, F. Rohde, and U. Sterr, “End-to-end topology for fiber comb based optical frequency transfer at the  $10^{-21}$  level,” *Optics Express*, volume 27, number 25, page 36 886, Dec. 2019. DOI: 10.1364/OE.27.036886. arXiv: 1910.04261 [physics . optics ] (cited on page 86).
- [121] M. Giunta, W. Hänsel, M. Fischer, M. Lezius, T. Udem, and R. Holzwarth, “Real-time phase tracking for wide-band optical frequency measurements at the 20th decimal place,” *Nature Photonics*, volume 14, number 1, pages 44–49, Sep. 2019. DOI: 10.1038/s41566-019-0520-5 (cited on page 86).
- [122] S. Origlia, M. S. Pramod, S. Schiller, Y. Singh, K. Bongs, R. Schwarz, A. Al-Masoudi, S. Dörscher, S. Herbers, S. Häfner, U. Sterr, and C. Lisdat, “Towards an optical clock for space: Compact, high-performance optical lattice clock based on bosonic atoms,” *Physical Review A*, volume 98, number 5, 053443, page 053 443, Nov. 2018. DOI: 10.1103/PhysRevA.98.053443 (cited on page 86).
- [123] J. Gray and D. Allan, “A Method for Estimating the Frequency Stability of an Individual Oscillator,” in *28th Annual Symposium on Frequency Control*, 1974, pages 243–246. DOI: 10.1109/FREQ.1974.200027 (cited on page 86).
- [124] K. B. Jefferts, “Hyperfine Structure in the Molecular Ion  $\text{H}^+_2$ ,” *Physical Review Letters*, volume 23, number 26, pages 1476–1478, Dec. 1969. DOI: 10.1103/PhysRevLett.23.1476 (cited on page 87).
- [125] W. H. Wing, G. A. Ruff, J. Lamb Willis E., and J. J. Spezeski, “Observation of the infrared spectrum of the hydrogen molecular ion  $\text{HD}^+$ ,” *Physical Review Letters*, volume 36, number 25, pages 1488–1491, Jun. 1976. DOI: 10.1103/PhysRevLett.36.1488 (cited on page 87).
- [126] J. J. Spezeski, “Observation of the infrared spectrum of the hydrogen molecular ion,” Ph.D. dissertation, Yale Univ., New Haven, CT., Jan. 1977. DOI: 10079 / bibid / 9851153 (cited on page 87).
- [127] A. Balakrishnan, V. Smith, and B. P. Stoicheff, “Dissociation energy of the hydrogen molecule,” *Physical Review Letters*, volume 68, number 14, pages 2149–2152, Apr. 1992. DOI: 10.1103/PhysRevLett.68.2149 (cited on page 87).
- [128] A. Carrington, C. A. Leach, A. J. Marr, R. E. Moss, C. H. Pyne, and T. C. Steimle, “Microwave spectra of the  $\text{D}_2^+$  and  $\text{HD}^+$  ions near their dissociation limits,” *Journal of Chemical Physics*, volume 98, number 7, pages 5290–5301, Apr. 1993. DOI: 10.1063/1.464928 (cited on page 87).
- [129] Y. P. Zhang, C. H. Cheng, J. T. Kim, J. Stanojevic, and E. E. Eyler, “Dissociation Energies of Molecular Hydrogen and the Hydrogen Molecular Ion,” *Physical Review Letters*, volume 92, number 20, 203003, page 203 003, May 2004. DOI: 10.1103/PhysRevLett.92.203003 (cited on page 87).
- [130] J. Biesheuvel, J.-P. Karr, L. Hilico, K. S. E. Eikema, W. Ubachs, and J. C. J. Koelemeij, “Probing QED and fundamental constants through laser spectroscopy of vibrational transitions in  $\text{HD}^+$ ,” *Nature Communications*, volume 7, page 10 385, 2016. DOI: 10.1038/ncomms10385 (cited on pages 87, 88).
- [131] Z.-X. Zhong, X. Tong, Z.-C. Yan, and T.-Y. Shi, “High-precision spectroscopy of hydrogen molecular ions,” *Chinese Physics B*, volume 24, number 5, 053102, page 053 102, May 2015. DOI: 10.1088/1674-1056/24/5/053102 (cited on page 87).

- [132] B. Roth and S. Schiller, “Sympathetically Cooled Molecular Ions: From Principles to First Applications,” in *Cold Molecules*, R. Krems, B. Friedrich, and W. C. Stwalley, Eds., Boca Raton: CRC Press, 2009, ch. 18. DOI: 10.1201/9781420059045. arXiv: 0812.1154 (cited on page 87).
- [133] B. N. Taylor, W. H. Parker, and D. N. Langenberg, “Determination of  $e/h$ , Using Macroscopic Quantum Phase Coherence in Superconductors: Implications for Quantum Electrodynamics and the Fundamental Physical Constants,” *Reviews of Modern Physics*, volume 41, number 3, pages 375–496, Jul. 1969. DOI: 10.1103/RevModPhys.41.375 (cited on page 88).
- [134] G. Gärtner and E. Klempt, “A direct determination of the proton-electron mass ratio,” *Zeitschrift für Physik A - Atoms and Nuclei*, volume 287, number 1, pages 1–6, Mar. 1978. DOI: 10.1007/BF01408352 (cited on page 88).
- [135] G. Gräff, H. Kalinowsky, and J. Traut, “A direct determination of the proton electron mass ratio,” *Zeitschrift für Physik A - Atoms and Nuclei*, volume 297, number 1, pages 35–39, Mar. 1980. DOI: 10.1007/BF01414243 (cited on page 88).
- [136] J. van Dyck R. S. and P. B. Schwinberg, “Preliminary Proton/Electron Mass Ratio using a Compensated Quadrupole Penning Trap,” *Physical Review Letters*, volume 47, number 6, pages 395–398, Aug. 1981. DOI: 10.1103/PhysRevLett.47.395 (cited on page 88).
- [137] D. J. Wineland, J. J. Bollinger, and W. M. Itano, “Laser-Fluorescence Mass Spectroscopy,” *Physical Review Letters*, volume 50, number 9, pages 628–631, Feb. 1983. DOI: 10.1103/PhysRevLett.50.628 (cited on page 88).
- [138] J. Van Dyck R. S., F. L. Moore, D. L. Farnham, and P. B. Schwinberg, “New measurement of the proton-electron mass ratio,” *International Journal of Mass Spectrometry and Ion Processes*, volume 66, number 3, pages 327–337, Jun. 1985. DOI: 10.1016/0168-1176(85)80006-9 (cited on page 88).
- [139] G. Gabrielse, X. Fei, L. A. Orozco, R. L. Tjoelker, J. Haas, H. Kalinowsky, T. A. Trainor, and W. Kells, “Thousandfold improvement in the measured antiproton mass,” *Physical Review Letters*, volume 65, number 11, pages 1317–1320, Sep. 1990. DOI: 10.1103/PhysRevLett.65.1317 (cited on page 88).
- [140] G. Audi and A. H. Wapstra, “The 1993 atomic mass evaluation (I) Atomic mass table,” *Nuclear Physics A*, volume 565, number 1, pages 1–65, Dec. 1993. DOI: 10.1016/0375-9474(93)90024-R (cited on page 88).
- [141] T. Beier, H. Häffner, N. Hermanspahn, S. G. Karshenboim, H.-J. Kluge, W. Quint, S. Stahl, J. Verdú, and G. Werth, “New Determination of the Electron’s Mass,” *Physical Review Letters*, volume 88, page 011 603, issue 1, 2001. DOI: 10.1103/PhysRevLett.88.011603 (cited on page 88).
- [142] J. Verdú, S. Djekić, S. Stahl, T. Valenzuela, M. Vogel, G. Werth, T. Beier, H.-J. Kluge, and W. Quint, “Electronic  $g$  Factor of Hydrogenlike Oxygen  $^{16}\text{O}^{7+}$ ,” *Physical Review Letters*, volume 92, page 093 002, issue 9, 2004. DOI: 10.1103/PhysRevLett.92.093002 (cited on page 88).
- [143] M. Hori, A. Dax, J. Eades, K. Gomikawa, R. S. Hayano, N. Ono, W. Pirkel, E. Widmann, H. A. Torii, B. Juhász, D. Barna, and D. Horváth, “Determination of the Antiproton-to-Electron Mass Ratio by Precision Laser Spectroscopy of  $\bar{p}\text{He}^+$ ,” *Physical Review Letters*, volume 96, number 24, 243401, page 243 401, Jun. 2006. DOI: 10.1103/PhysRevLett.96.243401 (cited on page 88).
- [144] P. J. Mohr, B. N. Taylor, and D. B. Newell, “CODATA recommended values of the fundamental physical constants: 2006,” *Reviews of Modern Physics*, volume 80, pages 633–730, issue 2, 2008. DOI: 10.1103/RevModPhys.80.633 (cited on page 88).

- [145] U. Bressel, “High-resolution vibrational spectroscopy of cold molecular hydrogen ions,” Ph.D. dissertation, Heinrich-Heine-Universität Düsseldorf, 2011 (cited on page 88).
- [146] F. Pérez and B. E. Granger, “IPython: A System for Interactive Scientific Computing,” *Computing in Science and Engineering*, volume 9, number 3, pages 21–29, May 2007, ISSN: 1521-9615. DOI: 10.1109/MCSE.2007.53. [Online]. Available: <https://ipython.org> (cited on page 93).
- [147] Astropy Collaboration, T. P. Robitaille, E. J. Tollerud, P. Greenfield, M. Droettboom, E. Bray, T. Aldcroft, M. Davis, A. Ginsburg, A. M. Price-Whelan, W. E. Kerzendorf, A. Conley, N. Crighton, K. Barbary, D. Muna, H. Ferguson, F. Grollier, M. M. Parikh, P. H. Nair, H. M. Unther, C. Deil, J. Woillez, S. Conseil, R. Kramer, J. E. H. Turner, L. Singer, R. Fox, B. A. Weaver, V. Zabalza, Z. I. Edwards, K. Azalee Bostroem, D. J. Burke, A. R. Casey, S. M. Crawford, N. Dencheva, J. Ely, T. Jenness, K. Labrie, P. L. Lim, F. Pierfederici, A. Pontzen, A. Ptak, B. Refsdal, M. Servillat, and O. Streicher, “Astropy: A community Python package for astronomy,” *Astronomy and Astrophysics*, volume 558, A33, A33, Oct. 2013. DOI: 10.1051/0004-6361/201322068. arXiv: 1307.6212 [astro-ph.IM] (cited on page 93).
- [148] Astropy Collaboration, A. M. Price-Whelan, B. M. Sipőcz, H. M. Günther, P. L. Lim, S. M. Crawford, S. Conseil, D. L. Shupe, M. W. Craig, N. Dencheva, A. Ginsburg, J. T. VanderPlas, L. D. Bradley, D. Pérez-Suárez, M. de Val-Borro, T. L. Aldcroft, K. L. Cruz, T. P. Robitaille, E. J. Tollerud, C. Ardelean, T. Babej, Y. P. Bach, M. Bachetti, A. V. Bakanov, S. P. Bamford, G. Barentsen, P. Barmby, A. Baumbach, K. L. Berry, F. Biscani, M. Boquien, K. A. Bostroem, L. G. Bouma, G. B. Brammer, E. M. Bray, H. Breytenbach, H. Buddelmeijer, D. J. Burke, G. Calderone, J. L. Cano Rodríguez, M. Cara, J. V. M. Cardoso, S. Cheedella, Y. Copin, L. Corrales, D. Crichton, D. D’Avella, C. Deil, É. Depagne, J. P. Dietrich, A. Donath, M. Droettboom, N. Earl, T. Erben, S. Fabbro, L. A. Ferreira, T. Finethy, R. T. Fox, L. H. Garrison, S. L. J. Gibbons, D. A. Goldstein, R. Gommers, J. P. Greco, P. Greenfield, A. M. Groener, F. Grollier, A. Hagen, P. Hirst, D. Homeier, A. J. Horton, G. Hosseinzadeh, L. Hu, J. S. Hunkeler, Ž. Ivezić, A. Jain, T. Jenness, G. Kanarek, S. Kendrew, N. S. Kern, W. E. Kerzendorf, A. Khvalko, J. King, D. Kirkby, A. M. Kulkarni, A. Kumar, A. Lee, D. Lenz, S. P. Littlefair, Z. Ma, D. M. Macleod, M. Mastropietro, C. McCully, S. Montagnac, B. M. Morris, M. Mueller, S. J. Mumford, D. Muna, N. A. Murphy, S. Nelson, G. H. Nguyen, J. P. Ninan, M. Nöthe, S. Ogaz, S. Oh, J. K. Parejko, N. Parley, S. Pascual, R. Patil, A. A. Patil, A. L. Plunkett, J. X. Prochaska, T. Rastogi, V. Reddy Janga, J. Sabater, P. Sakurikar, M. Seifert, L. E. Sherbert, H. Sherwood-Taylor, A. Y. Shih, J. Sick, M. T. Silbiger, S. Singanamalla, L. P. Singer, P. H. Sladen, K. A. Sooley, S. Sornarajah, O. Streicher, P. Teuben, S. W. Thomas, G. R. Tremblay, J. E. H. Turner, V. Terrón, M. H. van Kerkwijk, A. de la Vega, L. L. Watkins, B. A. Weaver, J. B. Whitmore, J. Woillez, V. Zabalza, and Astropy Contributors, “The Astropy Project: Building an Open-science Project and Status of the v2.0 Core Package,” *The Astronomical Journal*, volume 156, number 3, 123, page 123, Sep. 2018. DOI: 10.3847/1538-3881/aabc4f. arXiv: 1801.02634 [astro-ph.IM] (cited on page 93).